

STRUCTURED OPTICAL MATERIALS FABRICATED USING TWO-PHOTON
POLYMERIZATION

by

Yanzeng Li

A dissertation submitted to the faculty of
The University of North Carolina at Charlotte
in partial fulfillment of the requirements
for the degree of Doctor of Philosophy in
Physics and optical science

Charlotte

2020

Approved by:

Dr. Tino Hofmann

Dr. Glenn Boreman

Dr. Thomas Suleski

Dr. Zia Salami

ABSTRACT

YANZENG LI. Structured Optical Materials Fabricated Using Two-Photon Polymerization. (Under the direction of DR. TINO HOFMANN)

Artificially structured materials, which are treated as macroscopically homogeneous media, exhibit *effective* optical properties that can be altered by engineering the materials' intrinsic geometries at a scale much smaller than the probing electromagnetic radiation at the wavelength of interest. Synthesizing structured optical materials to gain a variety of desired optical responses have flourished during the last decade thanks to the emergence of novel fabrication techniques like two-photon polymerization, for instance. Despite these advancements, there are still knowledge gaps regarding the optical properties of the polymers compatible with two-photon polymerization techniques. Representative examples demonstrating the potential of two-photon polymerization for the fabrication of all-dielectric optical metamaterials have not been extensively explored yet.

This dissertation focuses on the development of all-dielectric metamaterials with structural features at sub-wavelength scales by using two-photon polymerization in order to engineer the material's dielectric properties at optical frequencies. In order to understand the optical responses of the all-dielectric metamaterials developed here, we accurately determined the optical properties of several two-photon polymerized polymers using spectroscopic ellipsometry over a spectral range from the ultraviolet to the near-infrared for the first time. Two different structured material classes composed of the investigated polymers were fabricated. These materials were designed to suppress Fresnel reflection loss or achieve very high reflection, respectively, at telecommunication wavelengths.

The two-photon polymerization technique was further used to integrate engineered optical structures into the fabrication of opto-mechanical components. We established

a protocol for the rapid prototyping of functional opto-mechanical components. As an example, microlenses with anti-reflective structures conformally coated on concave lens interfaces and opto-mechanical components with critical features from the nm- to the mm-range have been fabricated in order to demonstrate our approach.

DEDICATION

This dissertation is dedicated to my beloved father who was always my power and inspiration source. He was a very energetic man who could always uplift me whenever I was trapped in a predicament. Although he will not be able to celebrate the completion of my dissertation with me in the physical world, I have perceived his happiness and pride for my achievement in another form of life. This dissertation is for him.

ACKNOWLEDGEMENTS

My sincere gratitude goes out to all the people listed below who had made my Ph.D. journey enjoyable and treasurable. Without the contributions from them, I would have not been able to complete this dissertation.

I would like to present my appreciation to my advisor, Prof. Tino Hofmann, for his professional and kind guidance that directed me from a nebulous situation to goal-oriented research world. He granted me freedom to pursue different research topics and also encouraged me to conduct multiple research projects in order to broaden my research experience. In addition, his insightful advice helped me to grasp the physical essence of the scientific problems I was working on. He was always willing to spend his time with me to revise my manuscripts word by word. I truly appreciate that he organized our research group into a constructive family where all members are supportive to and motivated by each other. Being a Ph.D. student studying in his research group during the last four years has given me many unforgotten moments.

I would like to thank Prof. Glenn Boreman for his consistent support my research work. He always devoted his time to revising my papers, and his suggestions always solidified the research discoveries and strengthened the scientific points. I would like to thank Prof. Thomas Suleski, who was not only my instructor in the course of optical modeling but also my dissertation committee member. He provided me with valuable advice, particularly on diffractive optics and freeform lens design. I would like to thank Prof. Zia Salami for serving as my graduate faulty representative and for being a part of dissertation committee. I would like to thank Prof. Menelaos Poutous for his constructive feedback on my papers. I would like to thank Prof. Ishwar Aggarwal for his willingness to share his positive passion with me all the time. I also would like to thank Prof. Michael Fiddy. He introduced me to the field of metamaterials and our discussions ignited my research interest.

I would like to thank Dr. Darrell Childers and his colleagues Trung Nguyen and

John Piland from U.S. Conec Ltd. Dr. Childers supported our research projects in the Center for Metamaterials (CfM) and shared his valuable suggestions, steering my research toward practical applications. I would like to thank Dr. Stefan Schöche from J.A. Woollam Co. Inc. He allowed us to use the sophisticated equipment of the J.A. Woollam Co. Inc. and helped us with measurements on numerous polymer samples. I also would like to thank all the colleagues and members from the CfM who kindly provided their valuable suggestions and help.

During the study in Prof. Hofmann's research group, I received invaluable assistance from my colleagues and had a great experience working with them. They deserve sincere gratitude from me. Micheal Mclamb is a responsible researcher and a hard worker. He was always there whenever I needed him. Serang Park is a optimistic person and the energy source for our group. Marc Lata is a smart researcher who assisted me with many tasks regarding optical components assembly.

For a Ph.D. student, the life is filled with exciting moments, for instance, when a papers is accepted for publication, but the rest of it is tough. Fortunately, I had the support by my friends Prof. Hanyang Li (Harbin Engineering University), Boya Jin (a Ph.D. student studying in Prof. Vasily Astratov's research group at UNC at Charlotte), Dr. Karteek Kunala (graduated from Prof. Menelaos Poutous's research group at UNC at Charlotte), Steve Glass (graduated from Prof. Thomas Suleski's research group at UNC at Charlotte), and Diana Joy (studied in Prof. Yuri Nesmelov's research group at UNC at Charlotte). They turned my Ph.D. life into a colorful and vivid journey. Without their support and care, I would have not been able to climb over this Ph.D. mountain. I owe my gratitude forever to my friends.

Finally, I would like to give my deepest gratitude to my family for their unequivocal support for these years. My wife took care our family such that I would not be distracted and was able to focus on my research work. My three kids as well as the upcoming one were behaving wonderful all the time, so that I was able to fully

concentrate on my work. For my parents, I could not find an appropriate phrase to express my heartfelt appreciation to them. They have sacrificed too much to protect my dream, and their selfless love has put me where I am today.

TABLE OF CONTENTS

LIST OF TABLES	xii
LIST OF FIGURES	xiii
LIST OF OWN PUBLICATIONS	xxi
CHAPTER 1: INTRODUCTION	1
1.1. Overview	1
1.2. Two-photon polymerization lithography	7
1.3. Spectroscopic ellipsometry	12
1.3.1. Jones matrix based ellipsometry for isotropic materials	13
1.3.2. Mueller matrix based ellipsometry for isotropic materials	15
1.3.3. Interpretation of Ψ and Δ	17
1.3.4. Data analysis	19
1.4. Effective medium theory	25
REFERENCES	30
CHAPTER 2: UV TO NIR OPTICAL PROPERTIES OF IP-DIP, IP-L, AND IP-S AFTER TWO-PHOTON POLYMERIZATION DETERMINED BY SPECTROSCOPIC ELLIPSOMETRY	34
2.1. Abstract	34
2.2. Introduction	34
2.3. Experiment	36
2.3.1. Sample preparation	36
2.3.2. Data acquisition and analysis	37
2.4. Results and discussion	41

	x
2.5. Conclusion	46
REFERENCES	49
CHAPTER 3: BROADBAND NEAR-INFRARED ANTIREFLECTION COATINGS FABRICATED BY THREE DIMENSIONAL DIRECT LASER WRITING	54
3.1. Abstract	54
3.2. Introduction	55
3.3. Theory and experiment	57
3.4. Conclusion	62
REFERENCES	64
CHAPTER 4: NEAR INFRARED TRANSMITTANCE ENHANCE- MENT USING FULLY CONFORMAL ANTI-REFLECTIVE STRUCTURED SURFACES ON MICROLENSES FABRICATED BY DIRECT LASER WRITING	67
4.1. Abstract	67
4.2. Introduction	68
4.3. Materials and methods	69
4.4. Results and discussion	70
4.5. Conclusion	74
REFERENCES	76
CHAPTER 5: FABRICATION OF OPTICAL COMPONENTS WITH NM- TO MM-SCALE CRITICAL FEATURES USING THREE- DIMENSIONAL DIRECT LASER WRITING	81
5.1. Abstract	81
5.2. Introduction	81

	xi
5.3. Experiment	83
5.3.1. Sample design	83
5.3.2. Sample fabrication	86
5.4. Results and discussion	88
5.5. Conclusion	90
REFERENCES	92
CHAPTER 6: HIGH-CONTRAST INFRARED POLYMER PHOTONIC CRYSTALS FABRICATED BY DIRECT LASER WRITING	95
6.1. Abstract	95
6.2. Introduction	96
6.3. Experiment and discussion	98
6.4. Conclusion	103
REFERENCES	104
CHAPTER 7: CONCLUSION	107

LIST OF TABLES

TABLE 2.1: All Polymers best-model oscillator parameters, with errors representing the 90% confidence limits of the model parameters.	44
--	----

LIST OF FIGURES

FIGURE 1.1: Optical model used in ellipsometry for thin film characterization. The optical model consists of three layers: ambient (air), thin film, and Si substrate. Note that only the thin film has a finite thickness of t while the ambient and substrate are thought of as semi-infinite.	17
FIGURE 1.2: Calculated dielectric function using a Lorentz oscillator.	21
FIGURE 1.3: Calculated dielectric function from the Tauc-Lorentz model.	23
FIGURE 1.4: Imaginary part of Gaussian-like dielectric function $\varepsilon_2^{\text{Gau}}$ compared with the Lorentz-like dielectric function $\varepsilon_2^{\text{Lor}}$. The parameters (A , E_0 , Γ) are set to the same values (1, 2.5 eV, 1 eV).	24
FIGURE 1.5: The Lorentz sphere optical model used to deduce the Bruggeman effective medium approximation.	26
FIGURE 2.1: Experimental (green dashed lines) and best-model calculated (red solid lines) Mueller matrix spectra of the two-photon polymerized IP-Dip sample with a nominal thickness of 2100 nm for the spectral range from 210 nm to 1500 nm. The angle of incidence was $\Phi_a = 65^\circ$. The data for the sample with a nominal thickness of 3500 nm is omitted here for clarity, but shows also excellent agreement between experimental and best-model calculated line shapes.	40
FIGURE 2.2: Experimental (green dashed lines) and best-model calculated (red solid lines) Mueller matrix spectra of the two-photon polymerized IP-L sample with a nominal thickness of 2900 nm for the spectral range from 210 nm to 1500 nm. The angle of incidence was $\Phi_a = 65^\circ$. The data for the sample with a nominal thickness of 4300 nm is omitted here for clarity, but shows also an excellent agreement between experimental and best-model calculated line shapes.	41

FIGURE 2.3: Experimental (green dashed lines) and best-model calculated (red solid lines) Mueller matrix spectra of the two-photon polymerized IP-S sample with a nominal thickness of 3500 nm for the spectral range from 210 nm to 1500 nm. The angle of incidence was $\Phi_a = 65^\circ$. As for the IP-Dip and IP-L data shown in Figs. 2.1 and 2.2, respectively, the data for the sample with a nominal thickness of 4500 nm is omitted here for clarity, but shows also an excellent agreement between the experimental and best-model calculated line shapes. 42

FIGURE 2.4: The best-fit model refractive index n (red solid line) and extinction coefficient κ (green dashed line) for two-photon polymerized IP-Dip in the spectral range from 210 nm to 1500 nm. The spectrum below 400 nm is dominated by absorption bands, which are described by two oscillators with Tauc-Lorentz and Gaussian broadening. The best-model parameters are summarized in Tab. 2.1. The refractive index of two-photon polymerized (black dashed line) and single-photon polymerized (black dotted line) IP-Dip reported by S. Dottermusch *et al.* and T. Gissibl *et al.*, respectively, are reproduced for comparison [22, 24]. 43

FIGURE 2.5: Same as Fig. 2.4 but for IP-L. IP-L is characterized by a sharp absorption onset which can be described by a single Lorentz oscillator. The best-model parameters are summarized in Tab. 2.1. The refractive index of single-photon polymerized IP-L (black dotted line) reported by T. Gissibl *et al.* is shown for comparison [22]. 44

FIGURE 2.6: Same as Fig. 2.4 but for IP-S, which can be described using two oscillators with Lorentz and Gaussian broadening. The best-model parameters are summarized in Tab. 2.1. In addition to the sharp absorption onset below 300 nm, a small absorption band at 358 nm can be observed. The refractive index of single-photon, UV-cured IP-S (black dotted line) reported by T. Gissibl *et al.* is shown for comparison [22]. 45

FIGURE 2.7: The best-fit model refractive indices n and extinction coefficients κ for the two-photon polymerized IP-Dip, IP-L, and IP-S are reproduced in panel (a) and (b), respectively, for a direct comparison. 46

FIGURE 3.1: Plot of the real part of the effective permittivity $\varepsilon_{\text{ARSS}}$ as a function of the distance in micrometers from the top of the ARSS relative to the substrate, z , from air ($z = 0 \mu\text{m}$) to the substrate ($z = 1 \mu\text{m}$) across the ARSS ($0 \mu\text{m} < z < 1 \mu\text{m}$) based on a Bruggemann effective medium homogenization. The effective permittivity at 5000 cm^{-1} for cone-like ARSS with $f = 0.6, 0.7, 0.8,$ and 0.9 are shown as brown, green, blue, and orange solid lines, respectively. The effective permittivity of air and glass substrate are shown as black solid lines in each corresponding sections. The insert shows the layout of the three individual sections: air, ARSS, and glass substrate. 58

FIGURE 3.2: Nominal design for 3D arrays of the conocoid ARSS with a height of $1 \mu\text{m}$ and $f = 0.6, 0.7, 0.8,$ and 0.9 shown in panels a), b), c), and d), respectively. Scale bars indicate $2 \mu\text{m}$. 59

FIGURE 3.3: SEM micrographs of the conocoid ARSS with a nominal height of $1 \mu\text{m}$ and $f = 0.6, 0.7, 0.8,$ and 0.9 are shown in panels a), b), c), and d), respectively. Note that a SEM micrograph was obtained with the sample tilted by 35° from normal. Scale bars indicate $2 \mu\text{m}$. 60

FIGURE 3.4: 3D arrays of the conocoid ARSS with corrected geometries representative of the as-printed structures for post-comparison with $f = 0.6, 0.7, 0.8,$ and 0.9 shown in panels a), b), c), and d), respectively. Scale bars indicate $2 \mu\text{m}$. 60

FIGURE 3.5: Experimental (a) and 3D-FEM calculated (b) reflectance spectra for $f = 0.6$ (brown), 0.7 (green), 0.8 (blue), and 0.9 (orange). The solid lines represent the calculated data using the nominal conical geometry, whereas the dash dotted lines indicate the approximated as-printed (see Figs. 3.3 and 3.4) more sharply tapered geometries which were re-iterated in COMSOL. 61

FIGURE 3.6: Same as Fig. 3.5 for the experimental and 3D-FEM calculated transmittance data depicted in panels a) and b) respectively. Note that the transmission data were normalized to the bare glass substrate. 63

FIGURE 4.1: Contour plot of relative specular reflectance obtained using 3D-FEM calculations, as a function of angle of incidence ranging from 0° to 30° , for the spectral range from $1.4 \mu\text{m}$ to $2.2 \mu\text{m}$. The geometry of the ARSS is shown in the inset. A lateral spacing $P = 0.9 \mu\text{m}$, cone diameter $D = 0.8 \mu\text{m}$, and cone height $H = 0.83 \mu\text{m}$ was used for the calculations. The complex dielectric properties for IP-Dip were obtained from variable angle spectroscopic ellipsometry measurements [31]. Note that the reflectance of IP-Dip over the corresponding incident angles was used as a reference. 71

FIGURE 4.2: 3D rendering of the nominal design of a bare plano-convex spherical microlens and a corresponding microlens with an ARSS is shown in (a) and (b), respectively. Both microlenses have a base diameter $100 \mu\text{m}$. The inset in panel (b) depicts a closeup of the 3D rendering of the ARSS showing the hexagonal lattice pattern of the conicoid ARSS constituents. Corresponding SEM micrographs of the fabricated bare microlens and the microlens with the conformal ARSS on the convex side are depicted in (c) and (d), respectively. The inset in panel (d) shows a closeup of the ARSS on the microlens. 3D renderings and micrographs were obtained with a 45° tilt with respect to the surface normal. 72

FIGURE 4.3: Relative reflectance (blue solid line) and transmittance (red solid line) spectra of the ARSS treated microlens (Fig. 4.2(b) and (d)) measured by FTIR microscopy in the range from 1.4 to $2.2 \mu\text{m}$ using the absolute reflectance and transmittance of a bare microlens shown in Fig. 4.2(a) and (c) as a reference, respectively. The microlenses were mounted such that convex surface of the microlens faced the Cassegrain objective as shown in the inset. 74

FIGURE 5.1: CAD rendering of the fiber connector. The outer dimensions of the connector are on the mm-scale, while it contains elements with drastically smaller critical dimensions. Located at the left and right of the connector are mechanical guides which are designed to guide a receptacle with high-precision onto the connector. Located within the body of the connector are 12 fiber guides. For demonstration purposes 10 of these fiber guides are bare, 2 are equipped with plano-convex microlenses. One of the microlenses is conformally coated with a structured surface to form a anti-reflection coating (the right microlens in the inset). 84

FIGURE 5.2: Relative reflectance (blue-solid line) and transmittance (red-solid line) spectra of an ARSS-treated microlens (right inset) measured by FTIR microscopy in the range from 1.4 to 2.2 μm using the absolute reflectance and transmittance of a bare microlens (left inset) as a reference, respectively. 86

FIGURE 5.3: Schematic of the fabrication process. (a) illustrates the polymerization of the components which required the lowest spatial resolution. For this purpose a $25\times$ immersion objective was used in combination with IP-S photoresist. (b) after the polymerization the access monomer was removed as described in the text. (c) illustrates the subsequent fabrication of the bare and ARSS coated microlenses. The critical features of microlenses and coatings require resolutions in the μm to nm range. A $63\times$ immersion objective was used in combination with IP-Dip photoresist in order to achieve this resolution. Note, the objective focal lengths, as shown in Fig. 5.3 (a) and (c), are exaggerated for illustration purposes. 87

FIGURE 5.4: Top-view optical micrographs of the fabricated fiber connector showing the entire connector (a), a detailed micrograph of the fiber guides (b), a (c) comparison of a microlens without (left) and with (right) a conformal ARSS coating, and (d) a detailed micrograph of ARSS surface only. The scale bars in (a), (b), (c), and (d) are 2.5 mm, 100 μm , 50 μm , and 10 μm , respectively. 90

FIGURE 6.1: Nominal design for the 1D PCs investigated here. The PCs are composed of alternating compact and low-density polymer layers, as shown in panel (a). The low-density layers are constructed from pillar arrays. Structural dimensions and unit-cell geometry are shown in the inset. Panel (b) shows the corresponding effective medium model of the PCs which consists of alternating layers with different permittivity $\varepsilon_{\text{low}}^{\text{eff}}$ (light blue) and ε_{com} (dark blue), and results in a 1D permittivity variation along the z-axis which is used for the stratified-layer optical model calculations (inset). 98

FIGURE 6.2: SEM micrograph of the polymer PC composed of 12 repeating pairs of compact and low-density layers. The inset depicts the micrograph of a section of the top view of the polymer PC obtained by an optical microscope in transmission revealing the lateral arrangement of the columnar pillars with a circular base in a square lattice pattern. Note that the SEM micrograph was obtained with the sample tilted by 50° relative to the substrate normal. 99

FIGURE 6.3: Experimental (dashed lines) and best-model (solid lines) calculated (b) reflectance and (d) transmittance spectra obtained for the polymer PC shown in Fig. 6.2. The calculated reflectance and transmittance spectra for the nominal geometry are shown for comparison in panels (a) and (c), respectively. 101

FIGURE 6.4: Real (blue lines) and imaginary (orange lines) part of the best-model calculated dielectric function of the low-density (dashed lines) and the compact layers (solid lines) are shown in panels (a) and (b), respectively, for comparison. 102

LIST OF OWN PUBLICATIONS

The following peer-reviewed technical articles have been published as part of this dissertation and are partially included in the following chapters.

1. **Y. Li**, D. Fullager, E. Angelbello, D. Childers, G. Boreman, and T. Hofmann, "Broadband near-infrared antireflection coatings fabricated by three-dimensional direct laser writing," *Opt. Lett.* **43**, 239 (2018).
2. **Y. Li**, D. Fullager, S. Park, D. Childers, R. Fesperman, G. Boreman, and T. Hofmann, "High-contrast infrared polymer photonic crystals fabricated by direct laser writing," *Opt. Lett.* **43**, 4711 (2018).
3. M. Kocherga, J. Castaneda, M. G. Walter, Y. Zhang, N.-A. Saleh, L. Wang, D. S. Jones, J. W. Merkert, B. Donovan-Merkert, **Y. Li**, T. Hofmann, and T. A. Schmedake, "Si(bzimpy)₂-a hexacoordinate silicon pincer complex for electron transport and electroluminescence," *Chem. Comm.* **54**, 14073 (2018).
4. **Y. Li**, S. Park, M. McLamb, M. Lata, S. Schöche, D. Childers, I. Aggarwal, M. Poutous, G. Boreman, and T. Hofmann, "UV to NIR optical properties of IP-Dip, IP-L, and IP-S after two-photon polymerization determined by spectroscopic ellipsometry," *Opt. Mater. Express* **9**, 4318 (2019).
5. **Y. Li**, S. Park, D. B. Fullager, D. Childers, M. K. Poutous, I. D. Aggarwal, G. Boreman, and T. Hofmann, "Near-infrared transmittance enhancement using fully conformal antireflective structured surfaces on microlenses fabricated by direct laser writing," *Opt. Eng.* **58**, 010501 (2019).
6. **Y. Li**, M. Kocherga, S. Park, M. Lata, M. McLamb, G. Boreman, T. A. Schmedake, and T. Hofmann, "Optical dielectric function of Si(2,6-bis(benzimidazol-2'-yl)pyridine)₂ determined by spectroscopic ellipsometry," *Opt. Mater. Express* **9**, 3469 (2019).

7. **Y. Li**, S. Park, M. McLamb, M. Lata, D. Childers, and T. Hofmann, "Fabrication of optical components with nm-to mm-scale critical features using three-dimensional direct laser writing," *IEEE HONET-ICT*, 213 (2019).
8. S. Park, **Y. Li**, D. B. Fullager, S. Schöche, C. M. Herzinger, G. D. Boreman, and T. Hofmann, "Terahertz to mid-infrared dielectric properties of polymethacrylates for stereolithographic single layer assembly," *J. Infrared, Millimeter, Terahertz Waves* **40**, 971 (2019).
9. S. Park, **Y. Li**, D. B. Fullager, M. Lata, P. Kühne, V. Darakchieva, and T. Hofmann, "Terahertz optical properties of polymethacrylates after thermal annealing," *J. Vac. Sci Technol. B* **37**, 062924 (2019).
10. M. Lata, **Y. Li**, S. Park, M. J. McLamb, and T. Hofmann, "Direct laser writing of birefringent photonic crystals for the infrared spectral range," *J. Vac. Sci Technol. B* **37**, 062905 (2019).
11. M. McLamb, **Y. Li**, S. Park, M. Lata, and T. Hofmann, "Diffraction gratings for uniform light extraction from light guides," *IEEE HONET-ICT*, 220 (2019).
12. H. Yu, **Y. Li**, Y. Ji, X. Wu, Y. Yuan, H. Li, and J. Yang, "The propulsion mechanism and tiny particles removal investigation based on the "micro-gun" propulsion system," *Opt. Laser Technol.* **119**, 105627 (2019).
13. R. Duan, **Y. Li**, H. Li, and J. Yang, "Detection of heavy metal ions using whispering gallery mode lasing in functionalized liquid crystal microdroplets," *Biomed. Opt. Express* **10**, 6073 (2019).
14. R. Duan, **Y. Li**, H. Li, and J. Yang, "Real-time monitoring of the enzymatic reaction of urease by using whispering gallery mode lasing," *Opt. Express* **27**, 35427 (2019).

15. S. Park, Z. Z. Clark, **Y. Li**, M. McLamb, and T. Hofmann, "A stereolithographically fabricated polymethacrylate broadband THz absorber," *IEEE HONET-ICT*, 217 (2019).
16. H. Tian, Y. Song, **Y. Li**, and H. Li, "Fiber-optic vector magnetic field sensor based on mode interference and magnetic fluid in a two-channel tapered structure," *IEEE Photonics J.* **11**, 1 (2019).
17. D. B. Fullager, S. Park, C. Hovis, **Y. Li**, J. Reese, E. Sharma, S. Lee, C. Evans, G. D. Boreman, and T. Hofmann, "Metalized poly-methacrylate off-axis parabolic mirrors for terahertz imaging fabricated by additive manufacturing," *J. Infrared, Millimeter, Terahertz Waves* **40**, 269 (2019).
18. H. Li, X. Hao, **Y. Li**, L. Xu, B. Shi, and L. Liu, "Nanoheater-tuned whispering gallery mode lasing in liquid-filled hollow microcavities," *Opt. Lett.* **45**, 815 (2020).
19. R. Duan, X. Hao, **Y. Li**, and H. Li, "Detection of acetylcholinesterase and its inhibitors by liquid crystal biosensor based on whispering gallery mode," *Sens. Actuators, B* **308**, 127672 (2020).

CHAPTER 1: INTRODUCTION

1.1 Overview

The nature of all optical materials and devices originates from light-matter interactions. As light interacts with various materials, numerous optical phenomena are observed, depending on the materials' inherent properties and intrinsic geometries. Based on this, many scientists and researchers have dedicated their efforts to developing optical components either by selecting materials with specific characteristics or by engineering the optical structures with currently available materials. A high volume of studies on the synthesis of novel materials reveal fundamental restrictions on the diversity of optical functionalities, which is limited by the optical properties of naturally occurring materials. Therefore, the realization of extraordinary optical properties, such as negative index with low loss [1, 2], for instance, is impossible by using materials occurring in nature.

Fortunately, the dependence of the optical response on the geometries of sub-wavelength-sized constituents of a metamaterial offers another opportunity that can be leveraged to manipulate the light-matter interaction. In this sense, without changing materials themselves, their properties, as an *effective* medium, can be engineered by rearranging their constituent structures in different geometries. Such artificially introduced geometries are typically in sub-wavelength sized dimensions, meaning that they are smaller than the wavelength of the interacting light, but still large relative to the atomic level of the constituent materials. The macroscopically averaged optical response can be rendered as the one resulting from a homogenized and effective material [3]. Therefore, designing optical structures at scales smaller than the wavelength of interest is an appropriate method to engineer the effective optical properties such

that unusual optical features can be obtained. The development of such artificially structured materials is the theme of this dissertation.

The fabrication of designed optical materials is therefore a central question that we need to address in this dissertation. Fabricating optical structures is challenging, particularly for the creation of the materials operating in the near-infrared (NIR) and visible (VIS) spectral range. Unlike structured materials designed for microwave frequencies, whose dimensions are large enough that they can be often achieved with standard fabrication tools, the structures designed for optical frequencies require the size of unit block at a deep sub-wavelength scale (from tens to a few hundreds nanometers). Therefore, the fabrication of such optical metamaterials requires nano-lithographic instruments.

In past decades, a number of advanced nano-fabrication techniques have been developed. These techniques are now employed for applications in electro-optics [4], solar energy conversion [5], photonic metasurfaces [6], plasmonics [7], etc. For instance, electron beam lithography and focused-ion beam milling are frequently used in lab-environments for the realization of functional surfaces with dielectric/metal unit cell arranged in a certain lattice pattern [8, 9]. Interference lithography on the other hand has been widely applied for the fabrication of gratings and holographic optics [10, 11]. Although these nano-fabrication approaches have been demonstrated to be suitable for the fabrication of two-dimensional patterns, three-dimensional optical structures with spatially arbitrary parameters are difficult to achieve..

Three-dimensional direct laser writing (3D-DWL), is an alternative approach which utilizes two-photon polymerization in order to fabricate three-dimensional structures with dimensions on the sub-micrometer scale. 3D-DWL was most prominently utilized in 2004 when the first photonic crystal was fabricated using this technique [12]. Compared to the other contemporary nano-lithography techniques, the major advantage of the 3D-DWL is its capability of constructing virtually arbitrary 3D geometries

with critical feature dimensions beyond diffraction limit of light in NIR region. Therefore, 3D-DLW is a versatile platform to support the development of NIR functional materials with engineered optical material properties.

In addition to the fabrication and characterization of structured optical materials, we have accurately characterized the optical properties of the metamaterial constituents for the first time. The precise knowledge of the optical properties of the constituent materials is essential in order to reliably estimate the optical response from the effective medium composed of them, using either analytical or numerical calculation approaches. Here, spectroscopic ellipsometry is used for the accurate measurement of the dielectric function of a number of photo-resists (IP-Dip, IP-L, and IP-S) compatible with 3D-DLW techniques and employed here as the constituent materials of the investigated optical structures. Parameterized dielectric function models were developed for these polymers in the near-infrared to UV spectral region for the first time.

Combined with the finite element method (FEM) based numerical modeling tool (COMSOL), several multi-functional, structured optical materials have been theoretically studied and prototyped using 3D-DLW. Along with the exploration of the optical materials studied here, this dissertation emphasizes two aspects: 1) expand the range of the optical responses from dielectrics by engineering the constituent geometries and 2) accomplish critical optical functionalities with simple structural configurations that could benefit industrial applications. Based on this logic, this dissertation is structured as follows. The first chapter gives a brief introduction to the fundamental physics behind the techniques that we used throughout this dissertation. The ellipsometric measurements of the optical properties of the basic constituent materials, i.e., the 3D-DLW based photo-resists, are discussed in detail in chapter 2. Based on the determined parameters of the photo-resists, anti-reflective structured surfaces (ARSS) designed for the reduction of undesired Fresnel losses in optical

fiber communication systems are investigated in chapter 3. As direct applications of ARSS, conformal ARSS treated microlenses incorporated in 3D-DLW-fabricated fiber interconnects with multi-scale features are described in chapters 4 and 5, respectively. These results impressively demonstrate that two-photon polymerization is a promising nano-fabrication strategy that allows for a rapid prototyping of optical fiber components. Opposite to the suppression reflection at the telecommunication wavelength of $1.55 \mu\text{m}$, a highly reflective photonic crystal was developed using 3D-DLW-compatible photoresists. A geometry which had not been explored using 3D-DLW before was implemented to achieve record reflectance values comparable to gold reference standards. The development of the photonic crystal is detailed in chapter 6. Chapter 7 summarizes the dissertation in general and indicates possible avenues for future work.

The theoretical concepts applied in this dissertation derive from linear optics, where it is assumed that the optical properties of materials (i.e., refractive index n and absorption α or extinction coefficient κ) are independent of the amplitude of the externally applied electromagnetic field E . Therefore, linear optical interactions are briefly introduced below. In section 1.2, the physical mechanism of two-photon-polymerization-based lithography that is based on a non-linear optical process is introduced. Spectroscopic ellipsometry and effective medium theory, on the basis of the linear optical theory, are described in detail in sections 1.3 and 1.4, respectively.

Considering linear light-matter interaction, the optical properties of materials are characterized by the complex relative dielectric function ϵ_r , which is derived from the polarization P of a medium through the electric displacement field D :

$$\begin{aligned}
D &= \varepsilon_0 E + P \\
&= \varepsilon_0 E + \varepsilon_0 \chi E \\
&= \varepsilon_0 \varepsilon_r E,
\end{aligned} \tag{1.1}$$

where ε_0 and χ denote the vacuum permittivity and electric susceptibility, respectively. Then, the relative dielectric function ε_r is expressed as:

$$\varepsilon_r = 1 + \chi. \tag{1.2}$$

We know that the complex dielectric function ε_r is a function of the frequency ω of applied electric field E . In order to describe the behavior of ε_r as a function of the frequency ω , a simple physical model can be established by considering a medium wherein the bond electrons with a resonance frequency ω_0 are driven by the sinusoidal electric field E of the electromagnetic wave. In this simple, classical model, the electron, under the influence of the electric field induced driving force, oscillates harmonically around the nucleus, while it is reasonable to ignore the motion of the nucleus in that nuclear mass m_n is much heavier compared to the mass of electrons m_e (i.e., $m_n \gg m_e$). Introducing the displacement of the electron x and using the harmonic oscillator model, the motion of the electron can be expressed as a classical equation of motion:

$$m_e \frac{d^2 x}{dt^2} + m_e \Gamma \frac{dx}{dt} + m_e \omega_0^2 x = -eE, \tag{1.3}$$

where Γ is the damping rate. A non-vanishing Γ results in the lowering and broadening dielectric function described in detail in section 1.3. The electron charge is represented by e . The terms, on the left side of the equation from the left to the

right, are interpreted as the electron's acceleration, damping, and restoring force, respectively. The term on the right-hand side represents the driving force, wherein the electric field is defined as sinusoidal function with respect to time t :

$$E(t) = \frac{1}{2}E_0[\exp(i\omega t) + \exp(-i\omega t)], \quad (1.4)$$

where E_0 and ω denote the amplitude and frequency of the electric field, respectively. It is noteworthy to mention that the propagation associated phase term ϕ is omitted intentionally for simplification, while the omission does not impact the accuracy of the formulas. Substituting the electric field into Eqn. (1.3), the solution of the differential equation yields the following expression for the displacement x , wherein c.c. indicates the complex conjugate:

$$x = -\frac{eE_0}{m_e} \frac{\exp(-i\omega t)}{\omega_0^2 - \omega^2 - i\Gamma\omega} + \text{c.c.} \quad (1.5)$$

The physical interpretation of this solution depicts that the displacement of the electron induces a sinusoidal oscillation centered at the equilibrium position, thus forming a time-varying dipole moment $p(t) = -ex$. Assuming that the number of the atoms per unit volume is N , then the macroscopic polarization P of the medium can be expressed in the form of:

$$\begin{aligned} P &= Np \\ &= -Nex \\ &= \frac{Ne^2}{m_e} \frac{1}{\omega_0^2 - \omega^2 - i\Gamma\omega} E_0 \exp(-i\omega t). \end{aligned} \quad (1.6)$$

Note that c.c. has been omitted in this equation for brevity. Substituting this expression of the macroscopic polarization P into Eqn. (1.1), then the complex relative

dielectric function $\varepsilon_r(\omega)$ is obtained:

$$\begin{aligned}\varepsilon_r(\omega) &= 1 + \chi \\ &= 1 + \frac{Ne^2}{\varepsilon_0 m_e} \frac{1}{\omega_0^2 - \omega^2 - i\Gamma\omega}.\end{aligned}\tag{1.7}$$

Since the complex refractive index \tilde{n} ($\tilde{n} = n + i\kappa$) is equal to the square root of the complex dielectric $\sqrt{\varepsilon_r}$, the refractive index n and extinction coefficient κ , as the real and imaginary parts of the complex refractive index \tilde{n} , are respectively derived as:

$$n = \text{Re}\{\tilde{n}\} = 1 + \frac{Ne^2}{\varepsilon_0 m_e} \frac{\omega_0^2 - \omega^2}{(\omega_0^2 - \omega^2)^2 + (\Gamma\omega)^2},\tag{1.8}$$

$$\kappa = \text{Im}\{\tilde{n}\} = 1 + \frac{Ne^2}{\varepsilon_0 m_e} \frac{\Gamma\omega}{(\omega_0^2 - \omega^2)^2 + (\Gamma\omega)^2}.\tag{1.9}$$

Concerning the frequency dependence of the extinction coefficient κ , one can immediately note that the absorption $\alpha(\omega)$ ($\propto 4\pi\kappa(\omega)$) reaches a maximum as $\omega = \omega_0$. This accounts for the linear absorption process of a single-photon, while two-photon absorption is a nonlinear effect, which is elaborated in the next section.

1.2 Two-photon polymerization lithography

Two-photon polymerization, employed as the main nano-fabrication technique here for the development of optical structures, provides the 3D-DLW a resolution on a sub-micrometer scale (~ 100 nm) [13, 14, 15]. Such a spatial resolution is sufficient to construct structures that can coherently interact with light at wavelengths in infrared spectral range. 3D-DLW has already been established for the fabrication sub-wavelength-sized arbitrary architectures in free space, which is currently difficult to achieve by other conventional lithographic techniques, e.g., nanoimprint, electron-beam lithography, and photolithography. 3D-DLW is currently employing a linear

writing process, thus at present this technique is not suitable for commercial fabrication at scale, but it has been demonstrated in many publications of the last two decades, that this technique has a large potential for lab-based research projects [16, 17]. To have a better understanding of the capability and flexibility of the two-photon polymerization technique, particularly in the research environment, a general introduction to its operation mechanism from theoretical perspective is given in this section.

Two-photon polymerization is a photochemical process where the light-matter interaction occurs as a nonlinear optical effect. A common photo-polymerization process is subject to three sequential parts: 1) photo-initiators become excited by concurrently absorbing two photons and then decompose into radicals; 2) radicals incorporate with monomers to generate monomer radicals; and 3) polymers are formed at the final stage via the combination of the monomer radicals [18, 15]. Additional details about the chemical reaction have been omitted in this section since it falls outside of this dissertation. The interested reader is referred to the relevant literature [18, 19]. The objective here is to give a general introduction into the two-photon absorption process to allow for a better understanding of the two-photon polymerization from optics perspective.

Generally, the two-photon absorption takes place as optical fields interact with molecules in a dissipative way, which stimulates an energy exchange between the optical fields and molecules through absorption. The exchanged energy, per unit time and volume, can be expressed as the time-averaged product of applied electric field E and induced polarization P [19]:

$$\frac{dW}{dt} = \langle E \cdot P \rangle, \quad (1.10)$$

where the brackets indicate a time average over several cycles of the field.

In the previous section regarding linear optics, the relationship between the electric

field E and polarization P is linear. This can be seen in Eqn. (1.1), wherein the optical properties of materials (complex dielectric function ε_r or susceptibility χ), are independent of the intensity of the electric field E . Particularly, the imaginary part of the complex dielectric function ε_r , which corresponds to the absorption and therefore accounts for the energy transformation from the light field to the material medium, is independent of the intensity of E , as shown in Eqn. (1.9). However, this linear treatment is only valid at low power levels. For high intensities that can be achieved by high-power lasers, the optical properties including the absorbing characteristic become power-dependent, i.e., nonlinear optical interaction takes place. In order to take the nonlinear effect into account, it is necessary to remodel the electron motion, where the harmonic oscillation equation shown in Eqn. (1.3) has to be modified by introducing anharmonic terms, as follows:

$$m_e \frac{d^2x}{dt^2} + m_e \Gamma \frac{dx}{dt} + m_e \omega_0^2 x + m_e (C_1 x^2 + C_2 x^3 + \dots) = -eE, \quad (1.11)$$

where the anharmonic terms in increasing orders are summarized inside the parentheses. Assuming that the anharmonicity is small in comparison to the harmonic contribution (i.e., $\omega_0^2 \gg C_1 x \gg C_2 x^2 \dots$), it makes sense to approximate the solution with a power series expansion in the electric field E . Equivalently, the nonlinear polarization P^{NL} is written as a power expansion as follows:

$$\begin{aligned} P^{\text{NL}} &= P^{(1)} + P^{(2)} + P^{(3)} + \dots \\ &= \varepsilon_0 \chi^{(1)} E + \varepsilon_0 \chi^{(2)} E^2 + \varepsilon_0 \chi^{(3)} E^3 + \dots, \end{aligned} \quad (1.12)$$

where the superscripts (n) represent the n th-orders. In analogy to Eqn. (1.2), the nonlinear complex dielectric function ε^{NL} is obtained:

$$\begin{aligned}
\varepsilon_r^{\text{NL}} &= 1 + \chi^{\text{NL}} \\
&= 1 + \chi^{(1)} + \chi^{(2)}E + \chi^{(3)}E^2 + \dots,
\end{aligned}
\tag{1.13}$$

where the 1st-order $\chi^{(1)}$ is the linear susceptibility as the one shown in Eqn. (1.2). While the remaining terms are the n th-order nonlinear susceptibility $\chi^{(n)}$. In this expression, the dielectric function depends on the electric field E through the nonlinear susceptibilities. Likewise, the associated properties (i.e., refractive index and absorption) of materials varies as a function of the strength of the applied electric field E .

The terms $\chi^{(2)}E$ and $\chi^{(3)}E^2$ in the above expression, refer to the second-order and third-order nonlinearities and contribute to the majority of nonlinear phenomena. For instance, the second-order term $\chi^{(2)}E$ usually accounts for sum-frequency generation ($\chi^{(2)}(\omega_1, \omega_2, \omega_3)$ and $\omega_3 = \omega_1 + \omega_2$), but only takes effect for materials without inversion symmetry. In contrast, the third-order term $\chi^{(3)}E^2$ plays an important role in isotropic media, particularly corresponding to the four-frequency mixing process $\chi^{(3)}(\omega_1, \omega_2, \omega_3, \omega_4)$, where the four different frequencies satisfy the relation: $\omega_1 + \omega_2 + \omega_3 + \omega_4 = 0$. Herein, the two-photon absorption belongs to a special type of the four-frequency mixing processes, in which the four frequencies degenerate into an identical frequency from a single input laser beam. With $\omega_1 = \omega_2 = +\omega$ and $\omega_3 = \omega_4 = -\omega$, a charge carrier in molecular system is stimulated and kept at the excited state for producing the radicals as mentioned above. The two-photon absorption is different from the sum-frequency generation in the degenerate case because the end product of the sum-frequency generation is an emission of a photon with the sum frequency instead of maintaining the stimulated charge carriers at the excited state.

The two-photon absorption rate of energy is dominated by the imaginary part of Eqn. (1.10) and can be expressed as [19]:

$$\frac{dW}{dt} = \frac{8\pi^2\omega}{n^2c^2}I^2\text{Im}(\chi^{(3)}), \quad (1.14)$$

where I is the intensity of exciting light, being defined as $I = |E|^2nc/8\pi$, wherein n and c denote the medium refractive index and the speed of light in free space, respectively. Compared to the linear absorption for single-photon processes, the two-photon absorption rate in this expression is quadratically dependent on the light intensity. In addition, the scaling, in particular, between the first- and third-orders of susceptibility (i.e., $\chi^{(1)}/\chi^{(3)}$) is on the order of the 'characteristic atomic field' E_0 ($\sim 2.5 \times 10^{12} \text{ Vm}^{-1}$) [20]. This implies that it requires much higher light intensities to trigger two-photon absorptions at a level compatible to single-photon absorption. For this reason, a ultra-short pulse laser with a very high intensity on the order of TW/cm^2 is required for 3D-DLW. The 3D-DLW system used in this dissertation is equipped with a femtosecond laser at center wavelength of 780 nm with pulse duration of 100 fs, the peak power of which can reach 25 kW.

Based on the above mechanism of the two-photon polymerization process, the advantages can be summarized as follows: A polymerization process which takes advantage of two-photon absorption requires the absorption of two photons in a short period of time in the order of a few hundred femtoseconds. Typically, the frequency of the exciting photons is only half of the ones used for the single-photon polymerization, such that each single photon does not have enough energy to activate the polymerization along its pathway propagating inside the unpolymerized resin. Combining a femtosecond laser source and focusing optics, the polymerization process can only occur at the focal point where the energy is above the polymerization threshold of the photo-resists by a spatial collection of half-frequency photons in the short time interval. This distinguishes the two-photon from single-photon polymerization and

allows the synthesis of three-dimensional geometries with critical features in the μm - and nm-range.

In contrast to traditional single-photon lithography techniques, two-photon polymerization enables the fabrication of structures with a spatial resolution beyond diffraction limit of the wavelength of the light source used in the process. This is due to the cross-section of the light beam at the focal point and the programmable absorption rate which can be addressed using the laser power and exposure time. The fact that the profile of the focused laser beam used for effectively generating two-photon polymerization has a compact beam waist, compared to that used for single-photon polymerization, is understandable through Eqn. (1.14). The two-photon absorption is determined by the squared beam intensity I^2 , instead of I as for single-photon polymerization. The profile of I^2 is narrower than that of I , meaning that the extension of the polymerized volume is expected to be smaller with respect to the diffraction limit. In addition, the polymerized volume can be further reduced either by the decreasing the light intensity or the exposure time, as long as the polymerization threshold is exceeded. Note that the approach of reducing the laser power or/and exposure time for achieving a beyond-diffraction-limit dimension is at the expense of the polymerization strength that may cause undesirable adhesion issues. More details on the influence of the laser power and exposure time on the polymerization strength will be discussed in the following chapters. As for some of the other elements, including the optical system and precision mechanical components, that contribute to the performance of 3D-DLW systems, the interested reader is referred to the literature [15].

1.3 Spectroscopic ellipsometry

In the previous section we have introduced the general concept of 3D-DLW using two-photon polymerization. This chapter will focus on the accurate measurement of the optical properties of a number of photo-resists compatible with two-photon polymerization. Precise knowledge of the optical material properties is crucial for the opti-

cal design and fabrication of structured optical components. Knowledge of the optical properties of the polymers is particularly important as the dielectric function is an input parameter required for numerical simulations or analytical calculations needed to predict the optical performance of the designed metamaterials and thereby serve as a guide for the experiment. To acquire precise complex dielectric function data, spectroscopic ellipsometry is employed here to investigate a number of photo-resists compatible with two-photon polymerization. In the following, the fundamentals of spectroscopic ellipsometry data acquisition and analysis are briefly reviewed.

1.3.1 Jones matrix based ellipsometry for isotropic materials

Spectroscopic ellipsometry is a precision optical measurement technique that is employed to characterize materials through the assessment of the changes in both polarization states and phase of a probing beam reflected of (or transmitted through) a sample.

In reflection configuration, the interaction between a probing light beam and the surface of an isotropic sample can be written using the Jones vector representation [21]:

$$\begin{bmatrix} E_{rp} \\ E_{rs} \end{bmatrix} = \begin{bmatrix} r_{pp} & 0 \\ 0 & r_{ss} \end{bmatrix} \begin{bmatrix} E_{ip} \\ E_{is} \end{bmatrix}, \quad (1.15)$$

where both incident and reflected electric fields (E_i and E_r) are represented by the Jones vectors with a pair of orthogonally polarized components denoted by the subscripts s and p. Here, the s and p subscripts denote the polarization direction perpendicular to and parallel to the plane of incidence, respectively. The 2×2 Jones matrix at the right-hand side characterizes the sample, wherein the on-diagonal elements r_{pp} and r_{ss} are the complex reflection coefficients for p- and s-polarization, respectively. The off-diagonal elements, that delineate anisotropic optical responses, vanish for isotropic materials.

The ellipsometric parameters (Ψ, Δ) , which carry the sample-induced variations in the p-polarization relative to the s-polarization in terms of the magnitude and phase, can be defined as the ratio of the complex reflection coefficients of p- and s-polarizations for isotropic samples [21]:

$$\tan\Psi\exp(i\Delta) \equiv \frac{E_{rp}/E_{ip}}{E_{rs}/E_{is}} \equiv \frac{r_p}{r_s}. \quad (1.16)$$

The reflection coefficients can be written as complex numbers:

$$r_p = |r_p|\exp(i\delta_{rp}), \quad (1.17)$$

$$r_s = |r_s|\exp(i\delta_{rs}). \quad (1.18)$$

Substituting these two expressions into Eqn. (1.16), it follows that

$$\tan\Psi = \frac{|r_p|}{|r_s|}, \quad (1.19)$$

$$\exp(i\Delta) = \exp(i\delta_{rp} - \delta_{rs}). \quad (1.20)$$

Therefore, the ellipsometric parameters Ψ and Δ can be expressed in terms of the reflection coefficients:

$$\Psi = \tan^{-1} \left(\frac{|r_p|}{|r_s|} \right), \quad (1.21)$$

$$\Delta = \arg \left(\exp(i\delta_{rp} - \delta_{rs}) \right). \quad (1.22)$$

Thus, the ellipsometric parameters Ψ and Δ represent the amplitude ratio and phase difference between the reflected p- and s-polarizations, respectively.

1.3.2 Mueller matrix based ellipsometry for isotropic materials

So far, we have introduced the Jones matrix formalism used for the characterization of isotropic materials. The Jones vector is an elegant representation for describing the probing light beam with full polarization; however, it is not a suitable to express partial polarization and depolarization. In order to describe unpolarized or partially polarized light, a generalized ellipsometry formalism based on the Mueller matrix can be used. The Stokes vector S allows the characterization of arbitrary polarization states through four real valued Stokes parameters:

$$S = \begin{pmatrix} S_0 \\ S_1 \\ S_2 \\ S_3 \end{pmatrix} = \begin{pmatrix} I_p + I_s \\ I_p - I_s \\ I_{+45^\circ} - I_{-45^\circ} \\ I_R - I_L \end{pmatrix}. \quad (1.23)$$

Here, S_0 denotes the total light intensity and S_1 represents the light intensity determined by subtracting the light intensity of linear polarization in the s-direction I_s from that in the p-direction I_p . S_2 denotes the intensity difference between the light linearly polarized at $+45^\circ$ (I_{+45°) and -45° (I_{-45°) with respect to the p-direction. S_3 is the light intensity is determined by subtracting the light intensity of left-circular polarization I_L from that of right-circular polarization I_R .

As both incident and reflected light are represented by the Stokes vectors, the Mueller matrix accounts for the optical response of a sample and connects the Stokes vector of the incident light S^{in} with the Stokes vector of the light reflected by the sample S^{ref} :

$$\begin{pmatrix} S_0^{\text{ref}} \\ S_1^{\text{ref}} \\ S_2^{\text{ref}} \\ S_3^{\text{ref}} \end{pmatrix} = \begin{pmatrix} M_{11} & M_{12} & M_{13} & M_{14} \\ M_{21} & M_{22} & M_{23} & M_{24} \\ M_{31} & M_{32} & M_{33} & M_{34} \\ M_{41} & M_{42} & M_{43} & M_{44} \end{pmatrix} \begin{pmatrix} S_0^{\text{in}} \\ S_1^{\text{in}} \\ S_2^{\text{in}} \\ S_3^{\text{in}} \end{pmatrix}. \quad (1.24)$$

The Mueller matrix elements $M_{j,k}$ ($j, k = 1, 2, 3, 4$) are commonly normalized by the M_{11} element such that all elements have values in a range from -1 to 1. Typically, Mueller matrix ellipsometry is employed to examine samples that are either optically anisotropic or depolarizing or both. Here, Mueller matrix ellipsometry was used to account for possible depolarization effects in the visible spectral range. It is interesting to note that if the sample is isotropic and if depolarization is excluded, the Mueller matrix can be written as:

$$MM_{\text{iso}} = \begin{pmatrix} 1 & -\cos 2\Psi & 0 & 0 \\ -\cos 2\Psi & 1 & 0 & 0 \\ 0 & 0 & \sin 2\Psi \cos \Delta & \sin 2\Psi \sin \Delta \\ 0 & 0 & -\sin 2\Psi \sin \Delta & \sin 2\Psi \cos \Delta \end{pmatrix}. \quad (1.25)$$

It can be seen from this representation of the Mueller matrix, that isotropic materials have nonzero valued block-on-diagonal elements (M_{11} , M_{12} , M_{21} , M_{22} , M_{33} , M_{34} , M_{43} , and M_{44}), while the block-off-diagonal elements (M_{13} , M_{14} , M_{23} , M_{24} , M_{31} , M_{32} , M_{41} , and M_{42}) are equal to zero. The Mueller matrix for an isotropic sample is symmetric, i.e., M_{12} and M_{21} are symmetric while M_{34} and M_{43} are anti-symmetric. All the effects described above apply to the measured ellipsometric data for our samples, i.e., the block-off-diagonal elements vanished and only non-trivial block-on-diagonal elements were recorded. This indicates the isotropic characteristics of the photo-resists after 3D-DLW-based preparation.

1.3.3 Interpretation of Ψ and Δ

The previous two sections illustrated that ellipsometric measurements can be conveniently expressed using Jones or Mueller matrices depending on the nature of the sample response. For isotropic samples the Jones matrix is often expressed as ellipsometric parameters Ψ and Δ . The following section will discuss the analysis of experimental ellipsometric data which is necessary in order to extract the dielectric function (including anisotropy) and layer thickness of the sample constituents.

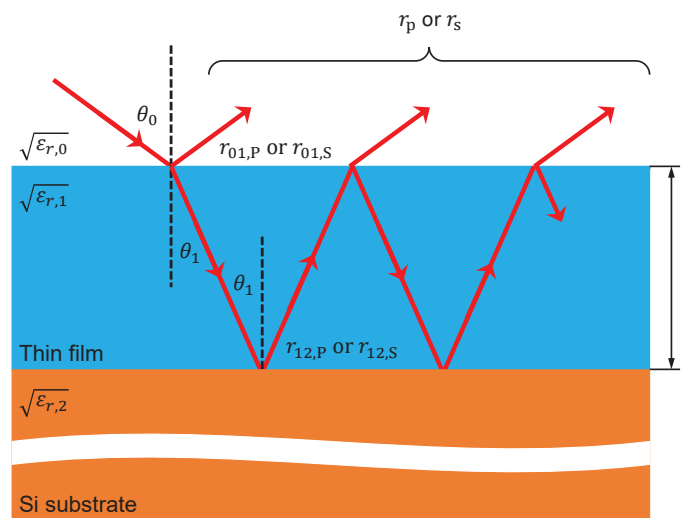


Figure 1.1: Optical model used in ellipsometry for thin film characterization. The optical model consists of three layers: ambient (air), thin film, and Si substrate. Note that only the thin film has a finite thickness of t while the ambient and substrate are thought of as semi-infinite.

As an example, a thin homogeneous and optically isotropic layer deposited on an isotropic and optically opaque substrate is considered here. The optical model required for the sample analysis is composed of three layers: ambient (air)/thin film/substrate, as shown in Fig. 1.1. Note that the effects of interface roughness are not considered in this example for simplicity. As shown in this optical model, the ambient and the substrate are defined as semi-infinite media, meaning that no reflection occurs at the top and bottom boundaries of the optical model. The thin film

is defined as a finite layer with thickness of t . To keep the use of complex dielectric function ε_r throughout this dissertation, let $\sqrt{\varepsilon_{r,0}}$, $\sqrt{\varepsilon_{r,1}}$, and $\sqrt{\varepsilon_{r,2}}$ be the complex refractive indices of air, the thin film, and the substrate, respectively. As the probing light beam is incident on the surface of the sample at an angle of θ_0 and experiences multiple reflections and transmissions within the thin film, the reflection coefficients r_p and r_s for p- and s-polarizations follow the Fresnel formula:

$$r_p = \frac{r_{01,p} + r_{12,p} \exp(-i\phi_{\text{prop}})}{1 + r_{01,p} r_{12,p} \exp(-i\phi_{\text{prop}})}, \quad (1.26)$$

$$r_s = \frac{r_{01,s} + r_{12,s} \exp(-i\phi_{\text{prop}})}{1 + r_{01,s} r_{12,s} \exp(-i\phi_{\text{prop}})}, \quad (1.27)$$

where the reflection coefficients r_{10} and r_{12} for both p- and s-polarizations denote the secondary reflection occurred at the interfaces of ambient/thin film and thin film/substrate, respectively. The term ϕ_{prop} expresses the propagation-induced phase difference for a cycle of light reflected inside the thin film domain. The subscripts a and $b \in \{0, 1, 2\}$ indicate the index of domains. Likewise, both secondary reflection coefficients and propagation-induced phase differences are written in a general form:

$$r_{ab,p} = \frac{\sqrt{\varepsilon_{r,b}} \cos\theta_a - \sqrt{\varepsilon_{r,a}} \cos\theta_b}{\sqrt{\varepsilon_{r,b}} \cos\theta_a + \sqrt{\varepsilon_{r,a}} \cos\theta_b}, \quad (1.28)$$

$$r_{ab,s} = \frac{\sqrt{\varepsilon_{r,a}} \cos\theta_a - \sqrt{\varepsilon_{r,b}} \cos\theta_b}{\sqrt{\varepsilon_{r,a}} \cos\theta_a + \sqrt{\varepsilon_{r,b}} \cos\theta_b}, \quad (1.29)$$

$$\phi_{\text{prop}} = 2 \frac{2\pi t}{\lambda} \sqrt{\varepsilon_{r,1}} \cos\theta_1. \quad (1.30)$$

Combining the equations from Eqn. (1.26) to Eqn. (1.30), only two variables $\varepsilon_{r,1}$ and t , respectively, describing the optical response and the thickness of the thin film, are unknown. These two variables can be retrieved by analyzing the experimentally

obtained ellipsometric parameters.

A correlation between the variables $\varepsilon_{r,1}$ and t is possible for small values of t , which is understandable by reviewing Eqn. (1.30). Adopting multiple measurements at different incident angles on a sample can often resolve this ambiguity. This is because the various incident angles lead to a change in optical path length of the probing beam as it travels through the thin film. This fundamentally increases the number of independent experimental data points [22].

1.3.4 Data analysis

As demonstrated in the previous section, the sample's information in terms of thin film thickness t and dielectric function ε_r is contained in the Jones/Mueller matrix spectra, and their values can be determined from an ellipsometric measurement. Analyzing ellipsometric data can be implemented through two different approaches: the so-called wavelength-by-wavelength analysis and the model dielectric function based analysis.

The wavelength-by-wavelength analysis does not require prior knowledge of the spectral dependence of the dielectric functions of the sample constituents. The extracted spectral points of the samples' dielectric function are treated independently. For isotropic bulk materials, a direct inversion of the experimental Ψ and Δ values to the sample's complex dielectric function can be obtained. In case of stratified samples, this direct conversion is not possible and the sample constituent layer thicknesses must be considered correctly. The Kramers-Kronig consistency of the extracted dielectric function must be verified.

The model dielectric function based analysis on the other hand ensures Kramers-Kronig consistency through proper selection of suitable model dielectric functions. This approach further prevents measurement noise from becoming part of the extracted material dielectric function. In addition, this approach allows access to physically relevant parameters, which can be extracted as fit-parameters of the model

dielectric function.

During the data analysis mentioned above, the physically relevant parameters (such as for instance resonance frequencies, amplitudes, broadenings, and layer thickness) are varied until a best-fit of the experimental and the optical model calculated data is obtained. Here, the Levenberg-Marguardt algorithm is adopted for the fitting process. This algorithm minimizes the mean square error (MSE), which is defined as the mismatch between the calculated and measured data sets given by:

$$MSE = \sqrt{\frac{1}{2N - M} \sum_{i=1}^N \left[\left(\frac{\Psi_i^{\text{Cal}} - \Psi_i^{\text{Exp}}}{\sigma_{\Psi,i}^{\text{Exp}}} \right)^2 + \left(\frac{\Delta_i^{\text{Cal}} - \Delta_i^{\text{Exp}}}{\sigma_{\Delta,i}^{\text{Exp}}} \right)^2 \right]}, \quad (1.31)$$

where N is the number of measured ellipsometric data pairs Ψ and Δ , and M is the total number of the parameters in the optical model. $(\Psi_i^{\text{Cal}}, \Delta_i^{\text{Cal}})$ and $(\Psi_i^{\text{Exp}}, \Delta_i^{\text{Exp}})$ are the calculated and experimental ellipsometric data sets, respectively, $\sigma_{\Psi,i}$ and $\sigma_{\Delta,i}$ are experimental standard deviations of the Ψ_i^{Exp} and Δ_i^{Exp} data points, respectively. In this dissertation, three types of oscillation (i.e., Lorentz, Tauc-Lorentz, and Gaussian oscillations) are used to constitute the parameterized model dielectric functions for the characterization of the photo-resists compatible with two-photon polymerization.

Lorentz oscillation: Recalling Eqn. (1.2), the dielectric function can be thought of as a superposition of all possible contributions and hereby rewritten in a form:

$$\varepsilon_r = 1 + \sum_{n=1} \chi_n. \quad (1.32)$$

The dielectric function based on the Lorentz oscillator model has been discussed in the beginning of this chapter (see Eqn. (1.7)). We express all the oscillations with respect to the photon energy, which is proportional to the photon frequency ω by the relation of $E = \hbar\omega$, where \hbar is the reduced Planck constant. The susceptibility tensor

of Lorentz in Eqn. (1.7) is:

$$\chi_{\text{Lor}} = \frac{A}{E_0^2 - E^2 - i\Gamma E}, \quad (1.33)$$

where A replaces the proportional terms $Ne^2/\varepsilon_0 m_e$ in Eqn. (1.7), representing the oscillator amplitude. The Lorentz oscillation is a classic model that can be useful to describe a resonant absorption process occurring at a frequency with the energy E_0 . Figure 1.2 shows the real and imaginary part of a Lorentz-like dielectric function for $A = 1$ and $\Gamma = 1\text{ eV}$. E_0 is located at 2.5 eV.

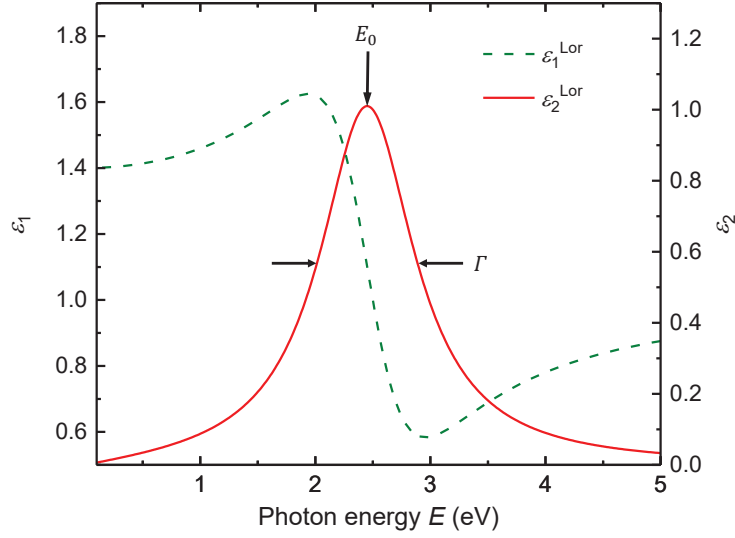


Figure 1.2: Calculated dielectric function using a Lorentz oscillator.

Tauc-Lorentz oscillation: The Tauc-Lorentz oscillation is often employed to model the dielectric function of amorphous materials which possess high-energy band-gaps close to the ultra violet spectral region [23]. Unlike the Lorentz oscillation that has a symmetric lineshape of $\varepsilon_2^{\text{Lor}}$, the imaginary part $\varepsilon_2^{\text{TL}}$ of the Tauc-Lorentz dielectric function exhibits an asymmetric absorption peak. Taking the effect of the energy band-gap into account, $\varepsilon_2^{\text{TL}}$ is expressed from the product of the Tauc gap function and the Lorentz oscillation, as follows [23]:

$$\varepsilon_2^{\text{TL}}(E) = \begin{cases} \frac{AE_0\Gamma(E-E_g)^2}{(E^2-E_0^2)^2+\Gamma^2E^2} \cdot \frac{1}{E} & E > E_g \\ 0 & E \leq E_g \end{cases} \quad (1.34)$$

where E_g denotes the Tauc energy band-gap. From this equation, it can be seen that the value of $\varepsilon_2^{\text{TL}}$ is vanishing for probing light with an energy less than E_g . Based on the Kramers-Kronig relations, the real part $\varepsilon_1^{\text{TL}}$ can be derived from $\varepsilon_2^{\text{TL}}$ in Eqn. (1.34), and is given in a closed form [24]:

$$\begin{aligned} \varepsilon_1^{\text{TL}}(E) = & \varepsilon_1^{\text{TL}}(\infty) + \frac{A\Gamma}{\pi\xi^4} \frac{a_{\text{ln}}}{2\alpha E_0} \ln \left(\frac{E_0^2 + E_g^2 + \alpha E_g}{E_0^2 + E_g^2 - \alpha E_g} \right) \\ & - \frac{A}{\pi\xi^4} \frac{a_{\text{tan}}}{E_0} \left[\pi - \tan^{-1} \left(\frac{2E_g + \alpha}{\Gamma} \right) + \tan^{-1} \left(\frac{-2E_g + \alpha}{\Gamma} \right) \right] \\ & + 2 \frac{AE_0}{\pi\xi^4 \alpha} E_g (E_2 - \gamma^2) \left[\pi + 2 \tan^{-1} \left(a \frac{\gamma^2 - E_g^2}{\alpha \Gamma} \right) \right] \\ & - \frac{AE_0\Gamma}{\pi\xi^4} \frac{E^2 + E_g^2}{E} \ln \left(\frac{|E - E_g|}{E + E_g} \right) + \frac{2AE_0\Gamma}{\pi\xi^4} E_g \ln \left[\frac{|E - E_g|(E + E_g)}{\sqrt{(E_0^2 - E_g^2)^2 + E_g^2 \Gamma^2}} \right], \end{aligned} \quad (1.35)$$

where

$$a_{\text{ln}} = (E_g^2 - E_0^2)E_2 + E_g^2\Gamma^2 - E_0^2(E_0^2 + 3E_g^2), \quad (1.36a)$$

$$a_{\text{tan}} = (E^2 - E_0^2)(E_0^2 + E_g^2) + E_g^2\Gamma^2, \quad (1.36b)$$

$$\xi^4 = (E^2 - \gamma^2)^2 + \alpha^2\Gamma^2/4, \quad (1.36c)$$

$$\alpha = \sqrt{4E_0^2 - \Gamma^2}, \quad (1.36d)$$

$$\gamma = \sqrt{E_0^2 - \Gamma^2/2}. \quad (1.36e)$$

The equation of $\varepsilon_1^{\text{TL}}$ seems to be rather complicated at first glance; however, only five parameters ($\varepsilon_1^{\text{TL}}(\infty)$, A , E_0 , Γ , E_g) control its shape. $\varepsilon_1^{\text{TL}}(\infty)$ is a constant to model the dielectric response to electric fields at the high-frequency limit ($\omega \sim$

∞). Figure 1.3 depicts the real and imaginary parts of the Tauc-Lorentz model. As expected, $\varepsilon_2^{\text{TL}}$ reaches the highest value at the resonance energy E_0 and vanishes for energies at and after the Tauc band-gap energy E_g . The oscillation strength and the half width of the Tauc-Lorentz oscillation are represented by A and Γ , respectively, which are analogous to the Lorentz oscillation.

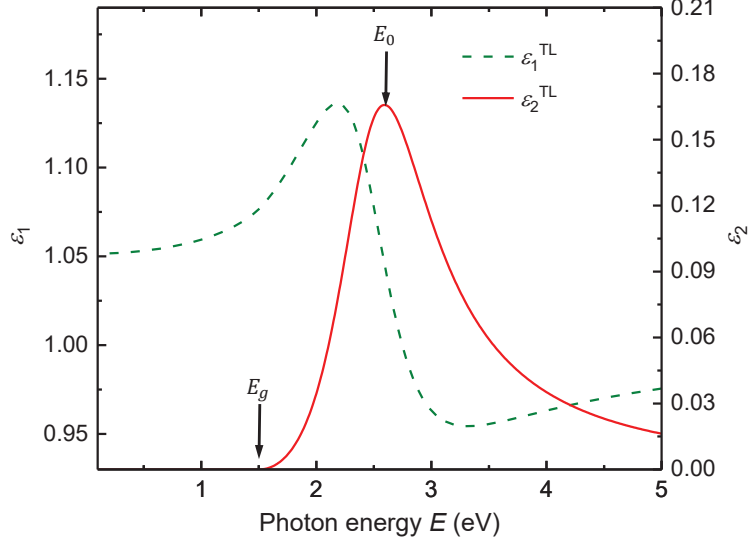


Figure 1.3: Calculated dielectric function from the Tauc-Lorentz model.

Gaussian oscillation: The Gaussian oscillation is a good optical model for capturing isolated absorption features in high energy regions such as the ultra violet spectral range [25]. This is because the imaginary part of the Gaussian oscillation $\varepsilon_2^{\text{Gau}}$ produces a symmetric lineshape similar to the Lorentz oscillation, while it rapidly decreases to zero away from the resonance energy. Thus, it can effectively isolate a single and sharp absorption peak while reducing any contributions at frequencies other than frequencies in close proximity to the resonant frequency. The expression for $\varepsilon_2^{\text{Gau}}$ is given by [25]:

$$\varepsilon_2^{\text{Gau}} = Ae^{-\left(\frac{E-E_0}{f\cdot\Gamma}\right)^2} - Ae^{-\left(\frac{E+E_0}{f\cdot\Gamma}\right)^2}, \quad (1.37)$$

where the constant $f = 1/2\sqrt{\ln(2)}$ in Eqn. (1.37) defines full width at half maximum for broadening Γ . The real part of the Gaussian oscillation $\varepsilon_1^{\text{Gau}}$ is obtained by Kramers-Kronig integration of $\varepsilon_2^{\text{Gau}}$, given by [25]:

$$\varepsilon_1^{\text{Gau}} = \frac{2}{\pi} P \int_0^\infty \frac{E' \varepsilon_2^{\text{Gau}}}{E'^2 - E^2} dE', \quad (1.38)$$

where P indicates that we take the principal part of the integral. To explicitly emphasize on the faster reduction of $\varepsilon_2^{\text{Gau}}$ compared to $\varepsilon_2^{\text{Lor}}$, Fig. 1.4 shows the dielectric function with a Gaussian lineshape along with the imaginary part obtained from a Lorentz oscillator, wherein all the critical parameters (A , E_0 , Γ) are set to the same values (1, 2.5 eV, 1 eV). It can be seen from the comparison that although both lineshapes of $\varepsilon_2^{\text{Gau}}$ and $\varepsilon_2^{\text{Lor}}$ have an identical FWHM (full width at half maximum), $\varepsilon_2^{\text{Gau}}$ has a steeper curve and falls to zero faster compared to that of $\varepsilon_2^{\text{Lor}}$.

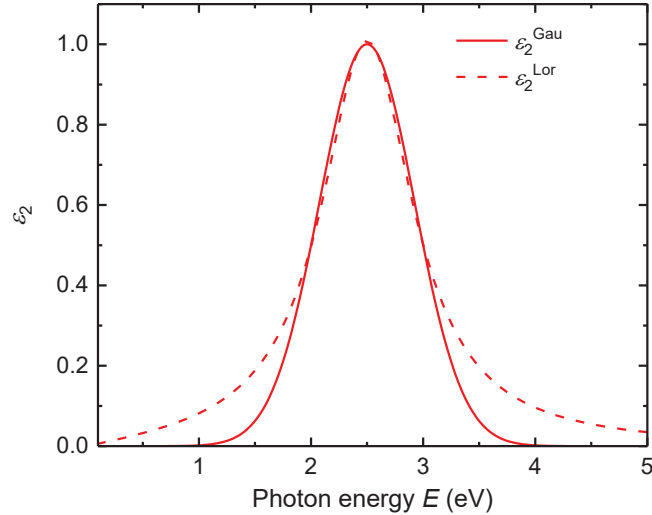


Figure 1.4: Imaginary part of Gaussian-like dielectric function $\varepsilon_2^{\text{Gau}}$ compared with the Lorentz-like dielectric function $\varepsilon_2^{\text{Lor}}$. The parameters (A , E_0 , Γ) are set to the same values (1, 2.5 eV, 1 eV).

1.4 Effective medium theory

The light-matter interaction investigated so far rested on an optical model where the boundary between each constituent layer is abrupt and the electromagnetic response can be easily solved by using Maxwell's equations. This optical model is suitable for evaluating the optical response of a material that is microscopically homogeneous. However, for a compound that is composed of multiple dielectrics interspersing with each other in a either disordered or ordered manner, the assumption of homogeneity at the microscopic scale is no longer valid. To accurately describe the optical properties of such composite materials, it is necessary to study the electromagnetic scattering of the individual constituent dielectrics, from which an effective dielectric function of the macroscopically uniform medium can be deduced. Generally, the effective dielectric function is derived from two types of parameters: 1) the permittivities of the constituent materials and 2) their respective volume fractions. This approach is well known as effective medium approximation (EMA). Several approaches for EMA models have been reported, including Bruggeman EMA [26], Maxwell-Garnett theory [27], and Looyenga's formula [28], for instance. These approaches account for different composite topologies and constituent material properties in the mixture. Among these EMA methods, the Bruggeman EMA gives the best approximation to characterize the effective properties of the optical structures that we designed and fabricated in this dissertation. Therefore, in this section, our focus will be on the review of the Bruggeman EMA.

In a two-constituent based mixture, one is thought of as the "inclusion", while the other component is thought to embed the inclusion and referred to as the "host". As the density of the inclusion rises up at a point where the inclusion and host materials cannot be differentiated topologically and intermingle with each other in a symmetric manner, this type of mixture environment is referred to as Bruggeman topology.

Without losing generality, we start with the inclusions that are imagined to be

distributed in a square lattice pattern in vacuum. Figure 1.5 shows that an isolated unit volume, as encircled by a Lorentz sphere with radius r , includes a number of atomic inclusions suspended in the vacuum. The value of the radius r is set such that the Lorentz sphere is microscopically large so that the surrounding space can be considered as a continuous medium.

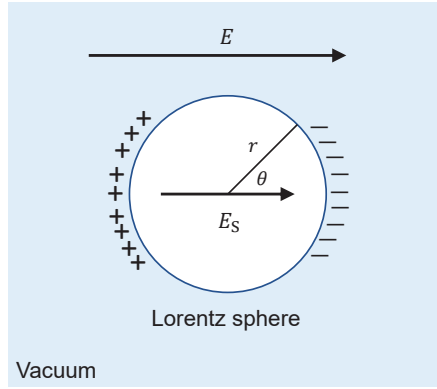


Figure 1.5: The Lorentz sphere optical model used to deduce the Bruggeman effective medium approximation.

As exposed to an external electric field E , the electric field experienced by the local dielectric particles (as shown in Fig. 1.5) is not only the macroscopically averaged field E as shown in Eqn. (1.1), but also the scattering field E_S incurred from the polarization charges accumulated on the outside surface of the Lorentz sphere. Therefore, the local field E_L is:

$$E_L = E + E_S. \quad (1.39)$$

The evaluation of the scattering field E_S can be obtained on the basis of Coulomb's law, as follows:

$$E_S = \int_0^\pi \frac{P \cos^2 \theta}{4\pi \epsilon_0 r^2} \cdot 2\pi r^2 \sin \theta d\theta = \frac{P}{3\epsilon_0}, \quad (1.40)$$

here, P is the dielectric polarization as given in Eqn. (1.6). The term in the numerator $P\cos^2\theta$ accounts for the polarization charge density on the surface of the Lorentz sphere, where $\cos^2\theta$ denotes the surface-charge-induced electric field along the radial direction. The local electric field can be rewritten by:

$$E_L = E + \frac{P}{3\epsilon_0}. \quad (1.41)$$

This Lorentz relationship is well-known for demonstrating that the electric field exerting on a localized atom in a cubic lattice is the sum of the macroscopic field E and the scattering field $P/3\epsilon_0$ induced from the surrounding atoms. It is also clear that E_L increases along with the increasing of the dielectric polarization P . Note that P can be related to the dipole moment of each atom contained in the medium via an expression:

$$P = N\alpha E_L = N\alpha \left(E + \frac{P}{3\epsilon_0} \right). \quad (1.42)$$

Similar to the polarization in Eqn. (1.6), here, N is the number of atoms in an unit volume and α represents the polarizability of the atoms. By associating this dielectric polarization P with the displacement expression in Eqn. (1.1), a formula, commonly known as the Clausius-Mossotti relation, is obtained:

$$\frac{N\alpha}{3\epsilon_0} = \frac{\epsilon - 1}{\epsilon + 2}, \quad (1.43)$$

where

$$\alpha = \frac{3\epsilon_0}{N} \frac{\epsilon - 1}{\epsilon + 2}. \quad (1.44)$$

Assuming that the dielectric particles (inclusions) comprise of two types of components A and B , then the above equation can be modified as:

$$\begin{aligned}\frac{\varepsilon - 1}{\varepsilon + 2} &= \frac{1}{3\varepsilon_0} (N_A\alpha_A + N_B\alpha_B), \\ &= f_A \frac{\varepsilon_A - 1}{\varepsilon_A + 2} + f_B \frac{\varepsilon_B - 1}{\varepsilon_B + 2},\end{aligned}\tag{1.45}$$

where ε_A and ε_B are the dielectric functions of the components A and B , respectively, and the respective volume fractions are f_A and f_B , which obey the relation: $f_A + f_B = 1$. Assuming that the constituents are immersed in a host material with a dielectric function ε_h , Eqn. (1.45) is rewritten as:

$$\frac{\varepsilon - \varepsilon_h}{\varepsilon + 2\varepsilon_h} = f_A \frac{\varepsilon_A - \varepsilon_h}{\varepsilon_A + 2\varepsilon_h} + (1 - f_A) \frac{\varepsilon_B - \varepsilon_h}{\varepsilon_B + 2\varepsilon_h}.\tag{1.46}$$

According to the assumption for the Bruggeman's topology, the permittivities of the two constituents ε_A and ε_B are interchangeable without varying the value of ε . Therefore, each constituent can be thought of as an inclusion, and the previously defined host medium is the composite material itself, indicating $\varepsilon = \varepsilon_h$. Therefore, the Bruggeman EMA for two-dielectric-based composite is expressed as:

$$f_A \frac{\varepsilon_A - \varepsilon}{\varepsilon_A + 2\varepsilon} + (1 - f_A) \frac{\varepsilon_B - \varepsilon}{\varepsilon_B + 2\varepsilon} = 0.\tag{1.47}$$

Based on this equation, the generalized Bruggeman EMA for a material consisting of n constituents is given by:

$$\sum_{i=1}^n f_i \frac{\varepsilon_i - \varepsilon}{\varepsilon_i + 2\varepsilon} = 0, \quad \sum_{i=1}^n f_i = 1.\tag{1.48}$$

After solving Eqn. (1.47), the effective dielectric function of a material composed of two constituents yields [29]:

$$\varepsilon = \frac{1}{4} \left\{ (3f_A - 1)\varepsilon_A + (3f_B - 1)\varepsilon_B \pm \sqrt{[(3f_A - 1)\varepsilon_A + (3f_B - 1)\varepsilon_B]^2 + 8\varepsilon_A\varepsilon_B} \right\}. \quad (1.49)$$

The selection of the sign “ \pm ” in the expression is subject to the fact that the imaginary part of the effective dielectric function must be a positive value.

REFERENCES

- [1] V. M. Shalaev, “Optical negative-index metamaterials,” *Nat. Photonics* **1**, 41 (2007).
- [2] D. R. Smith, J. B. Pendry, and M. C. Wiltshire, “Metamaterials and negative refractive index,” *Science* **305**, 788 (2004).
- [3] D. R. Smith, W. J. Padilla, D. Vier, S. C. Nemat-Nasser, and S. Schultz, “Composite medium with simultaneously negative permeability and permittivity,” *Phys. Rev. Lett.* **84**, 4184 (2000).
- [4] I. Trushkov and I. Iorsh, “Two-dimensional hyperbolic medium for electrons and photons based on the array of tunnel-coupled graphene nanoribbons,” *Phys. Rev. B* **92**, 045305 (2015).
- [5] Z. He, C. Zhong, S. Su, M. Xu, H. Wu, and Y. Cao, “Enhanced power-conversion efficiency in polymer solar cells using an inverted device structure,” *Nat. Photonics* **6**, 591 (2012).
- [6] X. Yin, Z. Ye, J. Rho, Y. Wang, and X. Zhang, “Photonic spin hall effect at metasurfaces,” *Science* **339**, 1405 (2013).
- [7] E. Karimi, S. A. Schulz, I. De Leon, H. Qassim, J. Upham, and R. W. Boyd, “Generating optical orbital angular momentum at visible wavelengths using a plasmonic metasurface,” *Light Sci. Appl.* **3**, e167 (2014).
- [8] T. W. Ebbesen, H. J. Lezec, H. Ghaemi, T. Thio, and P. A. Wolff, “Extraordi-

- nary optical transmission through sub-wavelength hole arrays,” *Nature* **391**, 667 (1998).
- [9] E.-B. Kley, B. Schnabel, and U. D. Zeitner, “E-beam lithography: an efficient tool for the fabrication of diffractive and micro-optical elements,” in Proc. SPIE, vol. 3008, 222–232, (International Society for Optics and Photonics, 1997).
- [10] C. Joenathan, Y. Li, W. Oh, R. M. Bunch, A. Bernal, and S. R. Kirkpatrick, “White light lateral shear interferometer with holographic shear lenses and spatial fourier transform,” *Opt. Lett.* **38**, 4896 (2013).
- [11] C. Joenathan, A. Bernal, Y. Woonghee, Y. Li, and W. Oh, “Analysis of the quantitative measurement for a lateral shear interferometer in a convergent beam mode using fourier transform method,” *Opt. Eng.* **53**, 054109 (2014).
- [12] M. Deubel, G. Von Freymann, M. Wegener, S. Pereira, K. Busch, and C. M. Soukoulis, “Direct laser writing of three-dimensional photonic-crystal templates for telecommunications,” *Nat. Mater.* **3**, 444 (2004).
- [13] S. Kawata, H.-B. Sun, T. Tanaka, and K. Takada, “Finer features for functional microdevices,” *Nature* **412**, 697 (2001).
- [14] J. Serbin, A. Egbert, A. Ostendorf, B. Chichkov, R. Houbertz, G. Domann, J. Schulz, C. Cronauer, L. Fröhlich, and M. Popall, “Femtosecond laser-induced two-photon polymerization of inorganic–organic hybrid materials for applications in photonics,” *Opt. Lett.* **28**, 301 (2003).
- [15] X. Zhou, Y. Hou, and J. Lin, “A review on the processing accuracy of two-photon polymerization,” *AIP Adv.* **5**, 030701 (2015).
- [16] Y. Li, D. Fullager, E. Angelbello, D. Childers, G. Boreman, and T. Hofmann,

- “Broadband near-infrared antireflection coatings fabricated by three-dimensional direct laser writing,” *Opt. Lett.* **43**, 239 (2018).
- [17] Y. Li, D. Fullager, S. Park, D. Childers, R. Fesperman, G. Boreman, and T. Hofmann, “High-contrast infrared polymer photonic crystals fabricated by direct laser writing,” *Opt. Lett.* **43**, 4711 (2018).
- [18] S. Maruo, O. Nakamura, and S. Kawata, “Three-dimensional microfabrication with two-photon-absorbed photopolymerization,” *Opt. Lett.* **22**, 132 (1997).
- [19] G. H. J.D. Bhawalkar and P. Prasad, “Nonlinear multiphoton processes in organic and polymeric materials,” *Rep. Prog. Phys.* **59**, 1041 (1996).
- [20] A. Hayat, A. Nevet, P. Ginzburg, and M. Orenstein, “Applications of two-photon processes in semiconductor photonic devices: invited review,” *Semicond. Sci. Technol.* **26**, 083001 (2011).
- [21] H. Fujiwara, *Spectroscopic Ellipsometry Principles and Applications*, (John Wiley & Sons Inc., Hoboken, NJ 07030, USA, 2007).
- [22] C. Herzinger, B. Johs, W. McGahan, J. A. Woollam, and W. Paulson, “Ellipsometric determination of optical constants for silicon and thermally grown silicon dioxide via a multi-sample, multi-wavelength, multi-angle investigation,” *J. Appl. Phys.* **83**, 3323 (1998).
- [23] G. Jellison Jr and F. Modine, “Parameterization of the optical functions of amorphous materials in the interband region,” *Appl. Phys. Lett.* **69**, 371 (1996).
- [24] J. G. E. Jellison and F. A. Modine, “Erratum: “Parameterization of the optical functions of amorphous materials in the interband region” [*Appl. Phys. Lett.* **69**, 371 (1996)],” *Appl. Phys. Lett.* **69**, 2137 (1996).

- [25] R. Synowicki and T. E. Tiwald, "Optical properties of bulk c-ZrO₂, c-MgO and a-As₂S₃ determined by variable angle spectroscopic ellipsometry," *Thin Solid Films* **455**, 248 (2004).
- [26] D. Bruggeman, "Dielectric constant and conductivity of mixtures of isotropic materials," *Ann. Phys. (Leipzig)* **24**, 636 (1935).
- [27] J. M. Garnett, "Xii. colours in metal glasses and in metallic films," *Phil. Trans. R. So. London* **203**, 385 (1904).
- [28] H. Looyenga, "Dielectric constants of heterogeneous mixtures," *Physica* **31**, 401 (1965).
- [29] W. Cai and V. Shalaev, *Optical metamaterials: fundamentals and applications*, (Springer Science & Business Media, 2009).

CHAPTER 2: UV TO NIR OPTICAL PROPERTIES OF IP-DIP, IP-L, AND IP-S AFTER TWO-PHOTON POLYMERIZATION DETERMINED BY SPECTROSCOPIC ELLIPSOMETRY¹

2.1 Abstract

The polymers IP-Dip, IP-L, and IP-S are among the most commonly used photoresists employed for rapid prototyping of optical components using two-photon polymerization. Despite the widespread use of these polymers, measured data on their optical properties is scarce. Recently, the refractive index n of these polymers has been determined in the visible and near-infrared spectral range. However, the accurate optical properties including extinction coefficient κ in the ultraviolet spectral range have not been reported yet. Here we report on accurate, ellipsometric measurements of the complex dielectric functions of two-photon polymerized IP-Dip, IP-L, and IP-S in the spectral range from 210 nm to 1500 nm. Model dielectric functions composed of oscillators with Lorentz, Gaussian, and Tauc-Lorentz broadenings are presented for all investigated polymers.

2.2 Introduction

Three-dimensional direct laser writing (3D-DLW) based on two-photon polymerization has enabled the fabrication of optical components composed of sub-wavelength-sized elements, forming virtually arbitrary architectures in free space [1]. First demonstrated in 2004 for the synthesis of infrared photonic crystals [2], two-photon polymerization is now widely employed for the synthesis of three-dimensional structures with a spatial resolution ranging from nm- to μm -scales [3, 4, 5]. Contemporary

¹Y. Li, T. Hofmann, *et al.*, *Opt. Mater. Express* **9**, 4318 (2019), **Editor's Pick**. Reprinted with permission © The Optical Society.

applications of this technique have enabled the fabrication of complex optical components [6, 7, 8]. Recently, 3D-DLW has been successfully employed for the synthesis of metamaterials [9, 10, 11, 12]. The optical components and materials fabricated using 3D-DLW cover a very wide spectral range from the ultraviolet (UV) through the visible (VIS) to the near-infrared (NIR) [13, 14, 15, 16, 17]. In addition, 3D-DLW-based fabrication of micro-optical elements with functional coatings and the manufacturing of metasurfaces have attracted much attention [18, 19, 8, 20, 21].

Despite the demonstration of optical components using 3D-DLW-based fabrication techniques, reports on the optical properties of 3D-DLW-compatible polymers are still scarce [22, 23, 24]. This lack of accurate knowledge of the optical constants of 3D-DLW-compatible polymers impedes further advances in the design and optimization of novel metamaterials and optical components fabricated using 3D-DLW-based approaches.

We have recently reported on the infrared complex dielectric functions of two commercially available and frequently employed 3D-DLW-compatible polymers IP-Dip and IP-L (Nanoscribe GmbH) determined using spectroscopic ellipsometry in the infrared spectral range from $1.67 \mu\text{m}$ to $40 \mu\text{m}$ [23]. T. Gissibl *et al.* extended the spectral range towards the visible spectral region from 400 nm to 900 nm by determining the refractive indices n of the UV-cured polymers including IP-Dip, IP-L, and IP-S using refractometry [22]. Recently, S. Dottermusch *et al.* have further explored the exposure-dependent refractive index of IP-Dip in the spectral range from 400 nm to 1550 nm [24]. An index difference Δn of up to 0.01 between single-photon polymerized (UV-cured) and two-photon polymerized IP-Dip was found. However, these recent reports focused exclusively on the transparent region of single-photon polymerized polymers [22] and the extinction coefficient κ has only been reported for single-photon polymerized IP-Dip so far [24]. The complex refractive index of two-photon polymerized IP-Dip, IP-L, and IP-S in the spectral range from 210 nm

to 400 nm has not been reported yet. Furthermore, parameterized dielectric function models are currently not available for these two-photon polymerized materials in the spectral range from 210 nm to 1500 nm.

In this paper, we report on the complex dielectric functions of two-photon polymerized IP-Dip, IP-L, and IP-S in the UV–VIS–NIR spectral range (210 nm to 1500 nm) determined using spectroscopic ellipsometry. A parameterized dielectric function model composed of a sum of oscillators with Gaussian, Lorentz, and Tauc-Lorentz broadenings is used to accurately describe the optical response of these polymers in the measured spectral range. A good agreement is found between the refractive index obtained here and the previous reports which focused on the transparent spectral range from 400 nm to 900 nm [22, 24]. Common for all investigated polymers is the strong absorption for wavelengths below 400 nm, but the number, strength, amplitude, and broadening of the observed absorption bands differ substantially between two-photon polymerized IP-Dip, IP-L, and IP-S.

2.3 Experiment

2.3.1 Sample preparation

Here the focus is on three commonly used, 3D-DLW-compatible polymers, which are commercially available as IP-Dip, IP-L, and IP-S (Nanoscribe, GmbH). The difference in viscosity between IP-Dip, IP-L, and IP-S allows the fabrication of structures with a wide range of critical dimensions in the nm to the μm range [25, 26, 13]. For each polymer, two samples in the shape of rectangular cuboids with a $100\ \mu\text{m} \times 100\ \mu\text{m}$ base and two different heights were fabricated on Si substrates using a commercially available 3D-DLW system (Photonic Professional GT, Nanoscribe, GmbH). The nominal heights for the samples ranged between 2000 nm to 4500 nm. Prior to the 3D-DLW fabrication, the Si substrates were rinsed with Acetone and Methanol. All samples were fabricated in a single 3D-DLW fabrication step. A $25\times$ objective was employed. This allows the fabrication of the rectangular

cuboids by steering the laser beam with the galvanometer scanner of the 3D-DLW system. This approach dispenses with the need for any mechanical translation of the sample stage and thereby avoids possible stitching and over-exposure errors that may be induced by a mechanical translation of the sample [27]. A laser power and scan speed of 90% and 20000 $\mu\text{m}/\text{s}$ (nominal DeScribe settings, Nanoscribe GmbH), respectively, were used to minimize fabrication time while preventing over-exposure. After the fabrication, any unpolymerized monomer was removed by immersing the samples in propylene glycol monomethyl ether acetate (PGMEA, Baker 220) for 20 min. Subsequently, the samples were immersed in 99.99% isopropyl alcohol for 2 min. Finally, the remaining isopropyl alcohol was evaporated at room temperature.

2.3.2 Data acquisition and analysis

The IP-Dip, IP-L, and IP-S samples were investigated using a commercial spectroscopic ellipsometer (RC2[®], J.A. Woollam Company Inc.) in the spectral range from 210 nm to 1500 nm at a fixed angle of incidence of $\Phi_a=65^\circ$. The ellipsometer operates in a rotating compensator configuration and is capable of measuring all 16 normalized, real-valued Mueller matrix elements M_{ij}/M_{11} , which connect the Stokes parameters of the probe beam before and after interaction with the sample [28]. The instrument is equipped with focusing optics and allows accurate ellipsometric data acquisition on a very small sample area with the size of $25 \times 60 \mu\text{m}^2$ at a single angle of incidence. For the ellipsometric measurements, the samples were aligned such that the entire probe beam fitted within the base surface area of the cuboid-shaped samples. This approach simplified the data analysis during which the samples were treated as homogeneous thin films. Two ellipsometric data sets were obtained for each polymer, one data set for each cuboid with a given height. These data sets were analyzed simultaneously. This well known multi-sample analysis approach reduces possible parameter correlation, which might arise from the ellipsometric measurements restricted instrumentally to a single angle of incidence [29].

The experimental and best-model Mueller matrix spectra M_{ij}/M_{11} are shown in Figs. 2.1, 2.2, and 2.3 for IP-Dip, IP-L, and IP-S, respectively. As expected, the observed optical responses of the fabricated samples are isotropic, i.e., only the on-diagonal block Mueller matrix elements are non-trivial and the off-diagonal Mueller matrix elements are negligible [30]. The experimental data were analyzed using stratified-layer optical model calculations employing a commercial ellipsometry data analysis software package (WVASE32TM, J.A. Woollam Co.).

Stratified layer optical models composed of three layers including Si substrate, SiO₂ layer, and a polymer layer are employed for the analysis of the experimental Mueller matrix spectra. The native SiO₂ layer thickness was determined using ellipsometric data obtained from the Si substrate prior to the sample fabrication. The layer thickness of the native SiO₂ was not further varied during the analysis of the ellipsometric data measured for the IP-Dip, IP-L, and IP-S samples. Standard model dielectric functions were used to account for the optical response of the Si substrate and the SiO₂ layer [29].

The parameterized complex dielectric function of the polymers needs to accurately render the optical response of these materials over a wide spectral range from the NIR to the UV. Dielectric function models composed of oscillators with different broadenings have been demonstrated to accurately describe the material dielectric functions throughout the UV, VIS, and IR spectral ranges, while simultaneously ensuring Kramers-Kronig consistency in the determined optical constants [31]. Here, parameterized dielectric functions composed of a combination of oscillators with Gaussian, Lorentz, and Tauc-Lorentz broadenings are used to describe the optical responses of two-photon polymerized IP-Dip, IP-L, and IP-S:

$$\begin{aligned}
\varepsilon(E) &= \varepsilon_1(E) + i\varepsilon_2(E) , \\
&= \varepsilon_\infty + \frac{A}{E_0^2 - E^2} + \sum^l \text{Gau}(A, E_0, \Gamma, E) + \sum^m \text{Lor}(A, E_0, \Gamma, E) \\
&\quad + \sum^n \text{TL}(A, E_0, \Gamma, E_g, E).
\end{aligned} \tag{2.1}$$

The real and imaginary parts of the complex dielectric function $\varepsilon(E)$ are denoted by $\varepsilon_1(E)$ and $\varepsilon_2(E)$, respectively, as functions of the photon energy E . The functions $\text{Gau}(A, E_0, \Gamma, E)$, $\text{Lor}(A, E_0, \Gamma, E)$, and $\text{TL}(A, E_0, \Gamma, E_g, E)$ represent oscillators with Gaussian, Lorentz, and Tauc-Lorentz broadening, respectively, where A is the oscillator amplitude, Γ the oscillator broadening, and E_0 the oscillator energy. For the Tauc-Lorentz oscillator the Tauc gap E_g denotes the energy at which $\varepsilon_2 = 0$. ε_∞ is a constant offset to $\varepsilon_1(E)$. Higher energy contributions to the dielectric function cause absorptions outside of the measured spectral range, which contribute to the dispersion of $\varepsilon_1(E)$. These contributions are included in the model by a pole, i.e., a Lorentz oscillator with vanishing broadening $A/(E_0^2 - E^2)$.

The imaginary part of the dielectric function $\varepsilon_2(E)$ for the oscillators with Gaussian $\varepsilon_2^{\text{Gau}}(E)$, Lorentz $\varepsilon_2^{\text{Lor}}(E)$, and Tauc-Lorentz $\varepsilon_2^{\text{TL}}(E)$ broadening is given by [31, 32, 33]:

$$\varepsilon_2^{\text{Gau}}(E) = Ae^{-\left(\frac{E-E_0}{\Gamma}\right)^2} - Ae^{-\left(\frac{E+E_0}{\Gamma}\right)^2}, \tag{2.2}$$

$$\varepsilon_2^{\text{Lor}}(E) = \frac{AE_0\Gamma}{E_0^2 - E^2 - i\Gamma E}, \tag{2.3}$$

$$\varepsilon_2^{\text{TL}}(E) = \begin{cases} \frac{AE_0\Gamma(E-E_g)^2}{(E^2-E_0^2)^2+\Gamma^2E^2} \cdot \frac{1}{E} & E > E_g \\ 0 & E \leq E_g \end{cases}, \quad (2.4)$$

where the constant $f = 1/2\sqrt{\ln(2)}$ in Eqn. (2.2) defines the full width at half maximum for the broadening Γ . The real part $\varepsilon_1(E)$ is obtained by a Kramers-Kronig integration of $\varepsilon_2(E)$ given in Eqns. (2.2)-(2.4) as part of the data analysis.

During the data analysis of the experimental Mueller matrix data obtained for the IP-Dip, IP-L, and IP-S samples, the relevant model parameters are varied using a Levenberg-Marquardt-based algorithm until the experimental and model calculated data match as close as possible (best-model). The best-model parameters obtained for the oscillator amplitude, energy, and broadening for IP-Dip, IP-L, and IP-S are summarized in Tab. 2.1. The corresponding optical constants are shown in Figs. 2.4, 2.5, and 2.6, respectively.

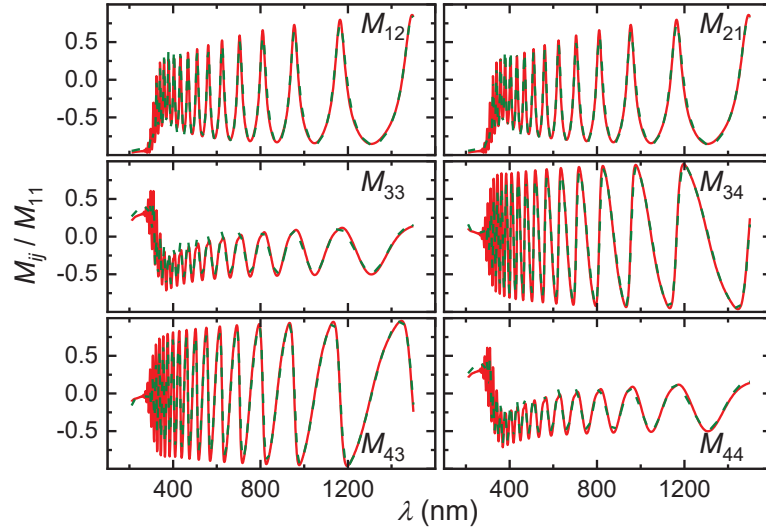


Figure 2.1: Experimental (green dashed lines) and best-model calculated (red solid lines) Mueller matrix spectra of the two-photon polymerized IP-Dip sample with a nominal thickness of 2100 nm for the spectral range from 210 nm to 1500 nm. The angle of incidence was $\Phi_a = 65^\circ$. The data for the sample with a nominal thickness of 3500 nm is omitted here for clarity, but shows also excellent agreement between experimental and best-model calculated line shapes.

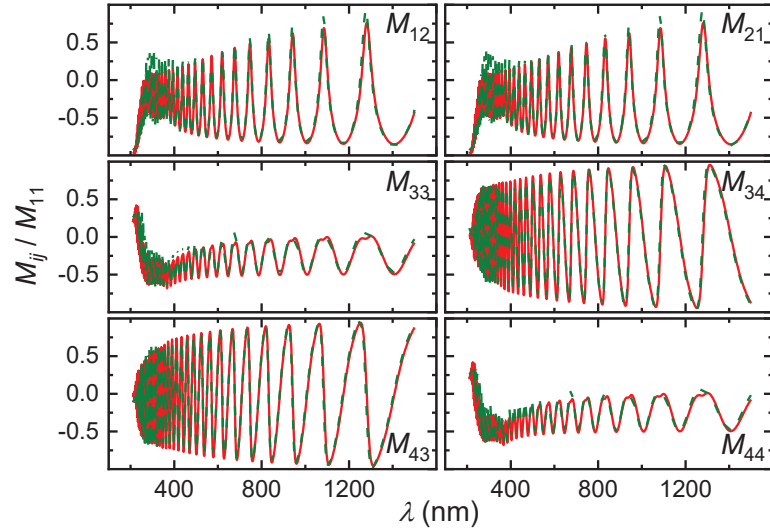


Figure 2.2: Experimental (green dashed lines) and best-model calculated (red solid lines) Mueller matrix spectra of the two-photon polymerized IP-L sample with a nominal thickness of 2900 nm for the spectral range from 210 nm to 1500 nm. The angle of incidence was $\Phi_a = 65^\circ$. The data for the sample with a nominal thickness of 4300 nm is omitted here for clarity, but shows also an excellent agreement between experimental and best-model calculated line shapes.

2.4 Results and discussion

Figures 2.1, 2.2, and 2.3 show experimental (green dashed lines) and best-model calculated (red solid lines) Mueller matrix spectra obtained in the spectral range from 210 nm to 1500 nm for the two-photon polymerized IP-Dip, IP-L, and IP-S samples, with a nominal thickness of 2100 nm, 2900 nm, and 3500 nm, respectively. The angle of incidence was fixed at $\Phi_a = 65^\circ$ for all measurements. Only the non-trivial Mueller matrix elements expected for isotropic sample responses, M_{12} , M_{21} , M_{33} , M_{34} , M_{43} , and M_{44} , are shown for brevity [30].

An excellent agreement between the experimental and best-model calculated data was found for all polymers. Note that for each polymer two samples with different thicknesses were analyzed simultaneously using a common dielectric function. The effects of the angular spread, caused by the used of focusing optics, are included in the model calculation. The best-model values for the angular spread were approximately

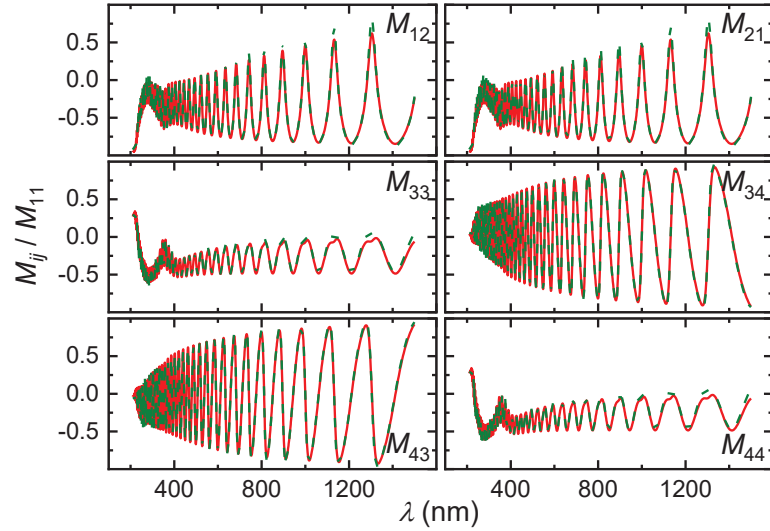


Figure 2.3: Experimental (green dashed lines) and best-model calculated (red solid lines) Mueller matrix spectra of the two-photon polymerized IP-S sample with a nominal thickness of 3500 nm for the spectral range from 210 nm to 1500 nm. The angle of incidence was $\Phi_a = 65^\circ$. As for the IP-Dip and IP-L data shown in Figs. 2.1 and 2.2, respectively, the data for the sample with a nominal thickness of 4500 nm is omitted here for clarity, but shows also an excellent agreement between the experimental and best-model calculated line shapes.

6° , which is typical for the employed ellipsometer equipped with focusing optics.

The Mueller matrix spectra shown in Fig. 2.1 for the IP-Dip sample are dominated by a Fabry-Pérot interference pattern in the spectral range from 400 nm to 1500 nm, which originates from the plane-parallel interfaces of the polymer. As the wavelength approaches the ultraviolet region below 400 nm, a significant dampening of the interference amplitude can be recognized. This indicates the presence of substantial absorption bands in the spectral range from 210 nm to 400 nm.

A similar optical response can be observed in the Mueller matrix spectra of IP-L and IP-S depicted in Fig. 2.2 and 2.3, respectively. However, the positions and amplitudes of the absorption bands are different among the three investigated polymers.

Table 2.1 summarizes the the best-model fit parameters for the mixed oscillator model dielectric functions of IP-Dip, IP-L, and IP-S, respectively. Accurate rendering of the experimental Mueller matrix data of IP-Dip requires a combination of two

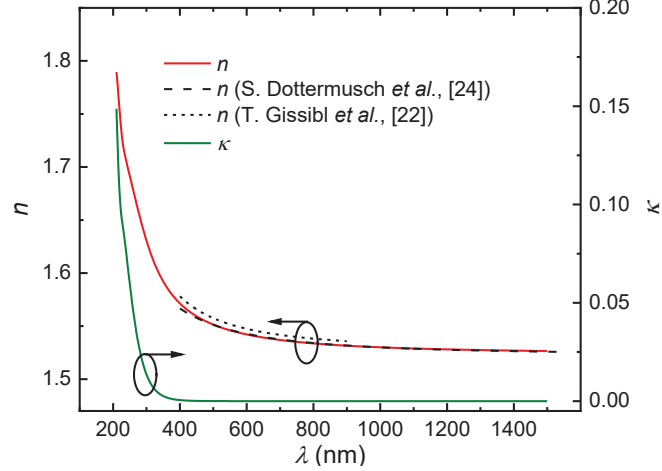


Figure 2.4: The best-fit model refractive index n (red solid line) and extinction coefficient κ (green dashed line) for two-photon polymerized IP-Dip in the spectral range from 210 nm to 1500 nm. The spectrum below 400 nm is dominated by absorption bands, which are described by two oscillators with Tauc-Lorentz and Gaussian broadening. The best-model parameters are summarized in Tab. 2.1. The refractive index of two-photon polymerized (black dashed line) and single-photon polymerized (black dotted line) IP-Dip reported by S. Dottermusch *et al.* and T. Gissibl *et al.*, respectively, are reproduced for comparison [22, 24].

oscillators including an oscillator with Tauc-Lorentz and one with Gaussian broadening. In the model dielectric function of IP-L two Lorentz oscillators and one pole were used. For the model dielectric function of IP-S, three oscillators including one pole with two broadening types (Gaussian and Lorentz) were required. The best-fit values for the static dielectric constants ε_∞ of the investigated polymers were comparable. The largest value was found for IP-S with $\varepsilon_\infty = 1.46 \pm 0.01$. The values for IP-Dip and IP-L are slightly smaller with $\varepsilon_\infty = 1.43 \pm 0.04$ for IP-Dip and $\varepsilon_\infty = 1.44 \pm 0.01$ for IP-L. The best-model parameters for the thicknesses of the polymer samples are $t_{\text{IP-Dip}} = 2124 \pm 4$ nm, $t_{\text{IP-L}} = 2940 \pm 1$ nm and $t_{\text{IP-S}} = 3582 \pm 4$ nm, which are in good agreement with the nominal values as expected from the 3D-DLW fabrication.

Figures 2.4, 2.5, and 2.6 depict the refractive index n (red solid lines) and extinction coefficient κ (green solid lines) of the best-fit model for IP-Dip, IP-L, and IP-S in the spectral range from 210 nm to 1500 nm, respectively. The refractive index data reported by S. Dottermusch *et al.* for two-photon polymerized (black dashed line)

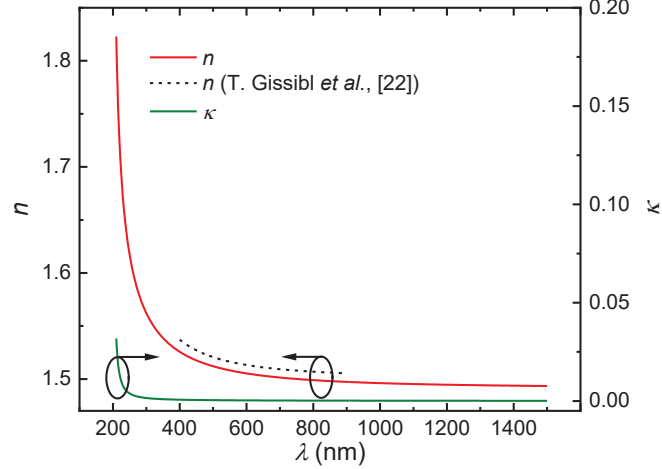


Figure 2.5: Same as Fig. 2.4 but for IP-L. IP-L is characterized by a sharp absorption onset which can be described by a single Lorentz oscillator. The best-model parameters are summarized in Tab. 2.1. The refractive index of single-photon polymerized IP-L (black dotted line) reported by T. Gissibl *et al.* is shown for comparison [22].

Table 2.1: **All Polymers best-model oscillator parameters, with errors representing the 90% confidence limits of the model parameters.**

	Oscillator	A	E_0 (eV)	Γ (eV)	E_g (eV)
IP-Dip	TL	(135.87 ± 4.18) eV	6.34 ± 0.05	3.95 ± 0.70	5.48 ± 0.01
	Gau	0.69 ± 0.13	5.84 ± 0.13	1.98 ± 0.08	—
IP-L	Pole	(70.84 ± 0.68) eV ²	10.43 ± 0.02	—	—
	Lor	0.83 ± 0.03	6.37 ± 0.02	0.12 ± 0.01	—
IP-S	Pole	(65.81 ± 0.50) eV ²	9.82 ± 0.01	—	—
	Lor	1.72 ± 0.09	6.24 ± 0.02	0.17 ± 0.01	—
	Gau	0.01 ± 0.001	3.47 ± 0.01	0.53 ± 0.01	—

IP-Dip [24] and by T. Gissibl *et al.* for single photon polymerized IP-Dip, IP-L, and IP-S (black dotted lines) [22] are included in Figs. 2.4-2.6 for comparison.

An excellent agreement of the refractive index determined using a mixed oscillator model dielectric function here and the refractive index reported in Refs. [24] can be observed for two-photon polymerized IP-Dip (Fig. 2.4) in the spectral region where the polymer is transparent. As expected, a small difference can be noticed between the refractive index of single-photon polymerized (UV cured) polymers and the corresponding two-photon polymerized IP-Dip, IP-L, and IP-S [22]. For all three

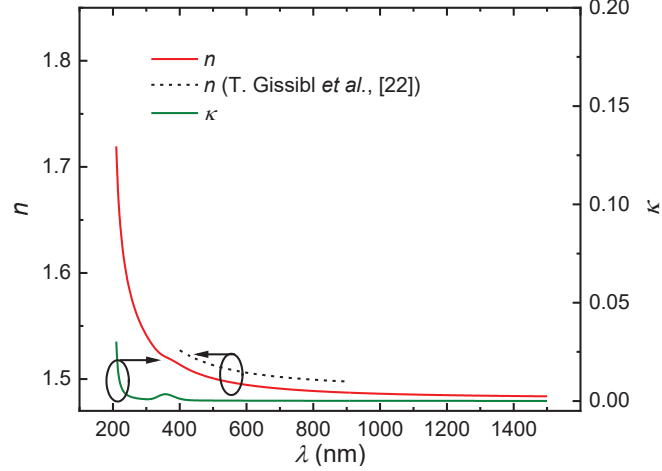


Figure 2.6: Same as Fig. 2.4 but for IP-S, which can be described using two oscillators with Lorentz and Gaussian broadening. The best-model parameters are summarized in Tab. 2.1. In addition to the sharp absorption onset below 300 nm, a small absorption band at 358 nm can be observed. The refractive index of single-photon, UV-cured IP-S (black dotted line) reported by T. Gissibl *et al.* is shown for comparison [22].

investigated polymers, the refractive index of the single-photon polymerized sample is higher than the refractive index of the two-photon polymerized sample. Therefore, optical elements that rely on a small index difference of adjacent polymer layers, like the waveguides suggested by Dottermusch *et al.*, could be realized using all of the investigated polymers [24].

To provide a direct comparison of the optical properties for the investigated polymers, the determined refractive indices n and extinction coefficients κ have been presented together in Fig. 2.7. Comparing the refractive indices n shown in panel (a) of Fig. 2.7, one can easily verify that the two-photon polymerized IP-Dip has the highest refractive index among the investigated polymers in the VIS spectral range. The refractive indices of IP-L and IP-S are grouped closely together and are substantially smaller compared to the refractive index of IP-Dip. The wider transparent window of IP-L and IP-S compared to IP-Dip can be immediately observed in Fig. 2.7 (b).

Common for all polymers is also the strong absorption in the UV spectral range.

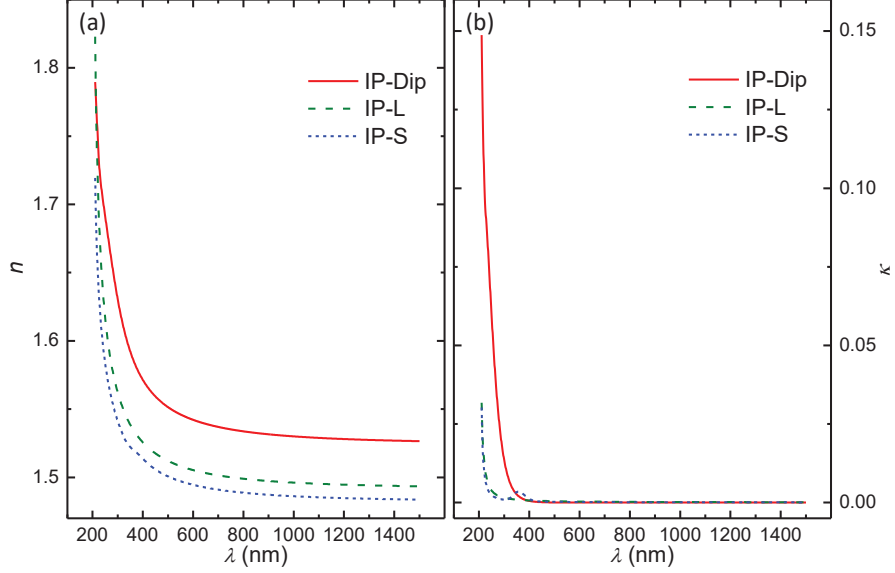


Figure 2.7: The best-fit model refractive indices n and extinction coefficients κ for the two-photon polymerized IP-Dip, IP-L, and IP-S are reproduced in panel (a) and (b), respectively, for a direct comparison.

However, while IP-Dip is transparent up to 350 nm, the absorption onset for IP-S and IP-L occurs further into the UV spectral range. Both IP-L and IP-S exhibit strong absorption bands at 210 nm, suggesting a much wider usable transparent window as compared to IP-Dip. In contrast to IP-Dip, the absorption onset for IP-S and IP-L is very abrupt. IP-Dip exhibits a very broad absorption onset and in addition a noticeable absorption band at approximately 230 nm. Only for IP-S a small absorption band is found inside the transparent window at approximately 358 nm. However, this band is relatively weak and may not impair the transmission of thin optical components.

2.5 Conclusion

The complex dielectric functions of two-photon polymerized IP-Dip, IP-L, and IP-S have been accurately determined using Mueller matrix spectroscopic ellipsometry in the range from 210 nm to 1500 nm. Parameterized dielectric function models composed of oscillators with mixed broadening including Gaussian, Lorentz, and Tauc-

Lorentz broadened line shapes are used to accurately represent the optical response of the investigated polymers. In addition to enabling convenient numerical access to the complex dielectric responses of the investigated polymers, the use of parameterized dielectric functions reported here prevents instrument noise from becoming part of the established optical properties. This is a significant advantage compared to so-called point-by-point extraction techniques. The use of oscillators with mixed broadenings further enables the description of spectral ranges with measurable absorption. A good agreement of the refractive index in the transparent region is found between the results obtained here compared with literature values reported for two-photon polymerized IP-Dip in the spectral range from 400 nm to 1500 nm [24].

As expected, all investigated polymers show strong absorption bands in the UV spectral region, however, substantial differences are observed among the individual investigated polymers. While IP-Dip starts to absorb at approximately 308 nm, the transparent window of IP-L and IP-S extends to approximately 230 nm in the UV spectral range if a small absorption peak observed in IP-S at approximately 358 nm is neglected in this comparison. The location, strength, and broadening of the observed absorption bands in the UV spectral region are reported here. Comparing the refractive index of the polymers in the transparent window from 400 to 1500 nm, it can be observed that IP-S has the lowest index while IP-Dip has the highest one. Taking refractive index at wavelength of 1500 nm as an example, the values for index n are 1.526 ± 0.008 , 1.492 ± 0.007 , and 1.483 ± 0.003 for IP-Dip, IP-L, and IP-S, respectively. In addition to providing accurate complex refractive index data, the difference between the refractive index observed for single- and two-photon polymerized IP-Dip is confirmed [24]. As suggested by S. Dottermusch *et al.* this index difference could be utilized to fabricate waveguides where the core is synthesized by single-photon polymerization while the cladding is cured using two-photon polymerization [24]. A similar refractive index difference is found for single- and two-photon polymerized

IP-L and IP-S, wherein the refractive indices of the single-photon polymerized materials are reported by T. Gissibl *et al.* [22]. Therefore, optical element designs that rely on the refractive index differences of adjacent polymers could also utilize IP-L and IP-S, substantially extending the accessible range of critical dimensions for such approaches.

Our parameterized model dielectric functions for three of the most widely used polymers, which are compatible with three dimensional direct laser writing using two-photon polymerization, now provide accurate complex refractive index values for the ultraviolet to the near-infrared spectral range. Access to accurate complex refractive index data is crucial for the design and development of optical materials and components fabricated using two-photon polymerization which is receiving substantial research interest. While the results reported here are restricted to three polymers compatible with the used two-photon polymerization system, the developed mixed oscillator dielectric function model is expected to provide a flexible analysis approach, which could be also applied to other photopolymers compatible with two-photon polymerization.

REFERENCES

- [1] M. Deubel, G. Von Freymann, M. Wegener, S. Pereira, K. Busch, and C. M. Soukoulis, “Direct laser writing of three-dimensional photonic-crystal templates for telecommunications,” *Nat. Mater.* **3**, 444 (2004).
- [2] M. Deubel, M. Wegener, A. Kaso, and S. John, “Direct laser writing and characterization of “slanted pore” photonic crystals,” *Appl. Phys. Lett.* **85**, 1895 (2004).
- [3] M. Nawrot, Ł. Zinkiewicz, B. Włodarczyk, and P. Wasylczyk, “Transmission phase gratings fabricated with direct laser writing as color filters in the visible,” *Opt. Express* **21**, 31919 (2013).
- [4] P.-I. Dietrich, M. Blaicher, I. Reuter, M. Billah, T. Hoose, A. Hofmann, C. Caer, R. Dangel, B. Offrein, U. Troppenz, *et al.*, “In situ 3D nanoprinting of free-form coupling elements for hybrid photonic integration,” *Nat. Photonics* **12**, 241 (2018).
- [5] A. E. Goodling, S. Nagelberg, B. Kaehr, C. H. Meredith, S. I. Cheon, A. P. Saunders, M. Kolle, and L. D. Zarzar, “Colouration by total internal reflection and interference at microscale concave interfaces,” *Nature* **566**, 523 (2019).
- [6] Y. Li, H. Zhao, S.-F. Feng, J.-S. Ye, X.-K. Wang, W.-F. Sun, P. Han, and Y. Zhang, “New design model for high efficiency cylindrical diffractive microlenses,” *Sci. Rep.* **7**, 16334 (2017).
- [7] T. P. Xiao, O. S. Cifci, S. Bhargava, H. Chen, T. Gissibl, W. Zhou, H. Giessen, K. C. Toussaint Jr, E. Yablonovitch, and P. V. Braun, “Diffractive spectral-splitting optical element designed by adjoint-based electromagnetic optimization

- and fabricated by femtosecond 3D direct laser writing,” *ACS Photonics* **3**, 886 (2016).
- [8] Ł. Zinkiewicz, J. Haberko, and P. Wasylczyk, “Highly asymmetric near infrared light transmission in an all-dielectric grating-on-mirror photonic structure,” *Opt. Express* **23**, 4206 (2015).
- [9] I. Sakellari, X. Yin, M. L. Nesterov, K. Terzaki, A. Xomalis, and M. Farsari, “3D chiral plasmonic metamaterials fabricated by direct laser writing: The twisted omega particle,” *Adv. Opt. Mater.* **5**, 1700200 (2017).
- [10] J. Moughames, S. Jradi, T. Chan, S. Akil, Y. Battie, A. E. Naciri, Z. Herro, S. Guenneau, S. Enoch, L. Joly, *et al.*, “Wavelength-scale light concentrator made by direct 3D laser writing of polymer metamaterials,” *Sci. Rep.* **6**, 33627 (2016).
- [11] V. Caligiuri, R. Dhama, K. Sreekanth, G. Strangi, and A. De Luca, “Dielectric singularity in hyperbolic metamaterials: the inversion point of coexisting anisotropies,” *Sci. Rep.* **6**, 20002 (2016).
- [12] B. Wang, Z. Xie, S. Feng, B. Zhang, and Y. Zhang, “Ultra-high Q-factor and figure of merit fano metamaterial based on dark ring magnetic mode,” *Opt. Commun.* **335**, 60 (2015).
- [13] T. Gissibl, S. Thiele, A. Herkommer, and H. Giessen, “Two-photon direct laser writing of ultracompact multi-lens objectives,” *Nat. Photonics* **10**, 554 (2016).
- [14] M. Schmid, S. Thiele, A. Herkommer, and H. Giessen, “Three-dimensional direct laser written achromatic axicons and multi-component microlenses,” *Opt. Lett.* **43**, 5837 (2018).
- [15] Y. Li, H. Zhao, S.-F. Feng, J.-S. Ye, X.-K. Wang, W.-F. Sun, P. Han, and

- Y. Zhang, “New design model for high efficiency cylindrical diffractive microlenses,” *Sci. Rep.* **7**, 16334 (2017).
- [16] Y. Li, D. Fullager, S. Park, D. Childers, R. Fesperman, G. Boreman, and T. Hofmann, “High-contrast infrared polymer photonic crystals fabricated by direct laser writing,” *Opt. Lett.* **43**, 4711 (2018).
- [17] C. Marichy, N. Muller, L. S. Froufe-Pérez, and F. Scheffold, “High-quality photonic crystals with a nearly complete band gap obtained by direct inversion of woodpile templates with titanium dioxide,” *Sci. Rep.* **6**, 21818 (2016).
- [18] M. Kowalczyk, J. Haberko, and P. Wasylczyk, “Microstructured gradient-index antireflective coating fabricated on a fiber tip with direct laser writing,” *Opt. Express* **22**, 12545 (2014).
- [19] Y. Li, D. Fullager, E. Angelbello, D. Childers, G. Boreman, and T. Hofmann, “Broadband near-infrared antireflection coatings fabricated by three-dimensional direct laser writing,” *Opt. Lett.* **43**, 239 (2018).
- [20] X. Xiong, S.-C. Jiang, Y.-H. Hu, R.-W. Peng, and M. Wang, “Structured metal film as a perfect absorber,” *Adv. Mater.* **25**, 3994 (2013).
- [21] B. Jose, R. K. Vijayaraghavan, L. Kent, S. O’Toole, J. O’Leary, and R. J. Forster, “Tunable metallic nanostructures using 3D printed nanosphere templates,” *Electrochem. Commun.* **98**, 106 (2019).
- [22] T. Gissibl, S. Wagner, J. Sykora, M. Schmid, and H. Giessen, “Refractive index measurements of photo-resists for three-dimensional direct laser writing,” *Opt. Mater. Express* **7**, 2293 (2017).
- [23] D. B. Fullager, G. D. Boreman, and T. Hofmann, “Infrared dielectric response

- of Nanoscribe IP-Dip and IP-l monomers after polymerization from 250 cm^{-1} to 6000 cm^{-1} ,” *Opt. Mater. Express* **7**, 888 (2017).
- [24] S. Dottermusch, D. Busko, M. Langenhorst, U. W. Paetzold, and B. S. Richards, “Exposure-dependent refractive index of nanoscribe IP-Dip photoresist layers,” *Opt. Lett.* **44**, 29 (2019).
- [25] I. Faniayeu and V. Mizeikis, “Realization of a helix-based perfect absorber for ir spectral range using the direct laser write technique,” *Opt. Mater. Express* **7**, 1453 (2017).
- [26] X. Xiong, Z.-H. Xue, C. Meng, S.-C. Jiang, Y.-H. Hu, R.-W. Peng, and M. Wang, “Polarization-dependent perfect absorbers/reflectors based on a three-dimensional metamaterial,” *Phys. Rev. B* **88**, 115105 (2013).
- [27] J. S. Oakdale, R. F. Smith, J.-B. Forien, W. L. Smith, S. J. Ali, L. B. Bayu Aji, T. M. Willey, J. Ye, A. W. van Buuren, M. A. Worthington, *et al.*, “Direct laser writing of low-density interdigitated foams for plasma drive shaping,” *Adv. Funct. Mater.* **27**, 1702425 (2017).
- [28] H. Fujiwara, *Spectroscopic Ellipsometry Principles and Applications*, (John Wiley & Sons Inc., Hoboken, NJ 07030, USA, 2007).
- [29] C. Herzinger, B. Johs, W. McGahan, J. A. Woollam, and W. Paulson, “Ellipsometric determination of optical constants for silicon and thermally grown silicon dioxide via a multi-sample, multi-wavelength, multi-angle investigation,” *J. Appl. Phys.* **83**, 3323 (1998).
- [30] *The measured experimental values for all off-diagonal Mueller matrix elements are $0\pm/-.0.01$, as would be expected for an isotropic sample response. Therefore, only the non-trivial on-diagonal Mueller matrix elements are reported here for brevity .*

- [31] R. Synowicki and T. E. Tiwald, "Optical properties of bulk c-ZrO₂, c-MgO and a-As₂S₃ determined by variable angle spectroscopic ellipsometry," *Thin Solid Films* **455**, 248 (2004).
- [32] G. Jellison Jr and F. Modine, "Parameterization of the optical functions of amorphous materials in the interband region," *Appl. Phys. Lett.* **69**, 371 (1996).
- [33] J. G. E. Jellison and F. A. Modine, "Erratum: "Parameterization of the optical functions of amorphous materials in the interband region" [*Appl. Phys. Lett.* **69**, 371 (1996)]," *Appl. Phys. Lett.* **69**, 2137 (1996).

CHAPTER 3: BROADBAND NEAR-INFRARED ANTIREFLECTION
COATINGS FABRICATED BY THREE DIMENSIONAL DIRECT LASER
WRITING¹

3.1 Abstract

Three-dimensional direct laser writing via two photon polymerization is used to fabricate anti-reflective structured surfaces composed of sub-wavelength conicoid features optimized to operate over a wide bandwidth in the near-infrared range from 3700 cm^{-1} to 6600 cm^{-1} (2.7 to $1.52\text{ }\mu\text{m}$). Analytic Bruggemann effective medium calculations are used to predict nominal geometric parameters such as the fill factor of the constitutive conicoid features of the anti-reflective structured surfaces presented here. The performance of the anti-reflective structured surfaces were investigated experimentally using infrared transmission measurements. An enhancement of the transmittance by 1.35% to 2.14% over a broadband spectral range from 3700 cm^{-1} to 6600 cm^{-1} (2.7 to $1.52\text{ }\mu\text{m}$) was achieved. We further report on finite-element-based results using three-dimensional model geometries for comparison. We find a good agreement between experimental results and the finite-element-based numerical analysis once as-fabricated deviations from the nominal conicoid forms are included in the model. Three-dimensional direct laser writing is demonstrated here as an efficient method for the fabrication and optimization of anti-reflective structured surfaces designed for the infrared spectral range.

¹Y. Li, T. Hofmann, *et al.*, *Opt. Lett.* **43**, 239 (2018). Reprinted with permission © The Optical Society.

3.2 Introduction

Since the discovery by C.G. Bernhard in 1967, biomimetic anti-reflective structured surfaces (ARSS) have enjoyed continued interest by the research community [1]. Compared to conventional thin-film anti-reflective coatings, ARSS have some inherent advantages such as the ability to tailor arbitrary index profiles[2], to enable frequency-independent Fresnel reflection reduction [3], or to require only a single material in the fabrication [4], for instance. Theoretically, sub-wavelength features can be designed to completely eliminate Fresnel loss by inducing forward scattering of otherwise evanescent diffraction orders [5].

As early as 1973, the functionality of ARSS was established in the visible spectral range [6]. Using photo-polymerized subwavelength-sized structures fabricated by interference lithography Clapham and Hutley achieved a reduction of the reflectance to less than 0.2% under normal incidence in the spectral range from 400 nm to 700 nm [6]. In general, complex fabrication techniques have been required for the synthesis of the subwavelength-sized structures which constitute the ARSS and have thereby limited the widespread use of the ARSS approach [7, 8, 9, 10, 11, 12].

Some renewed interest in ARSS is due to advances in nano- and micro-structure fabrication techniques which have led to numerous recent investigations devoted to maximize the transmissivity of ARSS by optimizing the geometry of the ARSS constituent features [13, 14, 15, 16, 17].

Recently, Kowalczyk *et al.* demonstrated for the first time that 3-dimensional direct laser writing (3D-DLW) via two-photon polymerization can be used for the fabrication of the subwavelength-sized structures for ARSS in the near-infrared spectral range [4]. This new approach circumvents the restrictions of previously employed lithographic techniques which are only allowed for a limited and very time-consuming exploration of the geometric parameter space of the subwavelength-sized structures. 3D-DLW now allows the fabrication of virtually arbitrary 3D structures with nm-sized features [18].

As such, 3D-DLW is ideally suited for the fabrication of ARSS and thereby enables optimization of the subwavelength-sized structure geometries required for ARSS in the infrared spectral range [19, 20].

Here we demonstrate the usefulness of 3D-DLW for the fabrication of 3D subwavelength-sized structures for ARSS and explore the geometric parameter space of these structures. Our observations show that 3D-DLW allows for rapid fabrication and cost-effective optimization of ARSS designed for the infrared spectral range when compared to previously demonstrated methods.

Although it is well known that the performance of a given ARSS depends critically on the geometric parameters of the constitutive features, such as shape, density, height and arrangement, suitable avenues to optimize ARSS performance, however, have not been reported. Even though several studies have been carried out to numerically optimize the geometrical parameters [16], only a few results have been experimentally validated. For the near-infrared spectral range, where sub-micron spatial resolution provides sufficient capability to design ARSS, 3D-DLW offers an efficient path for rapid prototyping. Although ARSS performance has been observed over a narrow spectral range centered at 1550 nm, anti-reflection behavior over a broadband spectral range in the near-infrared has not been reported [4].

In this letter, we report on a simple 3D-DLW-based rapid prototyping approach for designing and fabricating conicoid constituent ARSS on transparent substrates to achieve optimal anti-reflective performance over broadband near-infrared range. Using the Bruggemann effective medium homogenization, we explore the transmission enhancement associated with the variation of the fill factor f , defined as the ratio of the cone base diameter D to the lateral separation (pitch) P . We find by both experimental FTIR transmission measurements and three-dimensional finite-element method (3D-FEM) calculations using COMSOL (RF-module) that a maximum increase in transmission of 2.14% over a spectral range from 3700 cm^{-1} to 6600 cm^{-1}

can be achieved for $f = 0.8$ for the conicoid structures fabricated here. Scanning electron microscopy (SEM) was performed to evaluate the resulting 3D-DLW geometry of the ARSS constituent features and inform the 3D-FEM calculations.

3.3 Theory and experiment

The ARSS constituents are conicoid sub-wavelength structures symmetrically arranged in a hexagonal lattice pattern. Due to the spatially symmetrical distribution, the Bruggemann effective medium homogenization is suitable to estimate the gradual index transition throughout the ARSS domain [21]. The Bruggemann effective medium model for the permittivity of the ARSS $\varepsilon_{\text{ARSS}}$ accounts for the relative volume fraction of the sub-wavelength structures [22]:

$$\varepsilon_{\text{ARSS}}(f_i) = \frac{1}{4} \left\{ (3f_i - 1)\varepsilon_i + (2 - 3f_i)\varepsilon_h \pm \sqrt{[(3f_i - 1)\varepsilon_i + (2 - 3f_i)\varepsilon_h]^2 + 8\varepsilon_i\varepsilon_h} \right\}, \quad (3.1)$$

where $f_i(f, z)$ is the volume fraction of conicoid subwavelength inclusions $f_i(f, z) = \frac{\pi f^2(1-z)^2}{2\sqrt{3}}$, and z corresponds to the distance from the top of the ARSS to the substrate. The permittivities of the inclusions (IP-dip) and the host (air) are denoted by ε_i and ε_h , respectively.

Figure 3.1 depicts $\varepsilon_{\text{ARSS}}$ at $\omega = 5000 \text{ cm}^{-1}$ as a function of the distance to the air/ARSS interface z for $f = 0.6, 0.7, 0.8,$ and 0.9 . Upon inspection, the smoothest transition of $\varepsilon_{\text{ARSS}}$ from ε_h (air) to the permittivity of the substrate (glass) is found for $f = 0.9$. In contrast, the values of $\varepsilon_{\text{ARSS}}$ for $f = 0.6, 0.7,$ and 0.8 show a stronger permittivity contrast at the ARSS/substrate interface ($z=1 \mu\text{m}$). For the purposes of the plotted analytic function in Fig. 3.1 the domain of the ARSS has been sliced into 100 equally thick sub-layers. The permittivity values for the glass substrate and IP-dip were acquired through variable angle spectroscopic ellipsometry measurements [23]. The cubic profile of the index transition results from the conical shape of the ARSS

constituents.

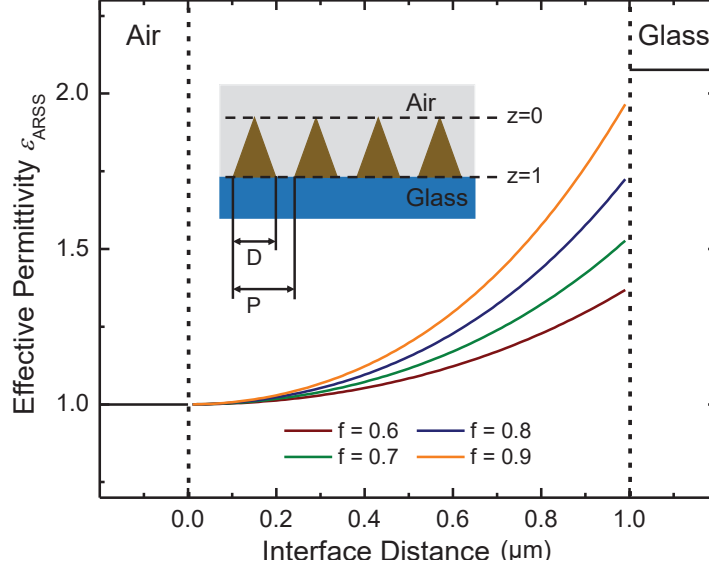


Figure 3.1: Plot of the real part of the effective permittivity $\varepsilon_{\text{ARSS}}$ as a function of the distance in micrometers from the top of the ARSS relative to the substrate, z , from air ($z = 0 \mu\text{m}$) to the substrate ($z = 1 \mu\text{m}$) across the ARSS ($0 \mu\text{m} < z < 1 \mu\text{m}$) based on a Bruggemann effective medium homogenization. The effective permittivity at 5000 cm^{-1} for cone-like ARSS with $f = 0.6, 0.7, 0.8,$ and 0.9 are shown as brown, green, blue, and orange solid lines, respectively. The effective permittivity of air and glass substrate are shown as black solid lines in each corresponding sections. The insert shows the layout of the three individual sections: air, ARSS, and glass substrate.

Four ARSS structures composed of conicoid constituents were fabricated by polymerizing IP-dip monomer on glass substrates using a commercially available 3D-DLW system (Photonic Professional GT, Nanoscribe, GmbH). The nominal height of the ARSS is $1 \mu\text{m}$, with the constituent features arranged in hexagonally ordered $50 \mu\text{m} \times 50 \mu\text{m}$ arrays. The nominal fill factor f is varied from 0.6 to 0.9 in steps of 0.1. The ARSS were fabricated in a single 3D-DLW fabrication step using an optimized exposure dose determined prior to the sample synthesis. After fabrication, the unpolymerized monomer is removed by immersion in PGMEA (Baker 220), and subsequently in 99.99% isopropyl alcohol for 20 min and 2 min, respectively. Lastly, the remaining isopropyl alcohol is evaporated by blow-drying with dry nitrogen. The

samples were post-cured in an ultraviolet oven for ten minutes to ensure complete polymerization of the structures.

3D-FEM calculations were performed for comparison with measured FTIR reflection and transmission data as well as qualitative comparison with the aforementioned homogenized Bruggemann calculations. Representative images depicting the array of nominal conicoid ARSS employed in the 3D-FEM calculations are shown in Fig. 3.2. Note that, single unit cells utilizing Floquet (periodic) boundary conditions were used for the 3D-FEM calculations of the ARSS reflectance and transmittance. In addition to the nominal conical geometries, conicoids which more closely resemble the SEM images (see Fig. 3.3) were also employed (see Fig. 3.4) as geometrical parameters for the 3D-FEM calculations (Fig.3.5 b), dashed dotted lines). The dielectric functions of the glass substrate and IP-dip were determined using variable angle IR ellipsometry and are reported elsewhere [23]. An incident angle of 17° was used in the numerical finite-element model calculations corresponding to the angular incidence average of the Cassegrain objective used in the infrared microscope [24].

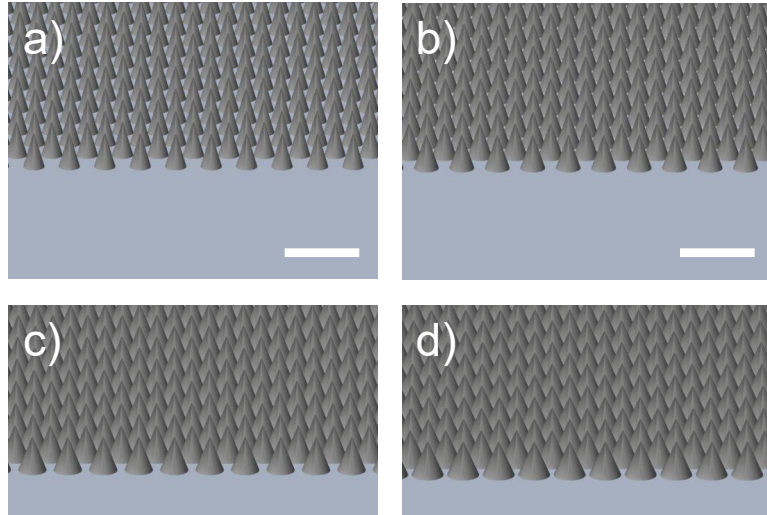


Figure 3.2: Nominal design for 3D arrays of the conicoid ARSS with a height of $1 \mu\text{m}$ and $f = 0.6, 0.7, 0.8,$ and 0.9 shown in panels a), b), c), and d), respectively. Scale bars indicate $2 \mu\text{m}$.

Figure 3.3 shows SEM micrographs of the fabricated samples, where panels a), b),

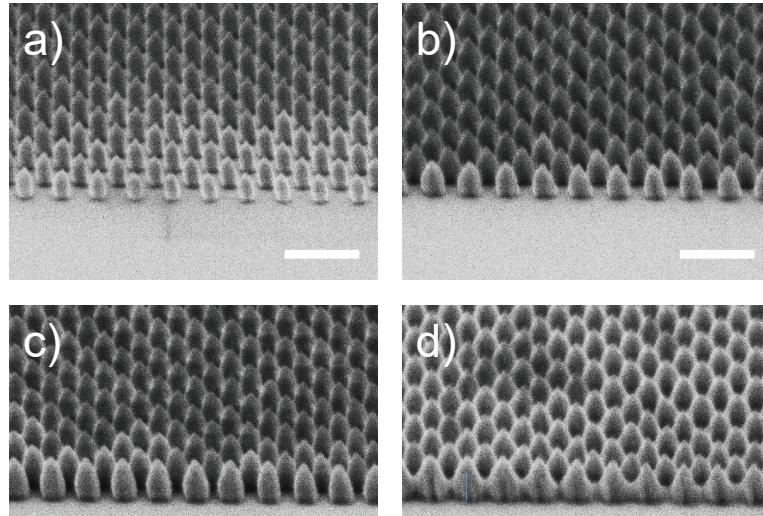


Figure 3.3: SEM micrographs of the conocoid ARSS with a nominal height of $1 \mu\text{m}$ and $f = 0.6, 0.7, 0.8,$ and 0.9 are shown in panels a), b), c), and d), respectively. Note that a SEM micrograph was obtained with the sample tilted by 35° from normal. Scale bars indicate $2 \mu\text{m}$.

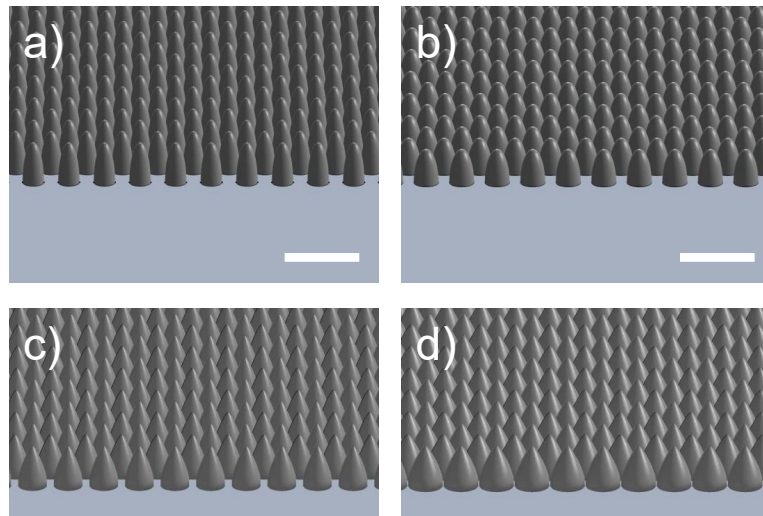


Figure 3.4: 3D arrays of the conocoid ARSS with corrected geometries representative of the as-printed structures for post-comparison with $f = 0.6, 0.7, 0.8,$ and 0.9 shown in panels a), b), c), and d), respectively. Scale bars indicate $2 \mu\text{m}$.

c), and d) depict the micrographs of the samples with a nominal fill factor f of $0.6, 0.7, 0.8$ and 0.9 , respectively. A good agreement between the nominal, as-designed shape and the resulting outcome of the 3D-DLW process is observed for f of $0.6, 0.7,$ and 0.8 . As a result of process variability, the $f = 0.9$ demonstrates slight deviation

from the intended spatial density.

Reflection and transmission infrared microscopy measurements were carried out in the spectral range from 3700 cm^{-1} to 6600 cm^{-1} with a resolution of 4 cm^{-1} using a Fourier transform infrared (FTIR) spectrometer in conjunction with an infrared microscope (VERTEX 70 and HYPERION 3000, Bruker, Inc.) and are shown in Figures 3.5 and 3.6, respectively. A $15\times$ Cassegrain objective is used for the reflection measurements whereas the transmission measurements used a complementary $15\times$ Cassegrain condenser. The Cassegrain illumination configuration results in a range of angles of incidence from 10.8° to 23.5° defined by the numerical aperture of the Cassegrain objectives and the diameter of their central mirrors [24]. The samples were mounted such that the ARSS faced the objective as opposed to the condenser.

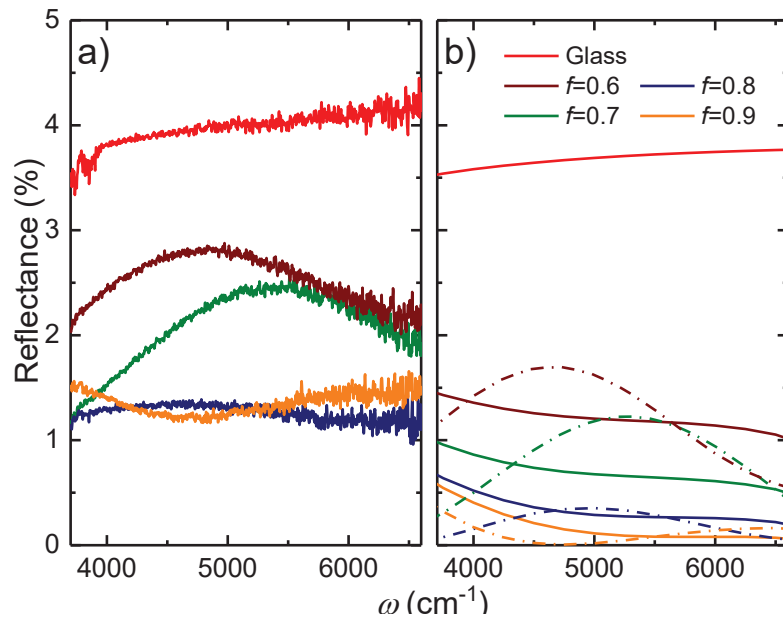


Figure 3.5: Experimental (a) and 3D-FEM calculated (b) reflectance spectra for $f = 0.6$ (brown), 0.7 (green), 0.8 (blue), and 0.9 (orange). The solid lines represent the calculated data using the nominal conical geometry, whereas the dash dotted lines indicate the approximated as-printed (see Figs. 3.3 and 3.4) more sharply tapered geometries which were re-iterated in COMSOL.

Figure 3.5 shows the comparison of the experimental a) and 3D-FEM model calculated b) reflectance spectra of samples with $f = 0.6$ (brown), $f = 0.7$ (green), $f = 0.8$

(blue) and $f = 0.9$ (orange), respectively. The reflectance spectrum of the bare substrate (red solid line) is shown for comparison. The solid and dash dot lines in panel b) represent the calculated reflectance for nominal and as-printed geometries, respectively (see Figs. 3.2 and 3.4). In general, the experimental and 3D-FEM model data are in a good agreement. For all ARSS samples, we observe lower reflectance than for the bare glass substrate. Moreover, with increasing fill factor f , the ARSS efficiency increases, corresponding to the trend seen in the 3D model calculation. Deviations between the experimental and 3D-FEM model calculated line shapes are attributed to the difference between nominal and as-printed geometries. The corrected 3D-FEM model calculations were reiterated using geometries which more closely resemble the as-printed geometry as observed in the SEM micrographs shown in Fig. 3.3. These results are shown using dash dot lines and, in general, show a closer resemblance to the experimental lineshapes. The discrepancy between the experimental and calculated reflectance on average varies by approximately 1%.

Figure 3.6 shows the comparison of normalized transmittance between the experimental data a) and 3D-FEM model calculation b). The transmission data were normalized to the bare glass substrate. The solid (nominal geometries, see Fig. 3.2) and dash dot lines (as-printed geometries, see Fig. 3.4) follow the same trend as a function of f as the reflectance in Fig. 3.5. The bowing behavior observed in the experimental data for $f = 0.6$ and 0.7 is well represented in the 3D-FEM calculations using the as-printed geometries. It is worth noting that the transmittance of the sample with $f = 0.9$ has the lowest value which is in contrast to the reflectance spectra in Fig. 3.5. We attribute this behavior to the structural deviation from the nominal geometry which is most apparent for $f = 0.9$ (see Fig. 3.3).

3.4 Conclusion

In conclusion, we observe that the Bruggemann homogenization detailed herein provides a good analytic prediction of ARSS performance. All the ARSS shown

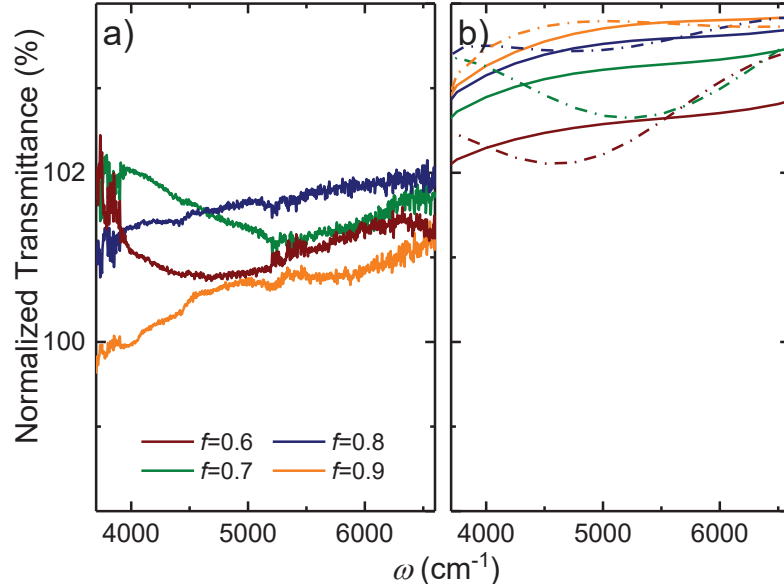


Figure 3.6: Same as Fig. 3.5 for the experimental and 3D-FEM calculated transmittance data depicted in panels a) and b) respectively. Note that the transmission data were normalized to the bare glass substrate.

herein exhibit higher transmittance and lower reflectance while being applied to only a single surface than for the bare substrate alone. Variations in the functionality of the ARSS relative to the 3D-FEM data were investigated through re-simulation utilizing geometrical parameters determined by inspection of SEM micrographs of the ARSS samples. The results obtained in these corrected 3D-FEM calculations showed a better agreement with the experimental reflectance and transmittance data in the cases where there was an apparent discrepancy between the nominal and as-printed conicoids seen in Fig. 3.3. Thus, we have demonstrated functional ARSS geometries fabricated using 3D-DLW which operate over a broad bandwidth in the near-infrared spectral range and exhibit negligible absorption. 3D-DLW therefore provides a new avenue for the fabrication and efficient optimization of ARSS for the near-infrared spectral range and might allow for a comprehensive exploration of the parameter space of the ARSS.

REFERENCES

- [1] C. Bernhard, "Structural and functional adaptation in a visual system," *Endeavour* **26**, 79 (1967).
- [2] W. H. Southwell, "Gradient-index antireflection coatings," *Opt. Lett.* **8**, 584 (1983).
- [3] D. Stavenga, S. Foletti, G. Palasantzas, and K. Arikawa, "Light on the moth-eye corneal nipple array of butterflies," *Proc. Roy. Soc. Lond B Bio.* **273**, 661 (2006).
- [4] M. Kowalczyk, J. Haberko, and P. Wasylczyk, "Microstructured gradient-index antireflective coating fabricated on a fiber tip with direct laser writing," *Opt. Express* **22**, 12545 (2014).
- [5] T. K. Gaylord, W. Baird, and M. Moharam, "Zero-reflectivity high spatial-frequency rectangular-groove dielectric surface-relief gratings," *Appl. Opt.* **25**, 4562 (1986).
- [6] P. Clapham and M. Hutley, "Reduction of lens reflexion by the moth eye principle," *Nature* **244**, 281 (1973).
- [7] P. Lalanne and G. M. Morris, "Antireflection behavior of silicon subwavelength periodic structures for visible light," *Nanotechnology* **8**, 53 (1997).
- [8] Y. Kanamori, M. Sasaki, and K. Hane, "Broadband antireflection gratings fabricated upon silicon substrates," *Opt. Lett.* **24**, 1422 (1999).

- [9] Z. Yu, H. Gao, W. Wu, H. Ge, and S. Y. Chou, "Fabrication of large area subwavelength antireflection structures on si using trilayer resist nanoimprint lithography and liftoff," *J. Vac. Sci. Technol. B* **21**, 2874 (2003).
- [10] S. R. Kennedy and M. J. Brett, "Porous broadband antireflection coating by glancing angle deposition," *Appl. Opt.* **42**, 4573 (2003).
- [11] G. Xie, G. Zhang, F. Lin, J. Zhang, Z. Liu, and S. Mu, "The fabrication of subwavelength anti-reflective nanostructures using a bio-template," *Nanotechnology* **19**, 095605 (2008).
- [12] C.-J. Ting, C.-F. Chen, and C. Chou, "Subwavelength structures for broadband antireflection application," *Opt. Commun.* **282**, 434 (2009).
- [13] Y. Li, J. Zhang, S. Zhu, H. Dong, F. Jia, Z. Wang, Z. Sun, L. Zhang, Y. Li, H. Li, W. Xu, and B. Yang, "Biomimetic surfaces for high-performance optics," *Adv. Mater.* **21**, 4731 (2009).
- [14] W.-L. Min, B. Jiang, and P. Jiang, "Bioinspired self-cleaning antireflection coatings," *Adv. Mater.* **20**, 3914 (2008).
- [15] Z. Han, Z. Wang, X. Feng, B. Li, Z. Mu, J. Zhang, S. Niu, and L. Ren, "Antireflective surface inspired from biology: A review," *Biosurf. Biotribol.* **2**, 137 (2016).
- [16] R. Weiblen, C. Menyuk, L. Busse, L. Shaw, J. Sanghera, and I. Aggarwal, "Optimized moth-eye anti-reflective structures for as 2 s 3 chalcogenide optical fibers," *Opt. Express* **24**, 10172 (2016).
- [17] H. Kasugai, K. Nagamatsu, Y. Miyake, A. Honshio, T. Kawashima, K. Iida, M. Iwaya, S. Kamiyama, H. Amano, I. Akasaki, H. Kinoshita, and H. Shiomi,

- “Light extraction process in moth-eye structure,” *Phys. Status Solidi C* **3**, 2165 (2006).
- [18] C. Marichy, N. Muller, L. S. Froufe-Pérez, and F. Scheffold, “High-quality photonic crystals with a nearly complete band gap obtained by direct inversion of woodpile templates with titanium dioxide,” *Sci. Rep.* **6**, 21818 (2016).
- [19] X. Zhang, J. Zhang, Z. Ren, X. Li, X. Zhang, D. Zhu, T. Wang, T. Tian, and B. Yang, “Morphology and wettability control of silicon cone arrays using colloidal lithography,” *Langmuir* **25**, 7375 (2009).
- [20] Y. Li, J. Zhang, S. Zhu, H. Dong, F. Jia, Z. Wang, Y. Tang, L. Zhang, S. Zhang, and B. Yang, “Bioinspired silica surfaces with near-infrared improved transmittance and superhydrophobicity by colloidal lithography,” *Langmuir* **26**, 9842 (2010).
- [21] V. Lucarini, J. J. Saarinen, K.-E. Peiponen, and E. M. Vartiainen, *Kramers-Kronig relations in optical materials research*, vol. 110, (Springer Science & Business Media 2005).
- [22] W. Cai and V. Shalaev, *Optical metamaterials: fundamentals and applications*, (Springer Science & Business Media 2009).
- [23] D. B. Fullager, G. D. Boreman, and T. Hofmann, “Infrared dielectric response of nanoscribe ip-dip and ip-l monomers after polymerization from 250 cm^{-1} to 6000 cm^{-1} ,” *Opt. Mater. Express* **7**, 888 (2017).
- [24] K. Hinrichs, A. Furchner, J. Rappich, and T. W. Oates, “Polarization-dependent and ellipsometric infrared microscopy for analysis of anisotropic thin films,” *J. Phys. Chem. C* **117**, 13557 (2013).

CHAPTER 4: NEAR INFRARED TRANSMITTANCE ENHANCEMENT USING
FULLY CONFORMAL ANTI-REFLECTIVE STRUCTURED SURFACES ON
MICROLENSSES FABRICATED BY DIRECT LASER WRITING¹

4.1 Abstract

Structured surfaces composed of subwavelength-sized features offer multifunctional properties including anti-reflective characteristics which are increasingly important for the development of micro-optical components. Here, three-dimensional direct laser writing, via two-photon polymerization, is used to fabricate plano-convex spherical microlenses with anti-reflective structured surfaces. The surfaces are composed of subwavelength-sized conicoid structures which were arranged fully conformal to the convex surface of the microlenses. The dimensions of the conicoid structures were optimized to effectively reduce Fresnel reflection loss over a wide band in the near-infrared spectral range from 1.4 to 2.2 μm , with a maximum reduction at 1.55 μm . Infrared reflection and transmission measurements were used, in combination with three-dimensional finite element calculations, to investigate the performance of the microlenses. The experimental results reveal that in the spectral range from 1.4 to 2.2 μm an effective suppression of the Fresnel reflection loss at the convex surface of spherical microlenses can be achieved. The transmittance enhancement is ranging from 1-3% for spherical microlenses with anti-reflective structured surfaces, in comparison to an uncoated reference.

¹Y. Li, T. Hofmann, *et al.*, *Opt. Eng.* **58**, 010501 (2019). Reprinted with permission © SPIE.

4.2 Introduction

Microlenses are ubiquitous optical components with numerous applications ranging from imaging [1] and sensing [2], to optical interconnects [3], and even photovoltaics [4, 5]. The optical performance of microlenses is impaired by Fresnel reflection losses, which are traditionally suppressed by use of multi-layered, thin-film anti-reflective (AR) coatings [6, 7, 8]. Fabrication requirements and properties of these multi-layered, thin-film AR coatings have several inherent drawbacks, such as susceptibility to thermal deformation and stresses, limited range of suitable materials, and incident angle sensitivity, for instance [9]. These can substantially hinder the applicability of multi-layered, thin-film AR coatings for microlenses which often have a very short radius of curvature [10, 11]. Single-layered AR surfaces composed of subwavelength-sized structures have been introduced more recently [12, 13]. These antireflective structured surfaces (ARSSs) address some of the critical shortcomings of multi-layered, thin-film AR coatings. In addition, ARSSs allow the tailoring of the index profile [14], and enable frequency-independent Fresnel reflection reduction if randomized ARSSs are used [15]. Furthermore, ARSSs can be designed to exhibit multifunctional properties such as hydro- and oleophobic characteristics [16, 17]. Moreover, ARSSs are commonly fabricated using a single material component and can be directly fabricated on lens substrate material which can significantly simplify the fabrication process.

It is well known that the optical properties of ARSSs depend critically on its constituents' structural parameters, such as shape, height, periodic distance (pitch), volume density, and arrangement [18]. The dependence on the constituents' geometry and arrangement has been studied in detail and was optimized for planar surfaces [19, 20, 21, 22]. Information on conformal ARSSs optimized for microlenses, however, is sparse. This is due to a lack of flexible fabrication approaches for conformal ARSSs. So far, notable works applied nanoimprint [23, 13, 24], interference

lithography [25, 12], or plasma etching [26, 27, 28] for the fabrication of conformal ARSSs. While providing efficient access to large scale manufacturing, these fabrication strategies have limited capabilities for rapidly prototyping and simultaneous optimization of the optical performance of the microlenses and the ARSS. In addition, ARSSs fabricated with these techniques often suffer from density variations within the ARSS across curved surfaces, rendering the ARSSs not fully conformal, thus adversely impacting their optical performance.

Three-dimensional direct laser writing (3D-DLW) might provide an attractive avenue for the fabrication of ARSSs and has been recently demonstrated by Kowalczyk *et al.* for the first time [21]. However, 3D-DLW-based fabrication of microlenses with conformal ARSSs has not been reported yet despite the recent success in the fabrication of bare microlenses using this technique [29, 30].

In this letter, we demonstrate a 3D-DLW-based, rapid prototyping approach for the fabrication of plano-convex spherical microlenses, with fully conformal broadband ARSSs for the near-infrared spectral range. The dimensions of the ARSS constituents are optimized for achieving maximum AR performance in the vicinity of the telecommunication wavelength of $1.55 \mu\text{m}$. Our observations show that 3D-DLW allows for rapid fabrication and cost-effective optimization of fully conformal ARSSs, in combination with microlenses designed for the infrared spectral range, when compared to previously demonstrated methods.

4.3 Materials and methods

The structural features of the ARSS was optimized and then integrated into the convex surface of a simple plano-convex microlens, with a base diameter of $100 \mu\text{m}$ and a curvature of $0.01 \mu\text{m}^{-1}$. The effective focal length of the microlens was $189 \mu\text{m}$ resulting in an f-number of 1.89 for operation at a wavelength of $1.55 \mu\text{m}$. The microlenses and ARSSs were fabricated in a single fabrication step using 3D-DLW with one photo-polymer (IP-Dip). The fabricated microlenses are investigated using

FTIR reflection and transmission measurements. We observe an increase of 1-3% in transmittance for the microlenses investigated here. Complementary SEM and optical microscopy were used to confirm the geometry of the microlenses, and the integrity of the conformal ARSS. Three-dimensional finite-element method (3D-FEM) reflection calculations using COMSOL were employed to evaluate and optimize the optical performance of the ARSS prior to the 3D-DLW fabrication.

The ARSS employed here is composed of conicoid subwavelength-sized structures which are arranged in hexagonal closed-packed fashion conformal to the convex surface of the microlens. The ARSS was optimized for the spectral range from $1.4 \mu\text{m}$ to $2.2 \mu\text{m}$ using Bruggemann effective medium homogenization by varying the parameters of the ARSS constituents (base diameter D and height H of the conicoids and their lateral separation P , see inset of Fig. 4.1) as described in detail in our previous work [19]. Note that the dielectric function of IP-Dip used for these calculations was obtained by variable angle IR ellipsometry and is reported elsewhere [31].

For an ARSS composed of IP-Dip conicoid subwavelength-sized structures, the lowest reflectance for the spectral range from $1.4 \mu\text{m}$ to $2.2 \mu\text{m}$ is obtained at $\lambda = 1.55 \mu\text{m}$ for $P = 0.9 \mu\text{m}$, $D = 0.8 \mu\text{m}$ and $H = 0.83 \mu\text{m}$, compared the reflectance of a planar IP-Dip surface which is 5.1%. Note that the fully conformal arrangement of the ARSSs designed and fabricated here results in conicoid structures normal to the convex surface of the microlens while preserving a constant lateral separation. Thus, simple planar surface models are suitable for the analytical and numerical evaluation of the optimal performance of the ARSS coated microlenses.

4.4 Results and discussion

Figure 4.1 depicts 3D-FEM calculated relative reflectance data for an IP-Dip ARSS, which was obtained using the reflection spectra ratio of the IP-Dip ARSS to a planar IP-Dip substrate, over a spectral range from $1.4 \mu\text{m}$ to $2.2 \mu\text{m}$ as a function of the angle of incidence. The range of the incident angle from 0° to 30° is determined

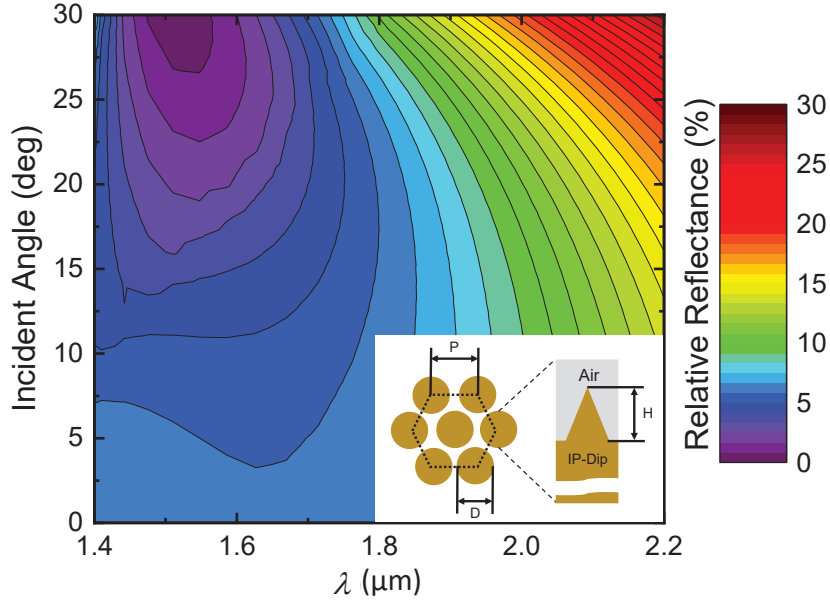


Figure 4.1: Contour plot of relative specular reflectance obtained using 3D-FEM calculations, as a function of angle of incidence ranging from 0° to 30° , for the spectral range from $1.4 \mu\text{m}$ to $2.2 \mu\text{m}$. The geometry of the ARSS is shown in the inset. A lateral spacing $P = 0.9 \mu\text{m}$, cone diameter $D = 0.8 \mu\text{m}$, and cone height $H = 0.83 \mu\text{m}$ was used for the calculations. The complex dielectric properties for IP-Dip were obtained from variable angle spectroscopic ellipsometry measurements [31]. Note that the reflectance of IP-Dip over the corresponding incident angles was used as a reference.

by considering the optical configuration of the Cassegrain objective used for the reflectance measurements and the variation of surface normal across the measured area of the microlens. A decrease in relative reflection of at least 30% is observed over the entire spectral and angle of incidence range of interest. In the vicinity of the telecommunication wavelength $\lambda = 1.55 \mu\text{m}$ the ARSS is most effective as expected based on the optimization described in Ref. [19]. A minimum in the relative reflectance occurs for incidence angles larger than 20° where the calculated relative reflectance is as low as 0.2%.

Three-dimensional renderings of the microlenses with and without the ARSS coating are shown in Fig. 4.2 (a) and (b), respectively. The inset of Fig. 4.2 (b) shows a closeup of the 3D rendering of ARSS coated microlens in order to provide structural

details of the AR constituents which are homogeneously and conformally distributed in hexagonal lattice pattern across the convex lens surface.

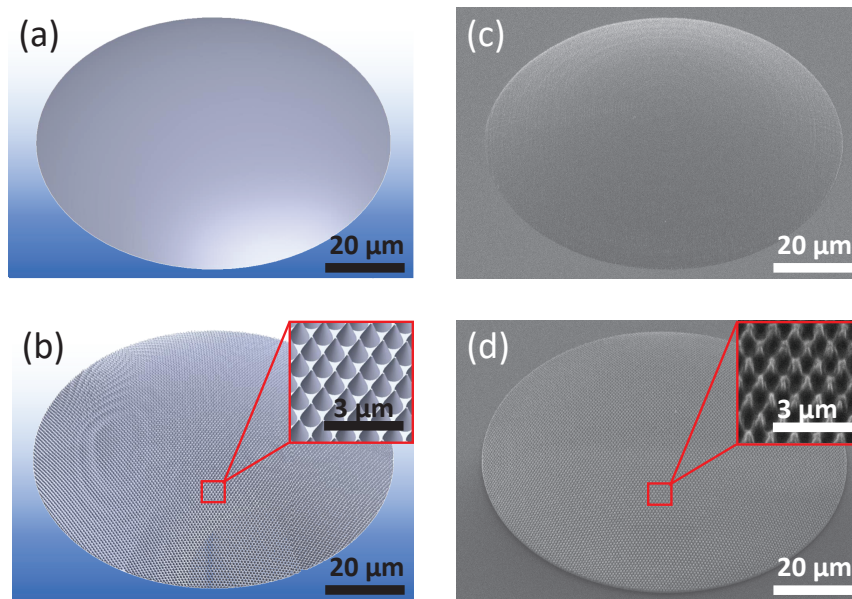


Figure 4.2: 3D rendering of the nominal design of a bare plano-convex spherical microlens and a corresponding microlens with an ARSS is shown in (a) and (b), respectively. Both microlenses have a base diameter $100\ \mu\text{m}$. The inset in panel (b) depicts a closeup of the 3D rendering of the ARSS showing the hexagonal lattice pattern of the conicoid ARSS constituents. Corresponding SEM micrographs of the fabricated bare microlens and the microlens with the conformal ARSS on the convex side are depicted in (c) and (d), respectively. The inset in panel (d) shows a closeup of the ARSS on the microlens. 3D renderings and micrographs were obtained with a 45° tilt with respect to the surface normal.

Two plano-convex microlenses were fabricated by polymerizing IP-dip monomer on glass substrates using a commercially available 3D-DLW system (Photonic Professional GT, Nanoscribe, GmbH). One microlens was fabricated with an ARSS conformal to the convex surface while the other microlens was fabricated with a bare convex surface to serve as a reference. Both microlenses were fabricated in a single 3D-DLW fabrication step using identical exposure doses which were optimized prior to the synthesis. After fabrication, the unpolymerized monomer is removed by immersion in propylene glycol monomethyl ether acetate (PGMEA, Baker 220), and subsequently in 99.99% isopropyl alcohol for 20 min and 2 min, respectively. Finally, the remaining

isopropyl alcohol is evaporated by blow-drying with dry nitrogen.

The AR performance was evaluated using FTIR reflection and transmission measurements. In addition, scanning electron microscopy (SEM) was used to determine the conformality and structural quality of the fabricated ARSS on top of the microlenses, and complementary optical microscopy was employed to evaluate the curvature of the fabricated microlenses.

Figures 4.2 (c) and (d) show SEM micrographs of the fabricated bare and the ARSS coated microlens, respectively. It can be clearly seen that the ARSS conformally follows the convex surface of the microlens. Comparing the insets of Figs. 4.2 (b) and (d) a true-to-form geometry and hexagonal surface arrangement of the fabricated conicoid constituents of the ARSS can be observed.

With optical microscopy, the evaluation of the fabricated microlenses' curvature was carried out via an experimental verification of the corresponding effective focal length under white light illumination. The experimentally determined effective focal length is $175 \pm 5 \mu\text{m}$ for both microlenses, consistent with the nominal effective focal length of $180 \mu\text{m}$ given by the lens curvature ($0.01 \mu\text{m}^{-1}$) and the refractive index of IP-dip ($n = 1.55$) for visible light illumination [32].

The optical performance of the microlenses were investigated by reflection and transmission IR microscopy measurements in spectral range from $1.4 \mu\text{m}$ to $2.2 \mu\text{m}$ using a FTIR spectrometer in conjunction with an IR microscope (VERTEX 70 and HYPERION 3000, Bruker, Inc.). A $15\times$ Cassegrain objective is used for the reflection measurements whereas the transmission measurements used a complementary $15\times$ Cassegrain condenser. The Cassegrain illumination configuration results in a range of angles of incidence from 10.8° to 23.5° defined by the numerical aperture of the Cassegrain objectives and the diameter of their central mirrors [33].

Figure 4.3 depicts the experimental data for the relative reflectance (blue solid line) and transmittance (red solid line) spectra of the microlens with the conformal ARSS.

Note that the absolute reflectance and transmittance of the bare microlens was used as a reference, respectively. On average a 2% increase in relative transmission is observed across the investigated spectral range due to the conformal ARSS treatment of the convex microlens surface. This is in good agreement with the observed 40% reduction in relative reflectance indicating negligible absorption and scattering losses.

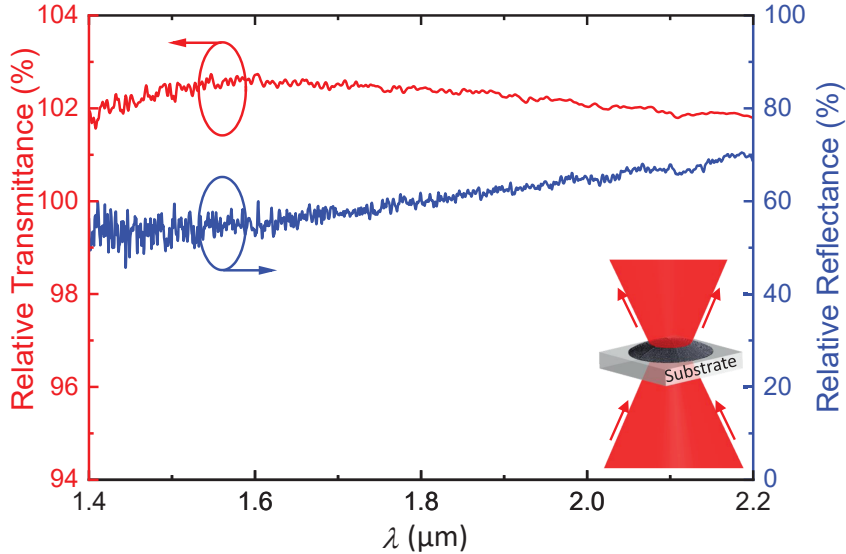


Figure 4.3: Relative reflectance (blue solid line) and transmittance (red solid line) spectra of the ARSS treated microlens (Fig. 4.2(b) and (d)) measured by FTIR microscopy in the range from 1.4 to 2.2 μm using the absolute reflectance and transmittance of a bare microlens shown in Fig. 4.2(a) and (c) as a reference, respectively. The microlenses were mounted such that convex surface of the microlens faced the Cassegrain objective as shown in the inset.

4.5 Conclusion

In conclusion, we demonstrated that 3D-DLW is an effective method for the fabrication of microlenses including conformal functional coatings for the near infrared spectral range. Here an ARSS composed of subwavelength-sized conicoid structures was optimized for the near infrared spectral range and effectively used to reduce the Fresnel reflection loss at the convex surface of plano-convex spherical microlenses. A structural comparison between the nominal and as-fabricated microlenses shows a good agreement on both micron- and sub-micron-sized structural features, and

illustrates the effectiveness of 3D-DLW as a rapid prototyping tool for fabricating optical components including functional coatings with multi-scale features in a single fabrication step.

Our experimental reflectance and transmittance spectra obtained using FTIR microscopy found a 2% improvement in transmission and a 40% reduction in reflection over the spectral range from 1.4 to 2.2 μm . These results are in good agreement with 3D-FEM calculations which corroborated the experimentally observed reflectance minimum at 1.55 μm . Optical imaging was used to demonstrate the functionality of the microlenses with and without ARSS coating and verify the focal length of the microlenses. We find that 3D-DLW could offer an elegant avenue for the rapid prototyping of optical components including conformal functional coatings for the infrared spectral range.

REFERENCES

- [1] J. Arai, H. Kawai, and F. Okano, “Microlens arrays for integral imaging system,” *Appl. Opt.* **45**, 9066 (2006).
- [2] M. Vekshin, A. Levchenko, A. Nikitin, V. Nikitin, and N. Yacovenko, “Glass microlens arrays for shack–hartmann wavefront sensors,” *Meas. Sci. Technol.* **21**, 054010 (2010).
- [3] C. A. Edwards, H. M. Presby, and C. Dragone, “Ideal microlenses for laser to fiber coupling,” *J. Lightwave Technol.* **11**, 252 (1993).
- [4] J. H. Karp, E. J. Tremblay, and J. E. Ford, “Planar micro-optic solar concentrator,” *Opt. Express* **18**, 1122 (2010).
- [5] T. Hou, C. Zheng, S. Bai, Q. Ma, D. Bridges, A. Hu, and W. Duley, “Fabrication, characterization, and applications of microlenses,” *Appl. Opt.* **54**, 7366 (2015).
- [6] E. Pawlowski, H. Engel, M. Ferstl, W. Fuerst, and B. Kuhlow, “Diffractive microlenses with antireflection coatings fabricated by thin film deposition,” *Opt. Eng.* **33**, 647 (1994).
- [7] U. Schulz, “Review of modern techniques to generate antireflective properties on thermoplastic polymers,” *Appl. Opt.* **45**, 1608 (2006).
- [8] P. Schnauber, A. Thoma, C. V. Heine, A. Schlehahn, L. Gantz, M. Gschrey, R. Schmidt, C. Hopfmann, B. Wohlfeil, J.-H. Schulze, *et al.*, “Bright single-photon sources based on anti-reflection coated deterministic quantum dot microlenses,” *Technologies* **4**, 1 (2015).

- [9] S. S. Oh, C.-G. Choi, and Y.-S. Kim, "Fabrication of micro-lens arrays with moth-eye antireflective nanostructures using thermal imprinting process," *Microelectron. Eng.* **87**, 2328 (2010).
- [10] J.-Q. Xi, M. F. Schubert, J. K. Kim, E. F. Schubert, M. Chen, S.-Y. Lin, W. Liu, and J. A. Smart, "Optical thin-film materials with low refractive index for broadband elimination of fresnel reflection," *Nat. Photonics* **1**, 176 (2007).
- [11] U. Schulz, "Broadband antireflection coatings for optical lenses," *SPIE Newsroom* 2-4 (2015).
- [12] B. Päivänranta, P.-Y. Baroni, T. Scharf, W. Nakagawa, M. Kuittinen, and H. P. Herzig, "Antireflective nanostructured microlenses," *Microelectron. Eng.* **85**, 1089 (2008).
- [13] J.-T. Wu, W.-Y. Chang, and S.-Y. Yang, "Fabrication of a nano/micro hybrid lens using gas-assisted hot embossing with an anodic aluminum oxide (aao) template," *J. Micromech. Microeng.* **20**, 075023 (2010).
- [14] W. H. Southwell, "Gradient-index antireflection coatings," *Opt. Lett.* **8**, 584 (1983).
- [15] L. E. Busse, C. M. Florea, J. A. Frantz, L. B. Shaw, I. D. Aggarwal, M. K. Poutous, R. Joshi, and J. S. Sanghera, "Anti-reflective surface structures for spinel ceramics and fused silica windows, lenses and optical fibers," *Opt. Mater. Express* **4**, 2504 (2014).
- [16] L. Peng, C. Zhang, H. Wu, P. Yi, X. Lai, and J. Ni, "Continuous fabrication of multiscale compound eyes arrays with antireflection and hydrophobic properties," *IEEE Trans. Nanotechnol.* **15**, 971 (2016).

- [17] A. Cavalli, P. Bøggild, and F. Okkels, “Parametric optimization of inverse trapezoid oleophobic surfaces,” *Langmuir* **28**, 17545 (2012).
- [18] D. Stavenga, S. Foletti, G. Palasantzas, and K. Arikawa, “Light on the moth-eye corneal nipple array of butterflies,” *Proc. Roy. Soc. Lond B Bio.* **273**, 661 (2006).
- [19] Y. Li, D. Fullager, E. Angelbello, D. Childers, G. Boreman, and T. Hofmann, “Broadband near-infrared antireflection coatings fabricated by three-dimensional direct laser writing,” *Opt. Lett.* **43**, 239 (2018).
- [20] R. Weiblen, C. Menyuk, L. Busse, L. Shaw, J. Sanghera, and I. Aggarwal, “Optimized moth-eye anti-reflective structures for as 2 s 3 chalcogenide optical fibers,” *Opt. Express* **24**, 10172 (2016).
- [21] M. Kowalczyk, J. Haberko, and P. Wasylczyk, “Microstructured gradient-index antireflective coating fabricated on a fiber tip with direct laser writing,” *Opt. Express* **22**, 12545 (2014).
- [22] S. Ji, K. Song, T. B. Nguyen, N. Kim, and H. Lim, “Optimal moth eye nanostructure array on transparent glass towards broadband antireflection,” *ACS applied materials & interfaces* **5**, 10731 (2013).
- [23] Y.-P. Chen, C.-H. Lee, and L. A. Wang, “Fabrication and characterization of multi-scale microlens arrays with anti-reflection and diffusion properties,” *Nanotechnology* **22**, 215303 (2011).
- [24] H. K. Raut, S. S. Dinachali, Y. C. Loke, R. Ganesan, K. K. Ansah-Antwi, A. Gora, E. H. Khoo, V. A. Ganesh, M. S. Saifullah, and S. Ramakrishna, “Multiscale ommatidial arrays with broadband and omnidirectional antireflection and antifogging properties by sacrificial layer mediated nanoimprinting,” *ACS Nano* **9**, 1305 (2015).

- [25] P.-Y. Baroni, B. Päivänranta, T. Scharf, W. Nakagawa, M. Roussey, M. Kuittinen, and H. P. Herzig, “Nanostructured surface fabricated by laser interference lithography to attenuate the reflectivity of microlens arrays,” *J. Eur. Opt. Soc-Rapid* **5** (2010).
- [26] J. W. Leem, Y. M. Song, and J. S. Yu, “Biomimetic artificial si compound eye surface structures with broadband and wide-angle antireflection properties for si-based optoelectronic applications,” *Nanoscale* **5**, 10455 (2013).
- [27] H. Jung and K.-H. Jeong, “Monolithic polymer microlens arrays with antireflective nanostructures,” *Appl. Phys. Lett.* **101**, 203102 (2012).
- [28] Y. M. Song, G. C. Park, S. J. Jang, J. H. Ha, J. S. Yu, and Y. T. Lee, “Multifunctional light escaping architecture inspired by compound eye surface structures: From understanding to experimental demonstration,” *Opt. Express* **19**, A157 (2011).
- [29] T. Gissibl, S. Thiele, A. Herkommer, and H. Giessen, “Two-photon direct laser writing of ultracompact multi-lens objectives,” *Nat. Photonics* **10**, 554 (2016).
- [30] N. Tsutsumi, J. Hirota, K. Kinashi, and W. Sakai, “Direct laser writing for micro-optical devices using a negative photoresist,” *Opt. Express* **25**, 31539 (2017).
- [31] D. B. Fullager, G. D. Boreman, and T. Hofmann, “Infrared dielectric response of nanoscribe ip-dip and ip-l monomers after polymerization from 250 cm^{-1} to 6000 cm^{-1} ,” *Opt. Mater. Express* **7**, 888 (2017).
- [32] T. Gissibl, S. Wagner, J. Sykora, M. Schmid, and H. Giessen, “Refractive index measurements of photo-resists for three-dimensional direct laser writing,” *Opt. Mater. EXPRESS* **7**, 2293 (2017).

- [33] K. Hinrichs, A. Furchner, J. Rappich, and T. W. Oates, “Polarization-dependent and ellipsometric infrared microscopy for analysis of anisotropic thin films,” *J. Phys. Chem. C* **117**, 13557 (2013).

CHAPTER 5: FABRICATION OF OPTICAL COMPONENTS WITH NM- TO MM-SCALE CRITICAL FEATURES USING THREE-DIMENSIONAL DIRECT LASER WRITING¹

5.1 Abstract

A powerful fabrication strategy based on three-dimensional direct laser writing for the rapid prototyping of opto-mechanical components with critical features ranging from several hundred nm to a few mm is demonstrated here. As an example, a simple optical fiber connector with optical and mechanical guides as well as integrated micro-optical elements with nano-structured surfaces is designed and fabricated. In contrast to established three-dimensional direct laser writing, two different polymers are combined in the fabrication process in order to achieve a drastic reduction in fabrication time by substantially reducing the “optical tool path”. A good agreement between the as-fabricated connector and nominal dimensions has been obtained. The developed approach allows the rapid prototyping of optomechanical components with multi-scale critical features. It is, therefore, envisioned to substantially accelerate the development cycle by integrating functional mechanical and optical elements in a single component.

5.2 Introduction

Three-dimensional direct laser writing (3D-DLW) based on two-photon polymerization is a widely employed additive manufacturing technique since Deubel *et al.* used

¹Y. Li, T. Hofmann, *et al.*, 2019 *IEEE 16th International Conference on Smart Cities: Improving Quality of Life Using ICT & IoT and AI (HONET-ICT)*, 239 (2019). © 2019 IEEE. Personal use of this material is permitted. Permission from IEEE must be obtained for all other uses, in any current or future media, including reprinting/republishing this material for advertising or promotional purposes, creating new collective works, for resale or redistribution to servers or lists, or reuse of any copyrighted component of this work in other works.

this approach in 2004 to synthesize infrared photonic crystals [1]. Since then, this unique additive fabrication technique has been successfully used for the fabrication of structured optical components with μm - and even nm-scale critical dimensions. 3D-DLW allows the polymerization of a photosensitive material within the free-space volume, a so called voxel, which is substantially smaller compared to voxel sizes which can be achieved using conventional single-photon polymerization techniques. The voxel dimensions are typically in the range from hundreds of nm to several μm . This technique is therefore suitable for the applications ranging from the rapid prototyping of micro-optical components to the synthesis of complex optical metamaterials with sub-wavelength-sized building blocks for the infrared and even visible spectral range [2, 3, 4]. In recent years the rapid prototyping of optical components applied in various optical fields, including functional coatings [5, 6], metasurfaces [7, 8], structured photonics [9, 10], and micro-optics [11, 12, 13] has been shown.

In addition to applications of 3D-DLW for the fabrication of optical elements with microscopic dimensions, recent decades have also witnessed intensive research efforts devoted to the development of mechanical components with macroscopic dimensions (mm-scale) by using the 3D-DLW approach [14, 15, 16]. In comparison with the other techniques for the fabrication of macroscopic mechanical parts, 3D-DLW can fabricate a mechanical part with a complex structural configuration in a single-step without involving additional manufacturing procedures. Furthermore, 3D-DLW simplifies the manufacturing complexity which can often result in a lower manufacturing time and a reduction of the fabrication costs. From an application perspective in an industrial environment, 3D-DLW is a promising tool for rapid prototyping of novel opto-mechanical components and could accelerate the product development cycle.

The capabilities of the 3D-DLW process to fabricate structures with either microscopic or macroscopic features have been extensively studied individually. However, approaches on how to utilize the 3D-DLW technique for the synthesis of structures

which contain critical features ranging from nm- to mm-scales, has not been reported yet.

The ability to rapidly prototype such structures has numerous applications for integrated optics and opto-mechanical elements. In order to obtain high quality components with nm- to mm-scale features in a manageable fabrication time, the use of multiple photosensitive materials and objectives is very helpful as will be shown here.

In this paper, hetero-3D-DLW for the fabrication of components with nm- to mm-scale critical features is introduced. This novel approach makes use of two photo-resists in order to achieve a substantial reduction in the “optical tool path”, thereby dramatically reducing the fabrication time. As an example, the fabrication of a optical fiber connector (mm-scale) is described. The connector contains mechanical alignment guides as well as multiple fiber guides which are equipped with microlenses (μm -scale). In order to further demonstrate the capability to fabricate structures with nm-scale dimensions, the surface of one of the microlenses was coated with an anti-reflective structured surface (ARSS, nm-scale).

5.3 Experiment

5.3.1 Sample design

The necessary procedures required for the 3-DLW-based fabrication of components with nm- to mm-scale critical features are demonstrated here, using a simple fiber connector as an example. The fiber connector was designed to include mm-scale external dimensions. It consists of mechanical as well as fiber guides and microlenses with μm -scale features. The capability to fabricate nm-scale structures is shown by integrating an ARSS which conformally coats the convex surface of one of the microlenses. The fabrication strategies developed here are not limited to this simple example, but can be employed for a wide range of applications where optical components consisting of features with nm- to mm-scale critical features are desired. A

CAD rendering of the fiber connector is shown in Fig. 5.1.

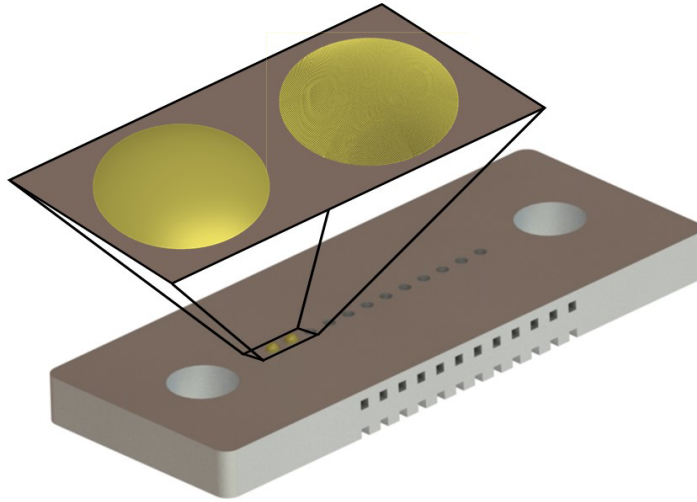


Figure 5.1: CAD rendering of the fiber connector. The outer dimensions of the connector are on the mm-scale, while it contains elements with drastically smaller critical dimensions. Located at the left and right of the connector are mechanical guides which are designed to guide a receptacle with high-precision onto the connector. Located within the body of the connector are 12 fiber guides. For demonstration purposes 10 of these fiber guides are bare, 2 are equipped with plano-convex microlenses. One of the microlenses is conformally coated with a structured surface to form a anti-reflection coating (the right microlens in the inset).

The fiber connector has the shape of a rectangular cuboid (length=6.4 mm, width=2.5 mm, and height=0.5 mm) and contains 12 cylindrical fiber guides with a diameter of $127 \mu\text{m}$. The cylinder axis of the fiber guides is oriented normal to the fiber connector face. In addition to the fiber guides, the connector also includes two cylindrical mechanical alignment guides with a diameter of $700 \mu\text{m}$. These alignment guides are designed to receive the mechanical alignment pins of a receptacle, thereby ensuring the accurate alignment of the connector and the receptacle. Consequently, this will provide an accurate alignment of the optical fibers within the connector and the receptacle component.

In order to ensure that the cylindrical fiber guides are accurately fabricated, 12 pairs of micro-channels were included at the bottom of the fiber connector as shown in Fig. 5.1. These micro-channels with a cross section of $100 \mu\text{m} \times 100 \mu\text{m}$ are connected

to the fiber guides and are oriented normal to the side planes of the fiber connector. Thereby the micro-channels aid in the removal of unpolymerized monomer after the polymerization step, during the development procedure. This simple micro-fluidic design substantially reduces the development time and ensures the complete removal of monomer within the fiber guides. The micro-fluidic channels further enable the inclusion of microlenses located at the top of the fiber guides. Without the micro-fluidic channels excess monomer would be trapped within the fiber guides between the substrate surface and lenslet located at opposing ends of the fiber guide.

For demonstration purposes, a pair of microlenses with and without an ARSS coating were included at the top of two fiber guides (as shown in the inset in Fig. 5.1). ARSSs are well-known bio-inspired coatings which reduce Fresnel reflection loss [17]. Here the ARSS are composed of subwavelength conicoid structures arranged in a hexagonal lattice pattern. The structural parameters of the conicoid structures, including height, pitch, lateral fill fraction, were optimized for a broadband anti-reflective behavior over spectral range from $1.4 \mu\text{m}$ to $2.2 \mu\text{m}$, while the optimal performance (40% reduction in reflection and 2% improvement in transmission) occurred at the telecommunication wavelength of $1.55 \mu\text{m}$, as shown in Fig. 5.2.

The structural features of the ARSS were integrated into the convex surface of a simple planoconvex microlens, with a based diameter of $130 \mu\text{m}$ and a curvature of $0.01 \mu\text{m}^{-1}$. The effective focal length of the microlens is $189 \mu\text{m}$ resulting in an f -number of 1.89 for operation at a wavelength of $1.55 \mu\text{m}$. The two insets in Fig. 5.2 show the SEM micrographs of the investigated bare microlens and ARSS coated microlens, respectively. For information about the design of the conformal ARSS coated microlens, the interested reader is referred to our previous publications [17, 18].

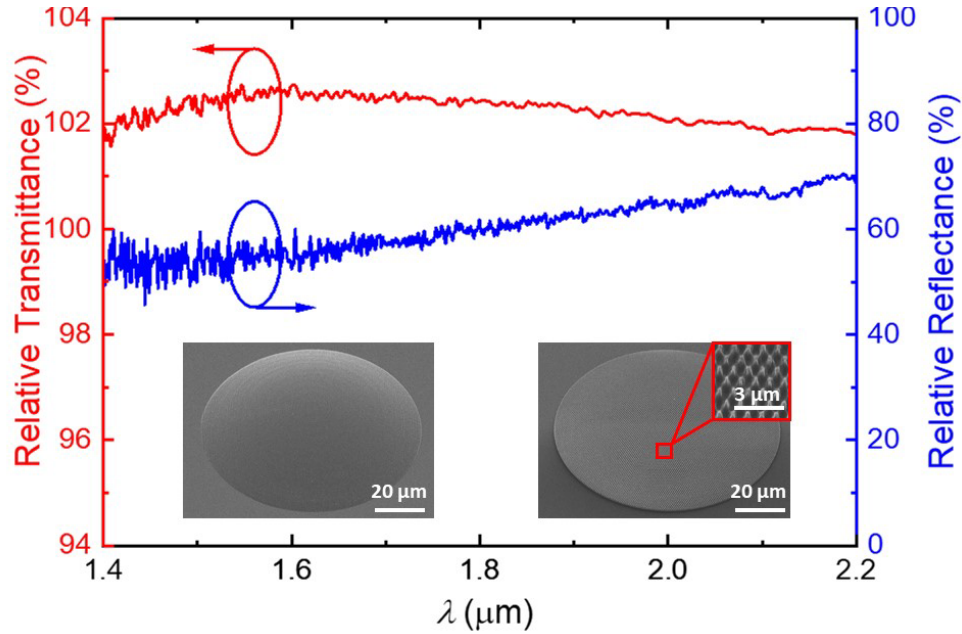


Figure 5.2: Relative reflectance (blue-solid line) and transmittance (red-solid line) spectra of an ARSS-treated microlens (right inset) measured by FTIR microscopy in the range from 1.4 to 2.2 μm using the absolute reflectance and transmittance of a bare microlens (left inset) as a reference, respectively.

5.3.2 Sample fabrication

The fiber connector including the microlenses with and without the ARSS coating was fabricated using a commercially available 3D-DLW system (Photonic Professional GT, Nanoscribe, GmbH). The employed process steps are illustrated in Fig. 5.3. Note, the objective focal lengths, as shown in Fig. 5.3 (a) and (c), are exaggerated for illustration purposes. Both objectives are immersed in the photoresist during the polymerization process.

As the first step, the features of the fiber connector which require the lowest spatial resolution were fabricated on a glass substrate as shown in Fig. 5.3 (a). During this step the rectangular cuboid (see Fig. 5.1) including the mechanical and optical guides as well as the micro-fluidic channels is polymerized. In order to expedite the fabrication process a 25 \times immersion objective was used in combination with the photoresist IP-S. Due to the high viscosity of the photoresist IP-S combined

with the large focal spot of the $25\times$ objective, voxel dimensions on the order of several micrometers are achievable. This allows for a larger distance between the layers which have to be polymerized as well. This reduction in “optical tool path” length substantially reduces the fabrication time while maintaining sufficient spatial resolution.

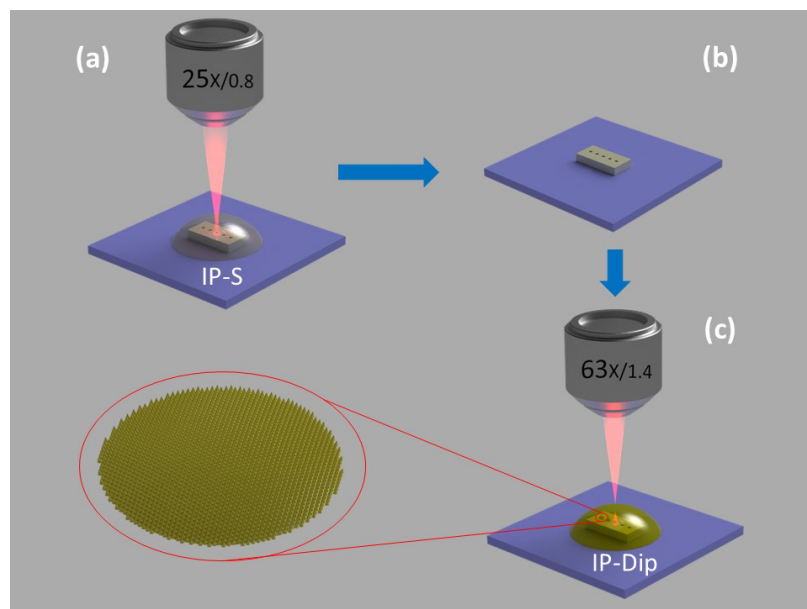


Figure 5.3: Schematic of the fabrication process. (a) illustrates the polymerization of the components which required the lowest spatial resolution. For this purpose a $25\times$ immersion objective was used in combination with IP-S photoresist. (b) after the polymerization the access monomer was removed as described in the text. (c) illustrates the subsequent fabrication of the bare and ARSS coated microlenses. The critical features of microlenses and coatings require resolutions in the μm to nm range. A $63\times$ immersion objective was used in combination with IP-Dip photoresist in order to achieve this resolution. Note, the objective focal lengths, as shown in Fig. 5.3 (a) and (c), are exaggerated for illustration purposes.

After the first polymerization step illustrated in Fig. 5.3 (a), a developing process was applied to remove the unpolymerized IP-S in order to obtain a dry and clean fiber connector, as shown in Fig. 5.3 (b). The unpolymerized IP-S, was removed by immersing the sample in propylene glycol monomethyl ether acetate (PGMEA) and, subsequently, in 99.99% isopropyl alcohol (IPA) for 40 min and 20 min, respectively. After evaporating the excess IPA in dry nitrogen, the fiber connector was subjected

to a second polymerization step as shown in Fig. 5.3 (c).

The final step aims at fabricating the microlenses with μm -scale dimensions and nm-scale features on top of the fiber guiding holes of the fabricated fiber connector, as shown in Fig. 5.3 (c). In this process step, a $63\times$ immersion objective is used in combination with the less viscous IP-Dip. This combination of objective and photo-resist reduces the effective voxel size to a few hundred nanometers and thereby provides sufficient spatial resolution to fabricate both the bare microlens as well as the microlens with the conformal ARSS coating, which consists of nm-scale conicoid features.

After re-immersing the fiber connector inside a drop of the photo-resist IP-Dip, the sample stage was manually controlled to locate the interface of the fiber guides of the fiber connector. Following this manual alignment procedure, a pair of microlenses was fabricated on top of two fiber guides. While one of the microlenses was fabricated with a bare convex surface, a second microlens was fabricated with a conformal ARSS coating. Following the polymerization, the development process was repeated as before to obtain the final fiber connector consisting of a cuboid connector body, mechanical and fiber guides as well as integrated microlenses with and without ARSS coating. A top-view optical micrograph is depicted in Fig. 5.4 and will be discussed in the next section. It is important to note that the hetero-3D-DLW fabrication approach described above, which combines two different photo-resists and immersion objectives, dramatically reduces the fabrication time. Compared with traditional homo-3D-DLW fabrication, one order of magnitude in fabrication time is saved. The total fabrication time of the fiber connector was approximately 13 hours.

5.4 Results and discussion

The fabricated fiber connector was investigated by using optical microscopy, as shown in Fig. 5.4. In Fig. 5.4 (a), the complete cuboid fiber connector is depicted. A row containing 12 fiber guides can be seen in the center of the cuboid between

the two larger mechanical guides on each side. The first two fiber guides from the left were selected to be covered by two microlenses to demonstrate the hetero-3D-DLW approach here. The remaining 10 fiber guides were not covered to allow a direct inspection. Fig. 5.4 (b) shows a detailed top-view of the fiber guides where no microlenses were added. The diameter of the fiber guides is $127 \pm 0.7 \mu\text{m}$ and in excellent agreement with the design.

The dark orthogonal lines are the result of multiple exposure due to the stitching of areas, which are polymerized in a single step using the galvanometric scanner of the 3D-DLW system. The galvanometric scanner is tuned to produce a slight overlap of adjacent areas. While this overlap ensures the continuity of the fiber connector, it also results in an additional laser exposure of these overlap areas. This leads to an observable optical contrast. The effects of the over exposure on the infrared optical properties of the employed polymers are not studied. We therefore restricted these overlap areas to sections which have no optical and only mechanical functionality as surface finish and mechanical properties of the polymers are thought to be not impaired.

A top-view micrograph of a bare microlens and an ARSS coated microlens are shown in Fig. 5.4 (c) for comparison. The substantial contrast between the bare microlens shown on the left side of the micrograph (bright) and microlens with ARSS coating shown on the right side (dark) originates from scattering at visible wavelengths. The conicoid constituents of the ARSS are designed to operate in the infrared spectral range. At visible wavelengths, however, the conicoid constituents are larger than the wavelength and hence scatter light significantly. The brightness of the bare microlens further indicates the smoothness of the lens surface that has been well constructed without defects. Figure 5.4 (d) provides a detailed top-view of the ARSS coated microlens to show the structure of the AR constituents, which are homogeneously and conformally distributed in a hexagonal lattice pattern across the convex

lens surface. A good agreement on the structural features between the fabricated and designed opto-mechanical component has been obtained.

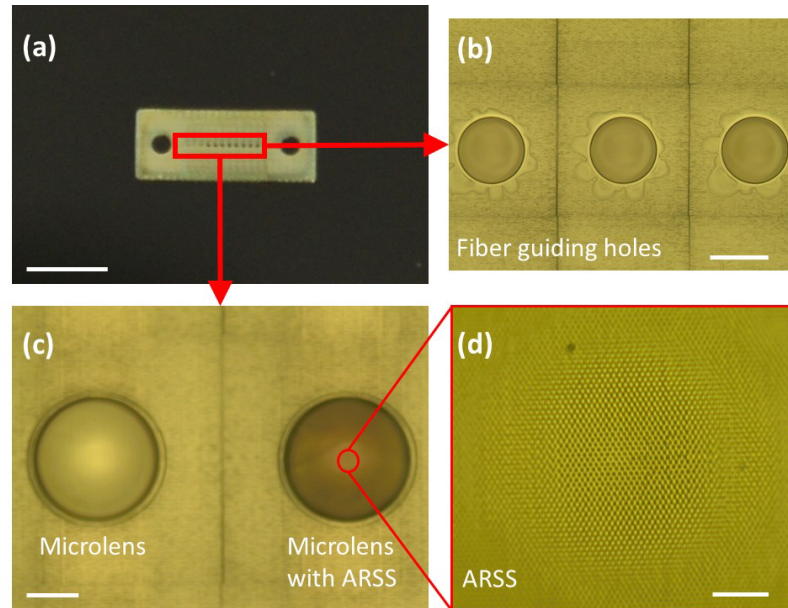


Figure 5.4: Top-view optical micrographs of the fabricated fiber connector showing the entire connector (a), a detailed micrograph of the fiber guides (b), a (c) comparison of a microlens without (left) and with (right) a conformal ARSS coating, and (d) a detailed micrograph of ARSS surface only. The scale bars in (a), (b), (c), and (d) are 2.5 mm, 100 μm , 50 μm , and 10 μm , respectively.

5.5 Conclusion

Hetero-3D-DLW, which has been introduced here as a 3D-DLW process involving multiple polymers, allows the fabrication of opto-mechanical components with multiple scale critical features ranging from the nm- to the mm-scale. The use of different polymers results in a dramatic reduction of the process time of hetero-3D-DLW compared to approaches where only a single polymer-objective combination is used. This is mainly due to the reduction in the “optical tool path”. The polymerization of IP-S with a 25 \times immersion objective and IP-Dip with a 63 \times immersion objective, has been found to allow for the efficient fabrication of mm-scale structures with low spatial resolution requirement (few micrometers) and μm -scale structures with high spatial resolution requirement (few hundred nanometers). A simple fiber connector with a

pair of integrated microlenses with and without ARSS coating has been used to illustrate this fabrication approach. A good agreement between the as-printed sample and nominal dimensions was achieved. In contrast to conventional 3D-DLW where only a single polymer objective combination is used, the hetero-3D-DLW approach shown here allows the fabrication of extremely complex optical components. The combination of different polymers and objectives reduces the process time dramatically. We envision hetero-3D-DLW for the rapid prototyping of opto-mechanical components, which could substantially accelerate the development cycle of opto-mechanical devices by integrating mechanical and optical functionality.

REFERENCES

- [1] M. Deubel, G. Von Freymann, M. Wegener, S. Pereira, K. Busch, and C. M. Soukoulis, "Direct laser writing of three-dimensional photonic-crystal templates for telecommunications," *Nat. Mater.* **3**, 444 (2004).
- [2] I. Sakellari, X. Yin, M. L. Nesterov, K. Terzaki, A. Xomalis, and M. Farsari, "3d chiral plasmonic metamaterials fabricated by direct laser writing: the twisted omega particle," *Adv. Opt. Mater.* **5**, 1700200 (2017).
- [3] J. Moughames, S. Jradi, T. Chan, S. Akil, Y. Battie, A. E. Naciri, Z. Herro, S. Guenneau, S. Enoch, L. Joly, *et al.*, "Wavelength-scale light concentrator made by direct 3d laser writing of polymer metamaterials," *Sci. Rep.* **6**, 33627 (2016).
- [4] V. Caligiuri, R. Dhama, K. Sreekanth, G. Strangi, and A. De Luca, "Dielectric singularity in hyperbolic metamaterials: the inversion point of coexisting anisotropies," *Sci. Rep.* **6**, 20002 (2016).
- [5] Ł. Zinkiewicz, J. Haberko, and P. Wasylczyk, "Highly asymmetric near infrared light transmission in an all-dielectric grating-on-mirror photonic structure," *Opt. Express* **23**, 4206 (2015).
- [6] M. Kowalczyk, J. Haberko, and P. Wasylczyk, "Microstructured gradient-index antireflective coating fabricated on a fiber tip with direct laser writing," *Opt. Express* **22**, 12545 (2014).
- [7] X. Xiong, S.-C. Jiang, Y.-H. Hu, R.-W. Peng, and M. Wang, "Structured metal film as a perfect absorber," *Adv. Mater.* **25**, 3994 (2013).

- [8] B. Jose, R. K. Vijayaraghavan, L. Kent, S. O’Toole, J. O’Leary, and R. J. Forster, “Tunable metallic nanostructures using 3d printed nanosphere templates,” *Electrochem. Commun.* **98**, 106 (2019).
- [9] Y. Li, D. Fullager, S. Park, D. Childers, R. Fesperman, G. Boreman, and T. Hofmann, “High-contrast infrared polymer photonic crystals fabricated by direct laser writing,” *Opt. Lett.* **43**, 4711 (2018).
- [10] C. Marichy, N. Muller, L. S. Froufe-Pérez, and F. Scheffold, “High-quality photonic crystals with a nearly complete band gap obtained by direct inversion of woodpile templates with titanium dioxide,” *Sci. Rep.* **6**, 21818 (2016).
- [11] T. Gissibl, S. Thiele, A. Herkommer, and H. Giessen, “Two-photon direct laser writing of ultracompact multi-lens objectives,” *Nat. Photonics* **10**, 554 (2016).
- [12] M. Schmid, S. Thiele, A. Herkommer, and H. Giessen, “Three-dimensional direct laser written achromatic axicons and multi-component microlenses,” *Opt. Lett.* **43**, 5837 (2018).
- [13] Y. Li, H. Zhao, S.-F. Feng, J.-S. Ye, X.-K. Wang, W.-F. Sun, P. Han, and Y. Zhang, “New design model for high efficiency cylindrical diffractive microlenses,” *Sci. Rep.* **7**, 16334 (2017).
- [14] S. Rodríguez and A. Frölich, “3d micro-printing goes macro: Tailor-made materials enable pioneering developments and applications,” *Laser Technik Journal* **14**, 31 (2017).
- [15] T. Bückmann, M. Thiel, M. Kadic, R. Schittny, and M. Wegener, “An elasto-mechanical unfeelability cloak made of pentamode metamaterials,” *Nat. Commun.* **5**, 4130 (2014).

- [16] V. Tielen and Y. Bellouard, “Three-dimensional glass monolithic micro-flexure fabricated by femtosecond laser exposure and chemical etching,” *Micromachines* **5**, 697 (2014).
- [17] Y. Li, D. Fullager, E. Angelbello, D. Childers, G. Boreman, and T. Hofmann, “Broadband near-infrared antireflection coatings fabricated by three-dimensional direct laser writing,” *Opt. Lett.* **43**, 239 (2018).
- [18] Y. Li, S. Park, D. B. Fullager, D. Childers, M. K. Poutous, I. D. Aggarwal, G. Boreman, and T. Hofmann, “Near-infrared transmittance enhancement using fully conformal antireflective structured surfaces on microlenses fabricated by direct laser writing,” *Opt. Eng.* **58**, 010501 (2019).

CHAPTER 6: HIGH-CONTRAST INFRARED POLYMER PHOTONIC CRYSTALS FABRICATED BY DIRECT LASER WRITING¹

6.1 Abstract

One-dimensional photonic crystals were fabricated by three-dimensional direct laser writing using a single polymer to obtain reflectance values approaching that of a gold reference in the near-infrared spectral range. The photonic crystals are composed of alternating compact and low-density polymer layers which provide the necessary periodic variation of the refractive index. The low-density polymer layers are composed of subwavelength-sized pillars which simultaneously serve as a scaffold while also providing refractive index contrast to the adjacent compact polymer layers. Bruggemann effective medium theory and stratified-layer optical-model calculated reflectivity profiles were employed to optimize the photonic crystal's design to operate at a desired wavelength of $1.55\ \mu\text{m}$. After the fabrication, the photonic crystal's structure was compared to the nominal geometry using complementary scanning electron microscopy and optical microscopy micrographs identifying a true-to-form fabrication. The performance of the photonic crystals was investigated experimentally using FTIR reflection and transmission measurements. A good agreement between stratified-layer optical-model calculated and measured data is observed. We thereby demonstrate the ease of predictive design and fabrication of highly efficient one-dimensional photonic crystals for the infrared spectral range using three-dimensional direct laser writing of a single polymer.

¹Y. Li, T. Hofmann, *et al.*, *Opt. Lett.* **43**, 4711 (2018). Reprinted with permission © The Optical Society.

6.2 Introduction

Photonic crystals (PC) have many potential uses in optoelectronics and telecommunications due to their ability to manipulate electromagnetic fields according to Bragg's law inside of periodic dielectric structures [1, 2]. Depending on the arrangement of the unit cell, each PC possesses a specific photonic bandgap which behaves analogously to the electronic bandgap in semiconductors [3]. However, rather than being associated with an absorption onset energy, photonic bandgaps are typically characterized in terms of transmissive and reflective energy bands [1].

Over the last decade, several different fabrication techniques have been explored for the synthesis of PC. These techniques include for instance holographic lithography [4, 5], colloidal self-assembly [6], and three-dimensional direct laser writing [7]. In 2004 M. Deubel et al. utilized three-dimensional direct laser writing (3D-DLW) for the first time to fabricate a woodpile-like PC via two-photon polymerization of monomers [7]. More recently, 3D-DLW has become an established prototyping tool for the rapid fabrication of structures with sub-micron-sized features with various optical functionalities, such as anti-reflective structured surfaces [8, 9], micro-lenses [10], and waveguides [11], for instance. Numerous works have investigated PC's designed for high reflectance elements at telecommunications wavelengths either by optimizing the spatial dimensions of PCs fabricated from polymers or by incorporating high index materials onto polymer templates through so-called inversion processes [12, 13, 14, 15, 16].

For instance, by inverting polymer scaffold geometries using a-Si/Al₂O₃ and TiO₂, S. Peng et al. [17] and C. Marichy et al. [18] have both demonstrated almost 100% reflectance centered at 7.5 μm and 1.54 μm , respectively. The highest reflectance observed for PC without inversion was reported by C. Marichy et al. [18] for a PC based on the photo-polymer IP-Dip which exhibited a reflectance of 80%-85% at 1.35 μm .

It is well known that the incorporation of high index materials into polymer-based PC templates increases both the reflectivity and achievable bandwidth (see for instance Ref. [1, 13]). However, the requisite inversion process introduces an additional degree of complexity into the fabrication of the PC. Additionally, the inversion process may result in structural deformation of the scaffold. The thereby induced defects often diminish the desired optical performance of the PC. Apart from the introduction of structural defects, the integration of PCs fabricated using such inversion processes into existing optical devices may be problematic as the required processing is often incompatible with standard fabrication methods. Therefore, an application space exists for PCs produced solely by 3D-DLW via two-photon polymerization.

In this letter, we apply 3D-DLW for the fabrication of one-dimensional PCs using a single monomer to obtain more than 90% reflectance in the near IR spectral range. Such reflectance is achieved by employing a one-dimensional PC design which maximizes the refractive index contrast between adjacent layers in the PC. The PCs investigated here are composed of alternating compact and low-density plane-parallel layers fabricated of a single polymer [(as shown in Fig. 6.1(a)]. The low-density layers consist of columnar pillars square lattice pattern, which allow for tailoring of the effective refractive index described by Bruggemann effective medium approximations (Bruggemann EMA) by changing the volume pillar density [19]. Therefore, the low-density layers can be treated as a homogeneous medium with an effective permittivity of $\epsilon_{\text{low}}^{\text{eff}}$. The fabricated PCs can be described as a 1D permittivity variation of compact (ϵ_{com}) and low-density ($\epsilon_{\text{low}}^{\text{eff}}$) layers, as shown in the inset of Fig. 6.1(b). Stratified optical model calculations [20] were used to determine the geometry and composition (pillar volume density) of the PC such that the maximum reflectivity occurs at a wavelength of $1.55 \mu\text{m}$ which is relevant for telecommunication applications.

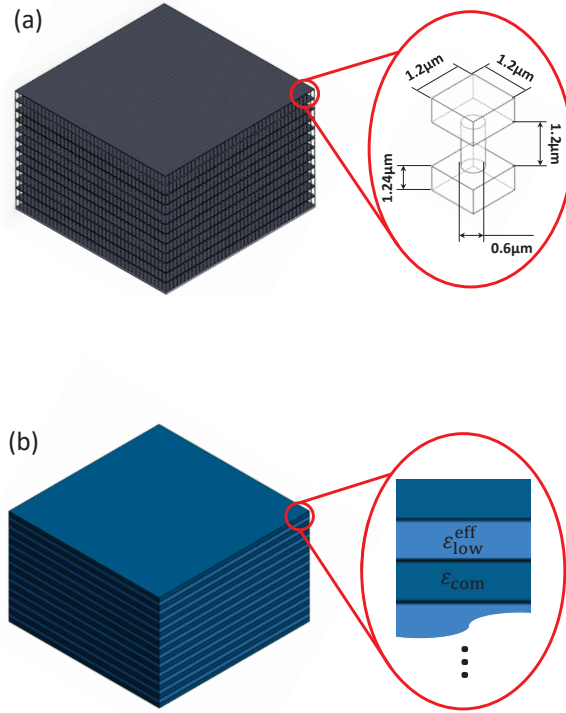


Figure 6.1: Nominal design for the 1D PCs investigated here. The PCs are composed of alternating compact and low-density polymer layers, as shown in panel (a). The low-density layers are constructed from pillar arrays. Structural dimensions and unit-cell geometry are shown in the inset. Panel (b) shows the corresponding effective medium model of the PCs which consists of alternating layers with different permittivity $\varepsilon_{\text{low}}^{\text{eff}}$ (light blue) and ε_{com} (dark blue), and results in a 1D permittivity variation along the z-axis which is used for the stratified-layer optical model calculations (inset).

6.3 Experiment and discussion

The optimized geometry for a one-dimensional polymer-based PC structure with photonic bandgaps centered at $1.55 \mu\text{m}$ and $2.06 \mu\text{m}$ is shown in Fig. 6.1(a). A commercially available 3D-DLW system (Photonic Professional GT, Nanoscribe, GmbH) was used to fabricate the PC by polymerizing IP-Dip monomer on a glass substrate. The fabricated PC has a square area of $48 \times 48 \mu\text{m}^2$ and consists of 12 repeating pairs of compact and low-density (nominal 24% volumetric fill fraction) layers, with a thickness of $1.24 \mu\text{m}$ and $1.2 \mu\text{m}$, respectively, as shown in the inset of Fig. 6.1(a). Except

for the first pair of layers adjacent to the substrate which appear to be tensile-strained a true-to-design fabrication can be recognized by comparing the SEM micrograph with the design shown in Fig. 6.1(a). The PC was fabricated in a single 3D-DLW fabrication step using a $63\times$ objective. The optimal exposure dose was determined prior to the sample synthesis. After fabrication, the unpolymerized monomer was removed by immersion in propylene glycol monomethyl ether acetate (PGMEA), and subsequently in 99.99% isopropyl alcohol (IPA) for 15 min and 10 min, respectively. Lastly, the remaining IPA was evaporated using dry nitrogen. Scanning electron microscopy (SEM) and light optical microscopy micrographs were acquired to evaluate the quality of the resulting PC structure as shown in Fig. 6.2.

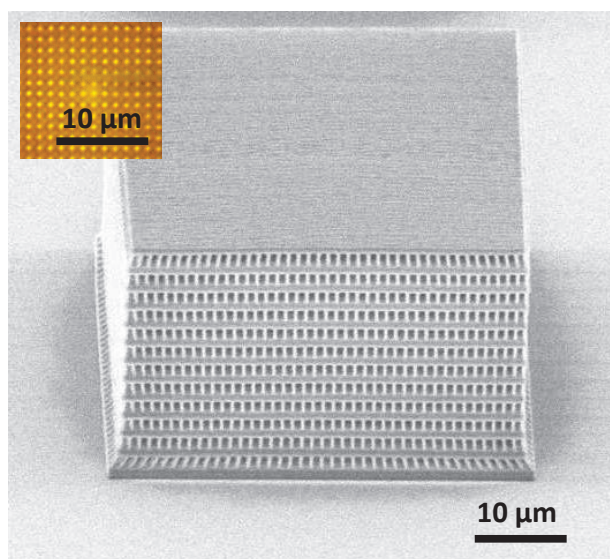


Figure 6.2: SEM micrograph of the polymer PC composed of 12 repeating pairs of compact and low-density layers. The inset depicts the micrograph of a section of the top view of the polymer PC obtained by an optical microscope in transmission revealing the lateral arrangement of the columnar pillars with a circular base in a square lattice pattern. Note that the SEM micrograph was obtained with the sample tilted by 50° relative to the substrate normal.

Reflection and transmission measurements were carried out over a spectral range from $1.3 \mu\text{m}$ to $2.3 \mu\text{m}$ using a FTIR spectrometer in conjunction with an infrared microscope (VERTEX 70 and HYPERION 3000, Bruker, Inc.). A confocal illumina-

tion using a $15\times$ Cassegrain objective was employed for the reflection measurements. Transmission measurements utilize a complementary $15\times$ Cassegrain condenser. The Cassegrain configuration results in an angular spread of the illumination ranging from 10.8° to 23.5° constrained by the numerical aperture of the Cassegrain objectives and the diameter of their central mirrors [21].

Fig. 6.3 (b) and (d) shows the unpolarized experimental (dashed green lines) and best-model calculated (solid red lines) reflectance and transmittance data, respectively. Experimental and best-model calculated data are found to be in very good agreement. For comparison the reflectance and transmittance data calculated for the nominal geometry (solid lines) are depicted in Fig. 6.3 (a) and (c), respectively. The reflectance and transmittance data were analyzed using stratified optical model calculations (WVASE32, J.A. Woollam Co.). The optical model employed here consists of a glass substrate and 12 A-B superlattice iterations of a compact and a low-density effective medium layer. During the data analysis the geometrical model parameters (layer thickness including thickness non-uniformity and polymer volume fraction) were varied using a Levenberg-Marquardt-based algorithm until the best match between experimental and calculated data was achieved (best-model). Note that an angular spread of 12° was used for all model calculations. The dielectric functions of the glass substrate and IP-Dip polymer used for the optical model calculations were previously determined using infrared variable angle spectroscopic ellipsometry and are not further varied during the analysis presented here [9, 22]. The dielectric function of the low-density layers $\varepsilon_{\text{low}}^{\text{eff}}$ is described using a Bruggemann EMA. This homogenization accounts for the symmetrically distributed, subwavelength sized, columnar IP-Dip pillars which constitute the low-density layers, and yields a complex dielectric function which depends on the volume fraction of columnar IP-Dip inclusions f_i and the permittivity of the constituents [23]:

$$\varepsilon_{\text{low}}^{\text{eff}}(f_i) = \frac{1}{4} \left\{ (3f_i - 1)\varepsilon_i + (2 - 3f_i)\varepsilon_h \pm \sqrt{[(3f_i - 1)\varepsilon_i + (2 - 3f_i)\varepsilon_h]^2 + 8\varepsilon_i\varepsilon_h} \right\}, \quad (6.1)$$

The complex dielectric functions of the inclusions (IP-Dip) and the host (air) are denoted by ε_i and ε_h , respectively.

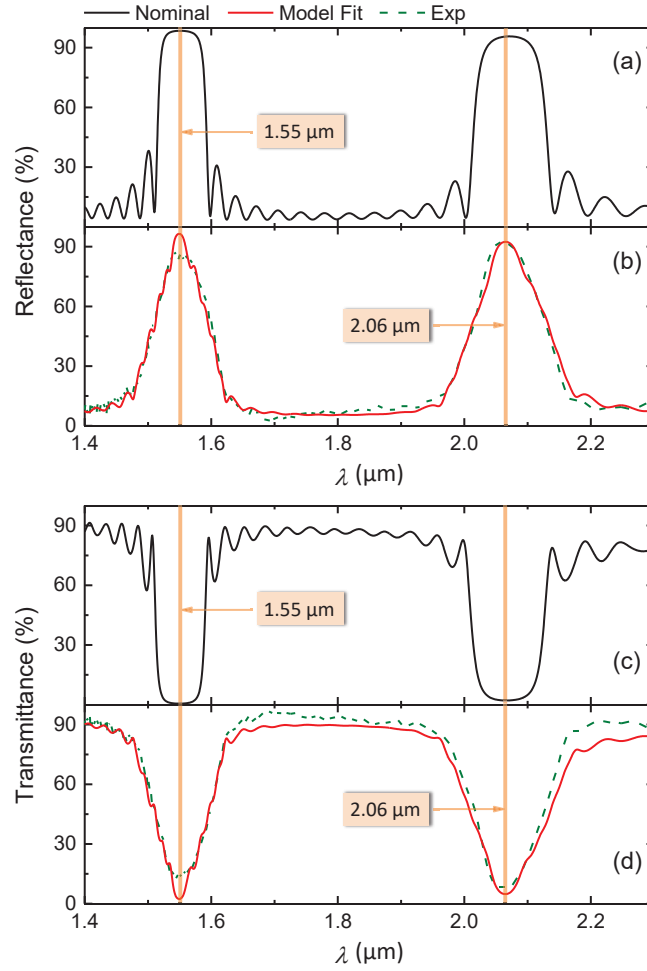


Figure 6.3: Experimental (dashed lines) and best-model (solid lines) calculated (b) reflectance and (d) transmittance spectra obtained for the polymer PC shown in Fig. 6.2. The calculated reflectance and transmittance spectra for the nominal geometry are shown for comparison in panels (a) and (c), respectively.

The best-model parameters obtained for the compact and the low-density effective

medium layer thickness are $d = 1242 \pm 5 \mu\text{m}$ and $d = 1202 \pm 5 \mu\text{m}$, respectively. The volumetric fill fraction was found to be $24.0 \pm 0.3\%$. All geometrical parameters are in very good agreement with the nominal structural parameters [see Fig. 6.1(a)]. The real and imaginary parts of the best-model complex dielectric function for the low-density $\epsilon_{\text{low}}^{\text{eff}}$ and the compact layer ϵ_{com} are shown in Figs. 6.4(a) and 6.4(b), respectively, for comparison.

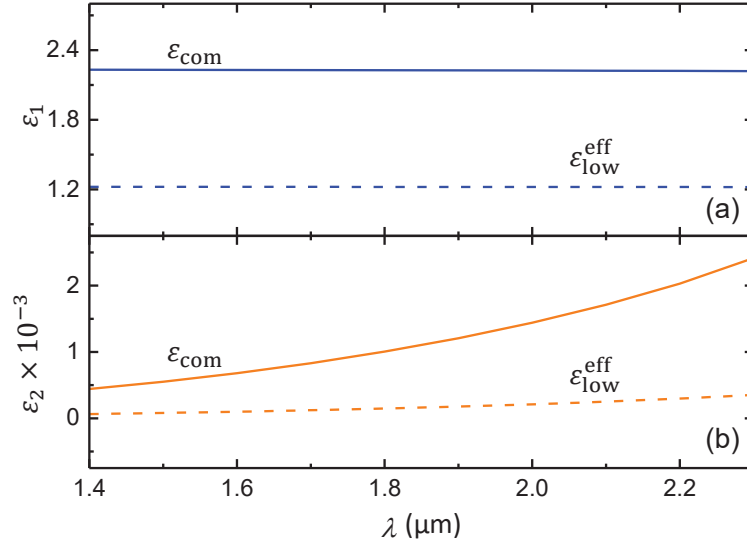


Figure 6.4: Real (blue lines) and imaginary (orange lines) part of the best-model calculated dielectric function of the low-density (dashed lines) and the compact layers (solid lines) are shown in panels (a) and (b), respectively, for comparison.

Comparing the reflectance and transmittance data calculated for the nominal geometry with the corresponding experimental and best-model data, one can notice that the bandwidth of the reflection bands is diminished. In addition, the sidelobes in the vicinity of the photonic bandgaps are significantly dampened. Based on our model calculations, this is due to the fact that the layer thicknesses are not perfectly uniform across the PC which is accounted for in the optical model by a layer non-uniformity of $0.57 \pm 0.04\%$. In contrast to a variation in the volumetric fill fraction f_i which causes an asymmetric broadening of the photonic bandgaps, a variation of the PC's layer thicknesses results in a symmetric shift of the photonic bandgaps. A non-uniformity

of the PC's layer thicknesses therefore causes the observed symmetric broadening of photonic bandgaps and results in a reduction of the reflectance maxima.

6.4 Conclusion

In conclusion, we have demonstrated that simple, one-dimensional polymer-based PC with a reflectivity above 90% can be obtained using 3D-DLW in a single fabrication step without employing inversion processes to increase the index of refraction contrast between adjacent layers. Compared to existing PC fabrication strategies, the approach presented here dramatically reduces the fabrication complexity and increases the fabrication efficiency for high-contrast, one-dimensional PC consisting of subwavelength-sized components.

For the investigated PC we observe a good agreement between experimental and best-model calculated reflectance and transmittance spectra in the infrared spectral range. This indicates a good quality of the as-printed structure which is confirmed both by SEM and optical microscopy. Furthermore, we find that simple Bruggemann effective medium calculations can be used to determine the effective refractive index of the low-density layers of the PC. In combination with stratified optical model calculations this allows for a simple optimization of the PC geometry. We have identified that a variation of the layer thickness is likely the primary cause for the reduction in reflectivity of the PC shown here. Thus further optimization of 3D-DLW fabrication parameters might allow for additional improvement of the layer homogeneity and thus increase in the reflectivity of one-dimensional PC. This observation opens a new avenue for 3D-DLW-fabricated, high-contrast, polymer-based PC, for instance operating as specular reflectors, which can be tailored over a very wide range from $1.25\ \mu\text{m}$ to $5\ \mu\text{m}$ where typical photo-polymers exhibit very low absorption.

REFERENCES

- [1] E. Yablonovitch, “Inhibited spontaneous emission in solid-state physics and electronics,” *Phys. Rev. Lett.* **58**, 2059 (1987).
- [2] S. John, “Strong localization of photons in certain disordered dielectric superlattices,” *Phys. Rev. Lett.* **58**, 2486 (1987).
- [3] K. Ho, C. T. Chan, and C. M. Soukoulis, “Existence of a photonic gap in periodic dielectric structures,” *Phys. Rev. Lett.* **65**, 3152 (1990).
- [4] D. Chanda, L. E. Abolghasemi, M. Haque, M. L. Ng, and P. R. Herman, “Multi-level diffractive optics for single laser exposure fabrication of telecom-band diamond-like 3-dimensional photonic crystals,” *Opt. Express* **16**, 15402 (2008).
- [5] M. Campbell, D. Sharp, M. Harrison, R. Denning, and A. Turberfield, “Fabrication of photonic crystals for the visible spectrum by holographic lithography,” *Nature* **404**, 53 (2000).
- [6] A. C. Edrington, A. M. Urbas, P. DeRege, C. X. Chen, T. M. Swager, N. Hadjichristidis, M. Xenidou, L. J. Fetters, J. D. Joannopoulos, Y. Fink, *et al.*, “Polymer-based photonic crystals,” *Adv. Mater.* **13**, 421 (2001).
- [7] M. Deubel, G. Von Freymann, M. Wegener, S. Pereira, K. Busch, and C. M. Soukoulis, “Direct laser writing of three-dimensional photonic-crystal templates for telecommunications,” *Nat. Mater.* **3**, 444 (2004).
- [8] M. Kowalczyk, J. Haberko, and P. Wasylczyk, “Microstructured gradient-index

- antireflective coating fabricated on a fiber tip with direct laser writing,” *Opt. Express* **22**, 12545 (2014).
- [9] Y. Li, D. Fullager, E. Angelbello, D. Childers, G. Boreman, and T. Hofmann, “Broadband near-infrared antireflection coatings fabricated by three-dimensional direct laser writing,” *Opt. Lett.* **43**, 239 (2018).
- [10] Y. Li, H. Zhao, S.-F. Feng, J.-S. Ye, X.-K. Wang, W.-F. Sun, P. Han, and Y. Zhang, “New design model for high efficiency cylindrical diffractive microlenses,” *Sci. Rep.* **7**, 16334 (2017).
- [11] I. Staude, G. Von Freymann, S. Essig, K. Busch, and M. Wegener, “Waveguides in three-dimensional photonic-bandgap materials by direct laser writing and silicon double inversion,” *Opt. Lett.* **36**, 67 (2011).
- [12] M. Deubel, M. Wegener, A. Kaso, and S. John, “Direct laser writing and characterization of “slanted pore” photonic crystals,” *Appl. Phys. Lett.* **85**, 1895 (2004).
- [13] S. Wong, M. Deubel, F. Pérez-Willard, S. John, G. A. Ozin, M. Wegener, and G. von Freymann, “Direct laser writing of three-dimensional photonic crystals with a complete photonic bandgap in chalcogenide glasses,” *Adv. Mater.* **18**, 265 (2006).
- [14] N. Tétreault, G. von Freymann, M. Deubel, M. Hermatschweiler, F. Pérez-Willard, S. John, M. Wegener, and G. A. Ozin, “New route to three-dimensional photonic bandgap materials: Silicon double inversion of polymer templates,” *Adv. Mater.* **18**, 457 (2006).
- [15] M. Hermatschweiler, A. Ledermann, G. A. Ozin, M. Wegener, and G. von Freymann, “Fabrication of silicon inverse woodpile photonic crystals,” *Adv. Funct. Mater.* **17**, 2273 (2007).

- [16] I. Staude, M. Thiel, S. Essig, C. Wolff, K. Busch, G. Von Freymann, and M. Wegener, "Fabrication and characterization of silicon woodpile photonic crystals with a complete bandgap at telecom wavelengths," *Opt. Lett.* **35**, 1094 (2010).
- [17] S. Peng, R. Zhang, V. H. Chen, E. T. Khabiboulline, P. Braun, and H. A. Atwater, "Three-dimensional single gyroid photonic crystals with a mid-infrared bandgap," *ACS Photonics* **3**, 1131 (2016).
- [18] C. Marichy, N. Muller, L. S. Froufe-Pérez, and F. Scheffold, "High-quality photonic crystals with a nearly complete band gap obtained by direct inversion of woodpile templates with titanium dioxide," *Sci. Rep.* **6**, 21818 (2016).
- [19] D. Bruggeman, "Dielectric constant and conductivity of mixtures of isotropic materials," *Ann. Phys. (Leipzig)* **24**, 636 (1935).
- [20] C. Sheppard, "Approximate calculation of the reflection coefficient from a stratified medium," *Pure and Applied Optics: Journal of the European Optical Society Part A* **4**, 665 (1995).
- [21] K. Hinrichs, A. Furchner, J. Rappich, and T. W. Oates, "Polarization-dependent and ellipsometric infrared microscopy for analysis of anisotropic thin films," *J. Phys. Chem. C* **117**, 13557 (2013).
- [22] D. B. Fullager, G. D. Boreman, and T. Hofmann, "Infrared dielectric response of nanoscribe ip-dip and ip-l monomers after polymerization from 250 cm^{-1} to 6000 cm^{-1} ," *Opt. Mater. Exp.* **7**, 888 (2017).
- [23] W. Cai and V. Shalaev, *Optical metamaterials: fundamentals and applications*, (Springer Science & Business Media 2009).

CHAPTER 7: CONCLUSION

Through this dissertation, we have demonstrated potential applications and meaningful contributions of the two-photon polymerization technique for the research and development of dielectric metamaterials. The dissertation can be summarized into three key aspects: (A) the accurate determination of the optical properties of photoresists compatible with two-photon polymerization; (B) the design of all-dielectric optical structures exhibiting increase or decrease of the reflectivity at infrared wavelengths; and (C) the rapid prototyping of optical components with critical dimensions ranging from a few hundred nanometers to several millimeters. In this chapter, we will briefly conclude the work presented in this dissertation and discuss the outlook for further development of novel optical material as additional nanofabrication lithography techniques are incorporated into the two-photon polymerization based fabrication strategy.

The accurate determination of the optical properties of the two-photon polymerized materials including IP-Dip, IP-L, and IP-S by using the spectroscopy ellipsometry is detailed in chapter 2. This first effort in establishing the optical properties of the polymers over spectral range from UV to NIR is critical for optical material designs where the investigated polymers are used as constituent materials. With the parameterized dielectric functions reported here for the first time, researchers and scientists can optimize optical structures based on these materials using finite-element-method based simulation, for instance.

Using the low-index polymer IP-Dip, two different optical structures engineered for exhibiting desired yet opposite optical responses (i.e., reflection suppression and elevation) were demonstrated in chapters 3 and 6. Chapter 3 shows the optimization

of conicoidal parameters of an ARSS to minimize reflection loss at telecommunication wavelengths. Chapter 6 discusses high-contrast polymer photonic crystals constructed using IP-Dip for boosting the reflection to a value compatible to a gold reference. These two optical structures emphasize the range of optical properties achievable by engineering their sub-wavelength sized unites.

The conformal ARSS coated microlenses, as detailed in chapter 4, demonstrate for the first time a new avenue for the fabrication of micro-optical components with functional optical coatings in a single fabrication step. This approach completely avoids any post-processing, compared to other fabrication strategies. The optical fiber interconnect shown in chapter 5 introduces a novel concept that utilizes two-photon polymerization technique to achieve a rapid prototyping of optical devices with critical features from a few hundred nm to several mm. This approach has substantial practical applications, as it allows the prototyping of opto-mechanical components and thereby may accelerate the development cycle of opto-mechanical devices by integrating mechanical and optical functionality.

In addition to all-dielectric metamaterials based on the two-photon polymerization technique, we propose to integrate other nanofabrication techniques into the research scope in order to further increase the range of optical responses achieved with these artificial materials. For instance, plasmonic metasurfaces can be practically achieved by metallizing the polymer structured surfaces fabricated using two-photon polymerization. Adding metals not only alters the optical performance of the original polymer structures significantly, but also causes interesting physical phenomena, e.g., plasmon-photon cavities and NIR plasmonic dipoles.